

**THERMOMECHANICAL STRAIN ANALYSIS OF
ELECTRONIC PACKAGES USING MOIRÉ INTERFEROMETRY
BY COMPUTATIONAL AND MANUAL FRINGE REDUCTION**

by

J. Morgan Slade

B.S. Materials Science and Engineering, MIT (1995)

**SUBMITTED TO THE DEPARTMENT OF
MATERIALS SCIENCE AND ENGINEERING
IN PARTIAL FULFILLMENT OF REQUIREMENTS
FOR THE DEGREE OF**

MASTER OF SCIENCE IN ELECTRONIC MATERIALS

at the

MASSACHUSETTS INSTITUTE OF TECHNOLOGY

June 1996

**© Massachusetts Institute of Technology 1996
All rights reserved**

Signature of Author _____

Department of Materials Science and Engineering
May 10, 1996

Certified by _____

Ravi Mahajan
Intel Corporation, Thermal/Mechanical Tools and Analysis Group
Technical Advisor

Certified by _____

David K. Roylance
Associate Professor, Materials Engineering
Thesis Advisor

Accepted by _____

Michael F. Rubner
TDK Professor of Materials Science and Engineering
Chair, Departmental Committee on Graduate Students

MASSACHUSETTS INSTITUTE
OF TECHNOLOGY

JUN 24 1996

Science

Thermomechanical Strain Analysis of Electronic Packages Using Moiré Interferometry by Computational and Manual Fringe Reduction

J. Morgan Slade

Submitted to the Department of Materials Science and Engineering on May 10, 1996
in partial fulfillment of the requirements for the degree of
Master of Science in Electronic Materials

ABSTRACT

The ability of moiré interferometry to measure the thermal strain in electronic packages was studied from a results oriented perspective. The physical foundations of moiré interferometry and strain analysis were reviewed in the context of their role within the Portable Engineering Moiré Interferometer (PEMI). Methods of computationally and manually computing strains from the interference fringe patterns are discussed and demonstrated. Manual techniques are shown to be simple with loss of accuracy, whereas the computational data reduction is complex with the potential of highly accurate continuous strain information.

An assessment of the resolution and accuracy of moiré interferometry was conducted through comparison measurements with thermal mechanical analysis (TMA) on specimens of 6061 aluminum. The results show resolution and accuracy to be similar in the two methods of analysis. Computational and manual analysis of the bulk aluminum thermal strain fringes yielded nearly identical results.

Evaluation of die bonded to organic and ceramic substrates was conducted with respect to bond layer shear strain and die warpage. Independently warpage data for the same samples was collected using a laser profilometer (flexus) and compared to the moiré warpage data. In comparing results the organic substrates versus the ceramic substrates were shown to cause a six-fold increase in shear strain in the bond layer at the corner of the die. An order of magnitude difference in warpage was also observed in the same packages using organic versus ceramic substrates.

The effect of encapsulation on plastic pin grid array (PPGA) packages was studied using moiré and FLEXUS data. Non-linear encapsulant material behavior was observed to cause the monolithic package warpage to reverse in the direction of accumulation. The warpage in the copper slug was significantly greater in the encapsulated PPGA. Shear strain in the die attach layer at the die corners was also ~3 times larger in the unencapsulated PPGA when compared by moiré with its encapsulated counterpart.

Computational fringe analysis using CAFRAN was conducted on 6061 aluminum and the PPGA die attach layer. The results were validated by the manual results obtained previously and demonstrate the feasibility of automated and continuous strain analysis using moiré interferometry and digital image processing techniques.

Technical Advisor: Ravi Mahajan

Title: Engineering Manager, Intel-Thermal/Mechanical Tools and Analysis Group

Thesis Advisor: David K. Roylance

Title: Associate Professor of Materials Engineering, MIT

Table of Contents

	<u>Page</u>
Abstract	2
Acknowledgments	11
Chapter 1-Introduction	13
Chapter 2-Background and Theory of Moiré Interferometry	16
2.1-History of Moiré Interferometry	16
2.2-Theory of Moiré Interferometry	17
2.2.1-Constructive and Destructive Interference	17
2.2.2-Diffraction	18
2.2.3-Interferometry in the PEMI	20
2.3-Manual Strain Analysis	25
2.4-Computational Moiré Strain Analysis	27
2.4.1-Computational Fringe Analysis History	27
2.4.2-Theoretical Foundation of CAFRAN	29
Chapter 3-General Experimental	34
3.1-Introduction	34
3.2-Equipment/Lab Setup	34
3.2.1-Portable Engineering Moiré Interferometer (PEMI)	34
3.2.2-Thermal Chamber and Temperature Controller	36
3.2.3-Image Recording System	37
3.2.4-Oven and Fume Hood	39
3.3-Sample Preparation	39
3.3.1-Electronic Package Cross-sectioning	39
3.3.2-Grating Attach Epoxies	43
3.3.3-Diffraction Grating Application	45
3.3.4-Failure Modes in Grating Replication	48
3.4-PEMI Calibration and Specimen Analysis	49
3.4.1-Null Field Alignment	49
3.4.2-Sample Alignment and Analysis	52
Chapter 4-Validation of PEMI and Moiré Technique	53
4.1-Introduction	53
4.2-Results	53
Chapter 5-Die Bonded to Substrate: Ceramic versus Organic	54
5.1-Introduction	55
5.2-Die-Bonded Substrate Sample Preparation	56
5.2.1-Thermal Carrier Adjustment	57
5.2.2-Manual Analysis Elements	57
5.2.3-Moiré Warpage Measurement	58
5.3-Shear Strain Analysis Results	59
5.4-Die Warpage Results	60
5.5-Conclusions	63
Die Bonded to Ceramic V-field Fringe Patterns	65
Die Bonded to Organic V-field Fringe Patterns	66

Table of Contents (Continued)

	<u>Page</u>
5.5-Conclusions(continued)	
Die Bonded to Ceramic-Bond Layer Shear	70
Die Bonded to Organic-Bond Layer Shear	73
Chapter 6-Encapsulated Versus Non-encapsulated PPGA	78
6.1-Introduction	78
6.2-PPGA Sample Preparation	79
6.2.1-Thermal Carrier Adjustment	81
6.2.2-Manual Analysis Elements	81
6.2.3-Moiré Warpage Measurement	82
6.3-Shear Strain Analysis Results	83
6.4-Slug and die Warpage Results	84
6.5-Flexus Warpage Analysis	90
6.6-Summary	92
Unencapsulated PPGA V-field Fringe Patterns	94
Encapsulated PPGA V-field Fringe Patterns	97
Die Attach Shear in Unencapsulated PPGA	101
Die Attach Shear in Encapsulated PPGA	103
Chapter 7-Computational Moiré Fringe Analysis of Aluminum and PPGA Die Attach Layer	105
7.1-Introduction	105
7.2-Computational Fringe Analysis	105
7.2.1-Image Quality Control	106
7.2.2-CAFRAN Image Analysis	107
7.3-CAFRAN Analysis of Aluminum	109
7.4-Computational Analysis of PPGA Fringe Patterns	113
Chapter 8-Conclusions and Future Work	119
8.1-Introduction	119
8.2-Summary of Results	119
8.3-Future Work	121
References	123

Table of Figures

Figure 2.1-Constructive and destructive interference pattern caused by the cancellation of opposing electric and magnetic field components when they share common plane and are out of phase with one another.	18
Figure 2.2-(left) SEM image of a 1200 line/mm diffraction grating similar to the ones used for the PEMI and (right) a diagram illustrating the line pitch definition.	19

Table of Figures (Continued)

	<u>Page</u>
Figure 2.3-(left) Bragg diffraction and (right) the diffraction pattern resulting from the destructive interference phenomena in monochromatic light plotting intensity versus angle of diffraction.	19
Figure 2.4-Optical system contained within the PEMI including beam splitter, adjustable angle redirection mirrors and the specimen.	20
Figure 2.5-Two beam interrogation of reference grating resulting collinear diffraction orders which produce no fringe pattern. (null field)	22
Figure 2.6-U-field fringe pattern exhibiting both normal and shear strains. A sample element has been drawn for manual analysis.	26
Figure 2.7-(a) Fringe pattern of normal strain in bulk aluminum (b)the intensity profile for a fringe pattern such as the one found in (a).	30
Figure 2.8-(a) 2D FFT representation of sample at lower strain (b) 2D FFT representation of same sample after a finite amount of thermal strain accumulation. Note that these samples exhibit only uniaxial strain as the harmonics exhibit only x-directional periodicity.	32
Figure 3.1-Portable Engineering Moiré Interferometer and Polaroid Camera.	35
Figure 3.2-Skeletal representation of the optical elements comprising the PEMI.	36
Figure 3.3-Schematic representation of the moiré and data acquisition setup.	36
Figure 3.4-Front (left) and side (right) view of the moiré thermal chamber.	37
Figure 3.5-Planes of the cross-sectional cuts used in the die bonded substrate and PPGA studies.	40
Figure 3.6-(top) Diagram of wire saw pulley mechanism. (bottom) Various orientations in which the packages were fixtured. Note that the wire arcing is highly exaggerated to for illustration purposes.	42
Figure 3.7-Scanning electron microscope image of 1200 line/mm grating (left), the definition of the grating pitch (g) which is $1/f$ (middle), and a cross-section of the ULE type gratings (right).	43
Figure 3.8-Grating application support bed from the top (left) and from the end (right).	46
Figure 3.9-Conventional grating replication technique used exclusively for LGA samples in this study.	47
Figure 3.10-Null field condition for the reference grating specimen.	51

Table of Figures (Continued)

	<u>Page</u>
Figure 3.11 (left) v-filed of PPGA at room temperature. (right) u-field of PPGA at room temperature.	52
Figure 4.1-CTE data for 6061 bulk aluminum for various directions and techniques of measurement.	54
Figure 5.1-Die bonded to substrate samples exhibiting a concave down warpage at temperatures below 180 °C.	56
Figure 5.2-Die bonded to substrate structural diagram. (left) diagonal cross section, (right) top view with die facing up.	57
Figure-5.3-Example of element definition used to do manual strain analysis in die-bonded to organic and ceramic samples.	58
Figure 5.4-Shear strain profile of region defined in Figure 5.2 for all four samples analyzed in the study. The room temperature strain magnitude for the opposite corner is also represented.	60
Figure 5.5-Die warpage temperature curves for die bonded to ceramic packages.	61
Figure 5.5-Die warpage temperature curves for die bonded to organic packages.	62
Figure 6.1-Direction of warpage upon cooling of a die-copper substrate mounted on an organic circuit board with die cavity without encapsulant. The copper has a larger CTE than both the organic board and the silicon.	79
Figure 6.2-PPGA encapsulated package used in moiré and FLEXUS testing.	80
Figure 6.3-PPGA cross-section illustrating the longitudinal cracking that was the dominant failure mode of the cross-sectioned PPGA packages.	80
Figure 6.4-Example of the 88 x 490 µm element used for manual calculation is the PPGA.	82
Figure 6.5- Strain profile data for encapsulated and unencapsulated PPGAs illustrating the effectiveness of the encapsulant in reducing the shear strain the critical die attach bond layer.	84
Figure 6.6-Warpage profile of encapsulated PPGA exhibiting a reversal in relative warpage direction(slug oriented up).	85
Figure 6.7-Warpage profile for unencapsulated PPGA exhibiting a monotonically increasing warpage with temperature decrease.	86
Figure 6.8-Warpage Profile in die of encapsulated PPGA exhibit relative warpage reversal between 23 and 40 °C.	87

Table of Figures (continued)

	<u>Page</u>
Figure 6.9-Unencapsulated PPGA die warpage profile exhibiting constant strain accumulation similar to the copper slug in the same package.	88
Figure 6.10-Profile of the vertical displacement of the copper and die relative to the absolute preexisting warpage magnitude at 104 °C. The encapsulated PPGA first decreases in absolute warpage magnitude before increasing again. The unencapsulated PPGA increases consistently with decreasing temperature.	89
Figure 6.11-Absolute warpage measurements of encapsulated PPGA slugs as a function of temperature. The vertical line passes through the value used as the basis for relative measurement below 104°C.	90
Figure 6.12-Relative change in PPGA slug warpage magnitude with respect to the absolute warpage state at 104 °C as measured by moiré and flexus.	91
Figure 7.1-A (left) and B (right): Moiré fringe pattern of bulk aluminum on which the grating was replicated at 104 °C. The fringes represent displacement due to thermal strain accumulated in cooling to the sample temperature of A (23.9 °C) and B (52.8 °C). CAFRAN is used to compute the difference in strain (CTE) between the two fringe patterns.	109
Figure 7.2-A and B-Two-dimensional frequency domain representation of Figures 7.1-A and B within CAFRAN.	109
Figure 7.3-A and B-Isolated first harmonics for Figures 7.4-C and D respectively from left to right.	110
Figures 7.4-A and B-Fourier transform filtered complex fringe pattern exhibiting smoothed intensity profiles.	111
Figure 7.5-A and B-The cumulative phase maps representing the original fringe patterns. The phase accumulates from left to right.	111
Figure 7.6-Phase difference map representing the pixel by pixel cumulative phase difference between the two aluminum fringe patterns.	112
Figure 7.7-Color contour strain map for bulk aluminum specimen analyzed in Chapter 4. The legend denotes the CTE value based on the known ΔT and strain values by applying equation (7-2) to allow comparison with data in Chapter 4.	112
Figures 7.8 A and B-Room temperature (23 °C) U-Field (left) and V-Field (right) fringe patterns for encapsulated PPGA analyzed in Chapter 6.	114
Figure 7.9A-U-field AOI in PPGA die attach region at 23.7 °C before importing into CAFRAN.	114

Table of Figures (Continued)

	<u>Page</u>
Figure 7.9B-U-field AOI in PPGA die attach region at 33.7 °C before importing into CAFRAN.	114
Figure 7.10A-Two dimensional frequency domain representation of Figure 7.9A.	114
Figure 7.10B-Two dimensional frequency domain representation of Figure 7.9B.	115
Figure 7.11A-Isolated first harmonic from Figure 7.10A representing 7.9A.	115
Figure 7.11B-Isolated first harmonic from Figure 7.10B representing 7.9B.	115
Figure 7.12A-IFFT of Figure 7.11A to recreate the 23.7 °C fringe pattern.	115
Figure 7.12B-IFFT of Figure 7.11B to recreate the 33.7 °C fringe pattern.	115
Figure 7.13A-Phase map of fringe pattern in Figure 7.12A.	116
Figure 7.13B-Phase map of fringe pattern in Figure 7.12B.	116
Figure 7.14-Phase difference map depicting the pixel by pixel difference in the phase value in Figures 7.13 A and B.	116
Figure 7.15-Strain map of encapsulated PPGA die attach region.	116
Figure 7.16 A and B-Comparison of strain maps for ΔT 's of 10°C and 19.5°C.	117

Table of Tables

	<u>Page</u>
Table 3.1-Glass Transition Temperature test for grating attach epoxies.	45
Table 3.2-Reference grating specifications.	46
Table 4.1-All figures reported in ppm/°C.	53
Table 5.1-The accumulated strain magnitudes in die corner epoxy bond regions defined in figure 5.2.	59
Table 5.2-Vertical displacement values obtained by moiré and FLEXUS.	62
Table 6.1-Relative vertical displacement values obtained by averaging the two values for both corners of the slug or die for each temperature.	89

Acknowledgments

The completion of this study and of the degree program at MIT was made possible by the loyal support of a large number of the faculty members of the Materials Science and Engineering Department as well as the gracious commitment of Intel Corporation to efforts in higher education. The author is grateful to these two organizations for the opportunity to be exposed to their high ambient level of competence, and for the specific learning and occasions for personal growth which were afforded him. The early years of technical development at MIT were in a large part fostered by the efforts of Professor Michael Cima through his constant support of the author's growth as a researcher in the UROP. Without the technical and financial support of Professor Cima and his group the road would have appeared much more difficult. Other professors providing constant inspiration during the more nascent period of the experience were Associate Professor Kirk Kolenbrander, Assistant Professor Anne Mayes and Professor Régis Pelloux. It is the spirit and energy from special individuals such as these which becomes the true motivation for self-improvement and learning. To be sure, enough notice and thanks cannot be given to Department Administrator Joe Dhosi and Department Head, Professor Thomas Eagar for their contrarian sense of fairness and custodianship. Challenge, strife and success share a causal existence at MIT and at times attempt to subsume the participants of the learning process. Singular acts of compassion, mentorship and companionship stand as islands of cognizance against the imbalanced burdens of the MIT experience. Thanks to the inspiring members of the department who are able to keep the humanity in engineering.

The research itself was completed under the supervision and with the sage guidance of Dr. Ravi Mahajan of the Thermal/Mechanical Tools and Analysis Group of Intel Corporation. Greg Turturro, George Raiser and many others at Intel also deserve thanks for their consistent and continued support of the project. Professor Mani Prakash of The Department of Mechanical Engineering of The State University of New York in Binghamton was instrumental in discovering and obtaining a copy of CAFRAN. Discussions with Professor Prakash and his graduate students were instrumental in the decision to pursue the software package as a means of processing the images and they also assisted the author in obtaining a copy of the software.

The bundle of image processing algorithms implemented in the automated fringe reduction were written by Professor Yoshiharu Morimoto and his graduate students. Professor Morimoto (a.k.a. Harry Moiré) is a faculty member at the Department of Mechanical Engineering of Osaka University as well as the Systems Engineering Department of Wakayama University in Japan. Professor Morimoto distributed his software program, 3D-CAFRAN, for no charge at the 1995 SEM Spring Conference in Grand Rapids, Michigan. The reference section contains a number of papers detailing the image processing methods employed in CAFRAN. Without the previous software and experimental research of Professor Morimoto and Professor Motoharu Fujigaki of Wakayama University the automated fringe reduction portion of this paper would not have existed. At the MIT end Associate Professor David Roylance has been kind enough to provide feedback and insure that the focus of the thesis remained in-tune with the academic expectations.

An entire thesis would not provide enough opportunity to recognize the fine job my parents, Lawrence James Slade and Jessie Adelia Slade have done in raising me with the keen perception of opportunity, avarice for knowledge, and impeccable sense of ethics which they embody. The sacrifices which they have endured in allowing me to attend MIT could be done no justice in such short space. My elder sister, Jamie Lynn Slade (Brown '93) and younger brother, Lincoln Jeffrey Slade (RVHS '98) both were the object of my thoughts as I have had little opportunity to spend time with them over the last six years. I look forward to sharing many exciting experiences with them. It would be difficult to find a family as loving, supportive and understanding as you have been.

J. Morgan Slade

Chapter 1

Introduction

Within the microelectronics industry the objective of miniaturization has become pervasive in the design rules for next generation packaging due to the economic and performance premiums associated with smaller first and second level structures. Surface mount technology (SMT) has ascended in its hierarchical role within the design process from being considered an afterthought to being an integral driver of design in order to capture the performance and component cost gains associated with high density integration schemes. SMT has in the last twenty years advanced at a phenomenal pace with the conventional perimeter lead devices being replaced by higher I/O density ball grid array (BGA), pin grid array (PGA) and multichip modules (MCM). In an effort to free more of the costly board real estate engineers implement these much denser I/O lead structures which utilize the board space beneath the chip. For critical applications the high lead density area array chip carriers continue to supplant the perimeter lead devices.

Miniaturization of the primary and secondary structures brings with it higher tolerances and more complex material systems with their associated non-linear thermomechanical interactions. These multilayer systems involve the implementation of low cost and process flow tailored materials that introduce a myriad of uncharacterized material behaviors into the integration structure. The three design drivers for an electronic package have become electrical performance, manufacturability and thermomechanical performance. Though the thermomechanical issues are now recognized more openly as deserving of forethought, in the microelectronics industry cash is king and the lowest cost material systems are frequently chosen irrespective of their disadvantages by thermomechanical measures.

Perhaps the most effective counter to design driven almost exclusively by material cost would be the demonstrated ability to characterize and thermomechanically model primary and second level packages in the context of all potential packaging materials. Through more efficient implementation of hybrid finite element analysis techniques using material values provided by progressive material characterization tools, the failure rate and ultimately the failure costs of various material systems can be assessed. By providing a quantitative long term cost arguments,

driven by thermomechanical considerations, the materials selection and design decisions will not reflect merely the manufacturing cost of the package or electrical performance factors, but the long term economic cost of the package.

The primary limitations in implementing a fully integrated package design process lie in the inability to efficiently provide technically significant assessments of the various designs iterations. There exists a duality between mechanical modeling and experimental measurement which must be embraced in order to accurately model these complex physical systems. Not only must the finite element models be robust in their ability to consider progressively more complex and finer geometries, but they must be able to incorporate the complex material behaviors of creep, viscoelastic strain and other non-linear parameters. Furthermore, fatigue lifetime models must incorporate the same parameters in order to discern the differences in failure lives of various material systems. These capabilities will allow design engineers to quantify the effect of material and design decisions in terms of long term package reliability economics.

The second part of analytical mechanical design capability is the ability to characterize complex material behavior accurately and with the resolution necessary for accurate modeling. A battery of new techniques are being employed to measure strength, thermal expansion and microstructural effects on material behavior, but one endemic limitation is the inability to observe the materials *in situ*. Standardized materials characterization tools can reveal most of the critical material parameters for mechanical models, but in order to validate both the integrity of the model and the characterization techniques' inputs in unison, *in situ* measurement of the stress-strain response of the system must be conducted.

Various techniques based on strain gauge rosettes, stress sensitive transistor arrays and laser profilometry have been used to characterize strain. These techniques fail to provide the continuous whole-field strain information required for finite element model validation. Only by implementation of moiré interferometry can the continuous strain information across an entire package cross-section be obtained. It would require tens of thousands of strain gauges to collect the same strain information contained within a single moiré interference fringe pattern. Through implementation of an environment chamber, the temperature dependence of strain within a package can be measured and used in model prediction validation. Due to recent simplifications, the

technique also lends itself to the efficient turnaround of analytical assessments of the numerous design considerations.

By interpreting the fringe patterns using digital image processing techniques, maps identical to FEM maps can be created to further ease the results validation and provide the strain information critical to FE modelers. Though the computational analysis of moiré data is not perfected, it has demonstrated promise in becoming a lynch-pin of mechanically driven electronic package design. The technique will allow high resolution measurement of the strain response in resins and alloys in service within an integration scheme. The sensitivity of the measurement will also allow the observation of the mechanical effect of microstructure and more specifically of thin layer materials which demonstrate drastically different behavior from the bulk. Through the precise control of sample temperature the transient material characteristics relevant in defining manufacturing protocol can be addressed as well. This study will demonstrate the importance of the moiré interferometry in advancing the sophistication, and ultimately the effectiveness in driving design decisions, of mechanical modeling in the microelectronics industry.

Chapter 2

Background and Theory of Moiré Interferometry

2.1 History of Moiré Interferometry

Centuries prior to the inception of the first moiré interferometer the concept of moiré was probably first observed in the trade of fine silks which create a “watered” or “shimmering” pattern when overlaid. In fact the word “moire” is the French translation for the English word “mohair” which is “a fabric or yarn made wholly or in part from the long silky hair of the Angora goat”¹. Presently the word has also become associated with the independent pattern seen when two geometrically regular patterns are superimposed. The foundation of moiré as a strain measuring technique are descendent from geometric moiré which in turn was first explored by A. Righi and Lord Rayleigh in the later part of the 19th century².

The physical principles describing moiré interferometry were not conceived of until 1954 when J. Guild wrote *The Interference System of Crossed Diffraction Gratings*³. For lack of a monochromatic light source almost exclusively efforts focused on geometric moiré which relies on no electromagnetic interference of light. The primary limitations with geometric moiré were that as the features of the gratings approach the wavelength of the light, the fringe contrast decreased rapidly. In 1954 Post demonstrated that the fringe density on photoelastic materials could be increased by a factor of 15, yielding much higher resolution². He then attempted the same tactic with geometric moiré by deliberately mismatching the reference and specimen gratings to obtain fringe multiplication. It was discovered by Post and others that the phenomena of higher fringe multiplication and high contrast were competing mechanisms. This fact discouraged further development of geometric moiré for small strain measurement².

It was well known that overlapping beams of coherent light gave rise to a virtual grating structure, but using a discharge lamp, the only available monochromatic light source, they obtained only a limited useful area of fringes. In the early 1970s, lasers became available to two Europeans, Boone and Cook, who were able produce high-density photoresist gratings². By using a conjugate beam method, Kato was able to produce directly applied gratings which had line densities on the order of 2240 lines/mm². They found, however, that the photoresist would easily exceed its elastic

limit in most situations. Throughout the 1970s several groups of researchers in Japan, England and the United States attempted to produce high density, high quality gratings. Currently, the process of grating replication involves photolithography on ultra-low expansion glass upon which aluminum is subsequently vacuum deposited. The deformation limits of the gratings are set by the aluminum film and the epoxy material used for grating application to the sample.

Real progress in moiré interferometers began taking shape in 1971 with the work of Boone and separately by Cook when they noted that one could use the same optical system to both create and interrogate specimen gratings². The invention of the moiré interferometer was first accomplished by Matsumoto and Takashima and separately by Kato in 1973. Variations on these original interferometers were then constructed by Post at Virginia Polytechnical Institute as well as researchers at Strathclyde University. In 1993 Daniel Post *et al.* published the classic *High Sensitivity Moiré* summarizing the accomplishments in the field since the 1950s. This work prompted the development of the Portable Engineering Moiré Interferometer by International Business Machine Corporation in Endicott, New York in 1994. At the same time IBM developed the photoresist-thin aluminum film on ULE glass gratings used by many moiré interferometry researchers today.

2.2 Theory of Moiré Interferometry

Two fundamental electromagnetic wave interactions are required in order to obtain interference patterns: destructive interference and diffraction. Both are a result of interaction of electromagnetic (EM) waves with other EM waves or with a physical structure with the same length scale as the wavelength. This section will provide a mechanistic explanation of process of producing moiré fringe patterns. The operation of these phenomena in the Portable Engineering Moiré interferometry (PEMI) is described in that manner.

2.2.1 Constructive and Destructive Interference

Moiré interferometry requires at least one interference event to produce an interference fringe pattern. In the PEMI two interference events occur in sequence, however it is useful to have an *a priori* understanding that only one interference event is prerequisite. Considering a simple case of EM interference where two noncolinear coherent beams of light intersect and the two beams contain EM wave trains which share identical planes of electrical polarization, the two will

interfere with one another at some finite interval related to the angle (2α) between their respective directions of propagation in space. Equation (2-1) describes the frequency with which the intensity of light varies in a plane passing through the region of intersection of the two beams and with which share mutually congruent angles of incidence.

$$f_{\text{int}} = \frac{2}{\lambda} \sin(\alpha) \quad (2-1)$$

Above, f_{int} is the frequency of the interference pattern in the region of intersection as a function of α and the wavelength, λ . Figure 2.1 below depicts this interference process for two intersecting beams polarized in the same plane and having the same wavelength.

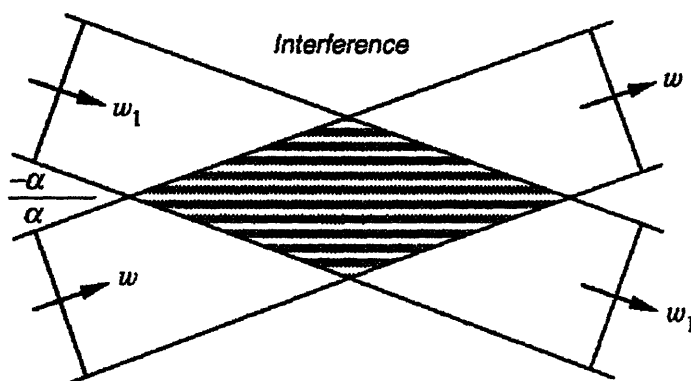


Figure 2.1-Constructive and destructive interference pattern caused by the cancellation of opposing electric and magnetic field components when they share common plane and are out of phase with one another.

The same physical conditions which cause the pattern shown above in Figure 2.1 are the source of the moiré fringe pattern and the virtual grating, both of which are describe later in the context of the PEMI.

2.2.2 Diffraction

When periodic physical features of reflective surfaces have dimensions approaching the wavelength of light impinging upon them, diffraction is said to occur. In moiré interferometry this periodic structure is called the diffraction grating. A scanning electron microscope image of a moiré diffraction grating is shown below in Figure 2.2. Considering a single wavelength of laser light, it is observed that for light impinging upon a periodically varying surface that the emerging (diffracted) light will do so at preferred directions related to the wavelength of light, the periodicity of the structure and the incident angle of the light. This phenomena, called Bragg diffraction, is

described by equation (2-2) below. The light diffracts off the grating in predictable directions and in varying intensities. These directions are governed by the diffraction equation,

$$\sin(\beta_m) = \sin(\alpha) + mf_{spec}\lambda \tag{2-2}$$

where β_m is the angle of the m th diffraction order, α is the angle of incidence, m is the diffraction order number, λ is the wavelength of light and f_{spec} is the frequency of the periodic structure being illuminated.

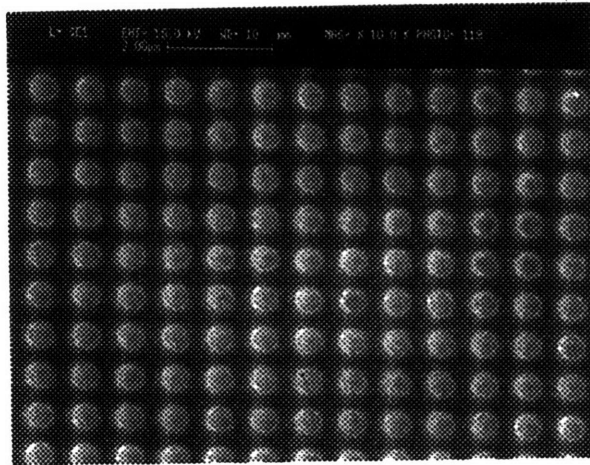


Figure 2.2-SEM image of a 1200 line/mm diffraction grating used for the study.

Remarkably due to the same constructive and destructive interference phenomena mentioned earlier, when the incident same wavelength light is polarized in the same direction (whether that direction be coplanar or noncoplanar) the light emerges only at discrete and predictable angles with respect to the sample. The intensity of diffraction as a function of observation angle from the specimen is given below in Figure 2.3.

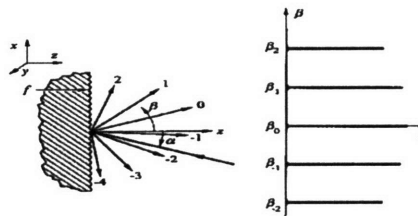


Figure 2.3-(left) Bragg diffraction and (right) the diffraction pattern resulting from the destructive interference phenomena in monochromatic light plotting intensity versus angle of diffraction.

By consulting equation (2-2) it is clear that for a constant incident angle (α), diffraction order (m) and wavelength of monochromatic light that the angle at which the diffraction orders emerge from the sample will change as a function of the frequency of the diffraction grating. In moiré the grating is a thin ridged aluminum film (mounted to a sample) which conforms to the underlying sample distortions. Thus as the sample distorts, the frequency of the grating changes and the angle at which the diffraction orders emerge from the sample becomes a function of that distortion. This is the diffraction phenomena at the heart of moiré interferometry. Having introduced both of the physical phenomena required for moiré interferometry, the next section will describe how these phenomena interact to create interference patterns representing displacements.

2.2.3 Interferometry in the PEMI

The PEMI used in this study is a compact assembly of all the optical elements required to produce the unique sequence of optical events necessary for moiré interferometry. This section will summarize the purpose and sequence of each segment of the optical system as it relates to the production of fringe patterns. A representation of the physical setup of the the PEMI is shown below in Figure 2.4.

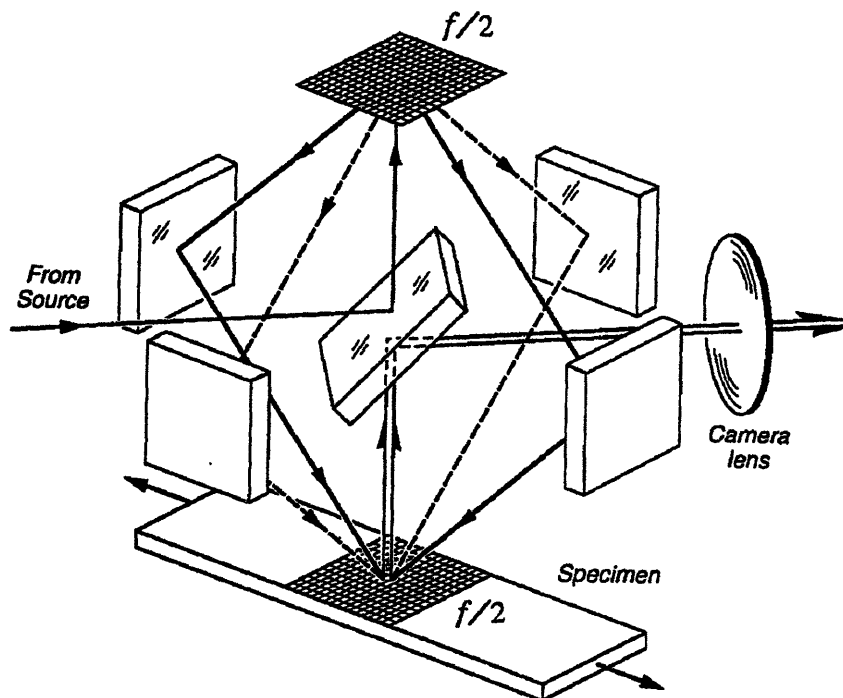


Figure 2.4-Optical system contained within the PEMI including beam splitter, adjustable angle redirection mirrors and the specimen.

The light source for the PEMI is a He-Ne laser which is originally a federal safety regulation Class II source as it emerges from the fiber optic from the laser, but becomes Class IIIB after redirection from the center double-sided mirror (Center Figure 2.4) to the beam splitter. Upon emission of the light from the laser it passes immediately through a collimating lens which insures uni-directional polarization of the light. Implicitly when laser light emerges from the laser cavity it is monochromatic and in phase. The light is then redirected to the permanent diffraction grating mounted inside the PEMI (top of Figure 2.4). The frequency of the grating is identical to that of the reference gratings described in Chapter 3 and shown in Figure 2.2.

By design the primary diffraction orders from the crossed grating grid are in the directions of the four adjustable mirrors which are then used to direct the light towards the specimen. In order to obtain a meaningful fringe pattern, from the four beams, the angles at which they impinge upon the sample must be congruent. This insures that by equation (2-2) that the diffraction angle at which each beam emerges from the sample is purely a function of the grating frequency on the sample. In order to establish the angular congruency it is necessary to control both the angular relationship between the beams being redirected by the mirrors in addition to the tilt and rotation of the specimen plane. Only when both of these parameters are properly calibrated will the PEMI yield meaningful fringe patterns. This process of calibration is known as null field alignment.

Since moiré interferometry allows the measurement of deformations, implicitly there exists a state of zero deformation with deformation taking a negative or positive value with respect to that reference state. At the point in time when the grating is applied to the sample the frequency of the grating on the sample is the same as that of the reference grating (and the permanent grating). The sample is then loaded mechanically or thermomechanically to change the grating frequency by minute amounts related to the magnitude of deformation that has occurred. The dimensions at the point in time at which the reference grating was mechanically bonded to the sample is defined as the state of zero deformation.

Ideally a fringe pattern will represent only the deformation in the sample that has accrued since the point in time when the grating was applied. Thus, if it is possible to align the mirrors such that the impinging beams diffract at an angle normal to the surface of the reference grating, then they will not interfere with one another in the camera plane because they will be collinear and

in phase. This condition is shown below in Figure 2.5. If a sample with a grating frequency differing from that of the reference is interrogated without changing the mirror adjustments, the diffraction orders corresponding to the incident beams will emerge at non-normal angles and by the principle described in Section 2.2.1, they will interfere with one another in the plane of the CCD camera.

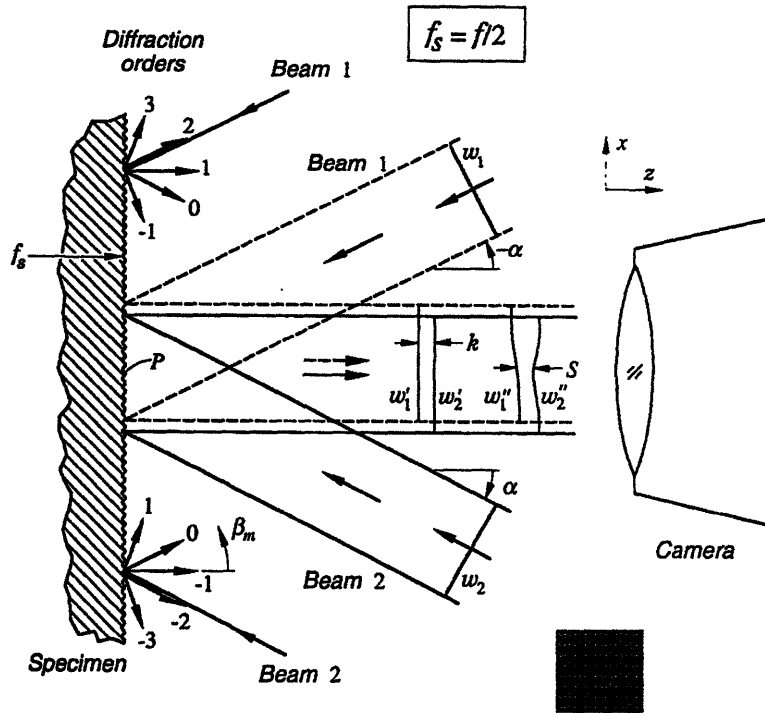


Figure 2.5-Two beam interrogation of reference grating resulting collinear diffraction orders which produce no fringe pattern. (null field)

Using equation (2-2) it is possible to determine that each fringe represents a constant 417 nm of deformation. It is also necessary for the direction of the grating lines of the sample and reference to have been aligned in order for this to be true. If they are not aligned a constant amount of fringe is introduced representing the amount the lines are rotated with respect to reference.

Null Field Alignment

In aligning the null field a complex set of angular relationships must be met as dictated by the mirror adjustments, and the reference stage tilt. The null field alignment (NFA) begins by placing a reference grating in the sample stage and positioning the stage such that the all four beams emerging from the PEMI intersect in the plane of the grating. The area of intersection is maximized to maximize the area over which a fringe pattern will be obtained. Above it was

mentioned that congruent angular relationships were required between the sample and the impinging beams to align the null field. Clearly, it is possible to maintain a mutually equiangular relationship between the four beams and still have incongruent angles between each of the beams and the plane of the sample if the sample is slightly tilted. Thus, it becomes necessary to control not only the mirror angles but also the sample tilt and for reasons *supra*, sample rotation.

Sample Tilt and Rotation Adjustment

The PEMI has an additional component not shown in Figure 2.4, a sample tilt and rotation control mechanism. It is simply a white plate the center from which the laser light emerges normal to the plate before entering the polarizer. The utility of this plate in controlling sample tilt and rotation stems from the fact that by design not only does the primary diffraction order from the sample diffract in the direction of the camera, but there is a secondary diffraction order which diffracts back to the redirection mirrors collinear with the incident light. This reflected order then returns to the permanent grating and by the same path as the original beam from the laser (but in reverse direction) travels toward the plate from which the light emerges. When the sample has the proper rotation and tilt for a specific beam, the reflected diffraction order returns to the point on the plate from which it originally emerged. Otherwise a red spot representing the diffraction order is observed on the plate. The rotation and tilt must be adjusted on the sample stage such that dot passes through the origination orifice. This step must be conducted simultaneously for all four beams in order to insure that they have the same equiangular relationship with the sample.

Supposing that the original angular relationship between the four beams impinging on the samples is slightly non-congruent, then it is necessary to adjust them which in turn changes their relative relationships with respect to the grating plane. This tautological problem can only be solved by looking at one additional segment of information--the reference grating fringe pattern. Note that when interrogating the reference grating we would like to see no fringes since the reference represents essentially zero deformation. Thus by minimizing fringes and iteratively making fine adjustments to the mirrors and sample stage it is possible to satisfy all the conditions for null field alignment: rotational alignment, minimized fringes and equiangular relationship between incident beams and grating plane. Upon completion of the null field alignment typically ~1 fringe is present in the fringe pattern and all the reflection diffraction orders pass through the origination orifice.

Virtual Gratings in Null Field Alignment

Previously in section 2.3.1 it was shown that intersecting monochromatic light would create the periodic structure of interference shown in Figure 2.1. Furthermore, it can be shown that for plane polarized light impinging on a grating sample that in the null field state the frequency of the two beams interference will be exactly twice that of the physical grating. The interference pattern created in the plane of the grating has been named the “virtual grating”. Thus historically as an instructive technique a causal relationship has been established between the establishment of the 2:1 virtual fringe frequency ratio and null field alignment. Although, the conclusion of this requirement is sometimes correct, the logic by which the conclusion is derived is flawed.

The proper explanation is that the presence of the virtual grating is that with the proper virtual grating frequency just happens to coincide with the angle required for null field alignment. As further proof consider the following thought experiment where the angles between two incident beams is proper and the null field is aligned. True, if the two beams happen to be plane polarized, the “virtual grating” will have twice the frequency of the reference grating. If the sample is tilted about the normal to the plane orthogonal to the virtual grating, the null field is no longer aligned yet the virtual grating is still present at twice the frequency of the grating.

A further point is that moiré interferometry has no intrinsic requirement that a virtual grating be present at all in order to obtain a fringe pattern. If the two beams impinging upon a sample are polarized in identical directions, but those directions are not coplanar then the two will produce no virtual grating. Upon diffraction normal to the surface or slightly off normal they will interfere with one another to create a fringe pattern identical to one created by two beams which created a virtual grating with everything else held constant. A more thorough discussion of this can be found in *High Sensitivity Moiré*⁴. Thus, the virtual gratings should be viewed as an instructive conceptual tool.

Specimen Analysis

After aligning the null field it is possible to analyze a sample and be insured that the resulting fringe pattern is related directly to the difference in frequency between the two orthogonal families of lines in the sample grating and reference grating. The sample is placed on the sample stage similarly to the reference grating in null field alignment. Null field alignment essentially determined the mirror angles which the null field was aligned. In specimen analysis the mirrors are not adjusted as they represent the calibrated angles related to the reference. The sample, however must be tilted and rotated such that the reflection orders pass through the origination orifice on the white alignment plate. Further adjustments to rotation must be made with *a priori* knowledge about the symmetries of a particular deformation or simply by minimizing the total number of fringes in the pattern. This adjustment is called rigid body rotation or carrier adjustment. After making this adjustment the resulting fringe pattern represents the displacement from the center of the fringe pattern which was defined uniquely by the carrier adjustment.

Fringe patterns typically analyze deformation in on planar direction, thus only two beams are used concurrently in producing fringe patterns. Each of the beams interact only with one family of grating lines and that family is the one running orthogonal to the projection of the direction of light incidence on the plane of the grating. Thus in considering the change of frequency in a family of grating lines, it is necessary only to interrogate the specimen with the two beams satisfying this criteria. This leads to the production of a U-field and V-field fringe pattern corresponding to the deformation in the horizontal (x) and vertical (y) directions respectively. The following section describes the simplest method of obtaining strain information from fringe patterns, manual analysis.

2.3 Manual Strain Analysis

The theory underlying manual strain calculations is simple and well established. Since each fringe represents a unit of displacement (417 nm) then it is fair to say that the displacement incurred from one fringe to an adjacent fringe is also 417 nm. Thus we can define an area of interest of known actual dimension and by counting the number of fringes in that area we essential tabulate the amount of displacement per unit of length. Such an element is shown below in Figure 2.6. It is also useful to observe that for perfectly normal strain the fringe pattern would exhibit

perfectly vertical and horizontal lines for U-field and V-field fringe patterns respectively. This fact is demonstrated by the fringe pattern for a thermally strained aluminum specimen in Figure 2.7.

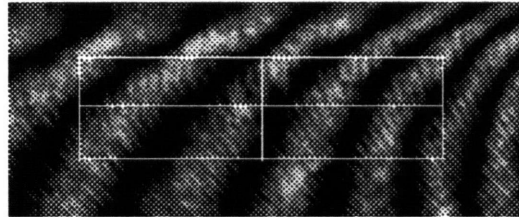


Figure 2.6-U-field fringe pattern exhibiting both normal and shear strains. A sample element has been drawn for manual analysis.

When shear strain components are present the fringes will become slanted denoting that the strain is a mixture of shear and normal strain components. By assigning fringe orders or number to each fringe in a sequential manner the strain can be related by the equations for Eulerian strain,

$$\begin{aligned} \varepsilon_x &= \frac{1}{f_{reference}} \left[\frac{\partial N_x}{\partial x} \right] \\ \varepsilon_y &= \frac{1}{f_{reference}} \left[\frac{\partial N_y}{\partial y} \right] \\ \gamma_{xy} &= \frac{1}{f_{reference}} \left[\frac{\partial N_x}{\partial y} + \frac{\partial N_y}{\partial x} \right] \end{aligned} \tag{2-3,4,5}$$

where $f_{reference}$ is 1200 lines/mm and ∂N_i is the change of fringe order N in the direction i . Note that the shear strain requires both the U-field and V-field components of strain to complete equation (2-5). Counting the fringe change across the perpendicular bisectors of the element in Figure 2.6 yields, $\partial N_x \sim 4.1$, and $\partial N_y \sim 0.8$. Clearly, the percentage of interpretation error diminishes with higher fringe densities. Generally as the number of fringes across an element decreases to less than $\sim 1/2$ the fringe counting error becomes dominant and the manually calculated strain values become unreliable.

One method of increasing fringe density is to use intentionally mismatched reference gratings which differ from the sample reference grating by a known amount which can subsequently be subtracted out from the strain value. This technique was not used here, but could

be readily implemented without changing the sample by obtaining a different reference grating (of different frequency), realigning the null field for the new frequency and re-analyzing the sample. The mismatch or carrier fringes should then be subtracted to obtain the actual strain. Another more automated means of interpreting fringe patterns is by computational analysis of digitized fringe patterns. The computational technique, discussed in the next section, provides nearly continuous strain information in contrast to the discrete average strain values provided by manual strain analysis.

2.4 Computational Moiré Strain Analysis

Generally the concept of computational analysis of moiré fringe patterns is centered around a single process flow. The first step involves filtering of the raw image, in addition to the removal of any mismatch (carrier) fringes present. Then the fringe pattern is interpreted with respect to the spatial phase distribution represented by the fringe locations. This operation yields a phase map or when multiplied by the grating constant, a displacement map. Since the information of interest is in fact the spatial change of displacement the data is then differentiated and smoothed. The resulting output is a strain map representing the strain present in the underlying specimen and any error incurred in the subsequent image processing steps. All computational techniques follow this general approach in obtaining strain information.

2.4.1 Computational Fringe Analysis History

As digital imaging have become available to experimentalists in the 1980s with the resolution to provide enough fringe pixel information for accurate data reduction, a multitude of methods for analysis of interferometric fringe patterns were developed. The data reduction at first was limited by the relative scarcity of inexpensive computing power in which to manipulate the large strings of image data, however this obstacle has become a non-sequitur. In general two schools of thought evolved with respect to how the relatively imperfect experimentally obtained interference fringes could be transformed into an analytical representation of underlying displacements. The first method, fringe tracing, identifies the fringe edges and interpolates the phase information between them, while the second essentially assigns phase in a continuous manner through a signal processing technique known as phase unwrapping. A variation on the first identifies the precise location of a fringes light and dark regions and linearly interpolates phase

between them. The evolution of computational fringe analysis is somewhat convoluted and intertwined as researchers mixed and matched different techniques to find the optimum solution.

Before attempting either of these two phase extraction processes it is necessary to preprocess the image information to eliminate the high frequency and low frequency noise from the image. Takeda *et al*^{5,6} was the first to demonstrate the application of Fourier transforms to Michelson Interferometry fringe patterns. Takeda was also integral in demonstrating the subtraction of artificially introduced mismatch (carrier) using the Fourier techniques. Increased fringe densities obtained by mismatch improved the statistical resolution of the fringe patterns. The technique was then applied to geometric moiré and moiré interferometry by Morimoto *et al*⁷⁻¹⁶ and Guo *et al*¹⁷ in a series of papers dealing with moiré mismatch and grid methods.

Concurrently, Morgan¹⁸ and Mertz¹⁹ developed alternatives to the phase-unwrapping step through sinusoidal fitting methods of interpreting intensity profiles. Voloshin²⁰⁻²¹ then adapted Mertz's method by using no mismatch (carrier) and introducing fractional fringe interpolation techniques to interpret phase. The phase-step method (PSM) based on the subtraction of several different phase-shifted fringe patterns of the same area of interest has become popular with many authors contributing work, among them, Kreith²², Marco *et al*²³ and Shield *et al*^{24,25}. This approach is reported to decrease background noise and increase spatial fringe resolution. Seemingly countless studies have documented the performance of the various noise reduction and data manipulation techniques in the last 15 years²⁶⁻³⁷. They all attempt to come to grips with the ubiquitous problem of spatial phase interpretation in the face of noise, discontinuities and other anomalies.

Perhaps the most popular combination of filtering and phase interpretation techniques is Fourier transform and phase unwrapping. The weakness being the long range propagation of phase unwrap errors which is carried through to the outputted strain map. Recently, Singh and Sirkis³⁸ demonstrated a marked improvement to phase unwrapping by differential cross multiplication (DCM), a technique used in fiber optic sensors derived from work by Morgan¹⁸. DCM exhibited no long range error propagation and yielded the same continuous strain data as the phase unwrap algorithm. Other experimentalists have attempted to minimize or eliminate the endemic error associated with phase unwrapping by introducing phase unwrapping algorithms that

interpret piecewise regions and have path independence requirements^{39,40}. These strategies involve more complex algorithms and require greater computing power to execute, but have demonstrated promise.

Until recently the algorithms for fringe interpretation have been developed independently by researchers who pieced together different algorithms to achieve the desired affect. In the last year, researchers at the University of Osaka in Japan lead by Morimoto have assembled a group of algorithms in a UNIX windows based package specifically for the interpretation of fringe patterns. The contents and theory behind the set of algorithms comprising Computational Fringe Analysis (CAFRAN) is given in the next section.

2.4.2 Theoretical Foundation of CAFRAN

Though the version of CAFRAN implemented in this study was a Beta version of the program, it contained all the necessary algorithms with which to filter and subsequently interpret the fringe patterns. As an overview, CAFRAN uses Fast Fourier Transforms to filter and remove carrier from the fringe patterns. The phase is then interpreted by arctangent phase wrapping and the strain maps are then produced by differentiation of the displacement map.

Historically, the first additive FFT algorithm was described by the work J.W. Cooley and J. W. Tukey⁴¹ in 1965. The straightforward computation of an N-point Fast Fourier Transform (FFT) requires a number of arithmetic operations proportional to N^2 . In many scientific and engineering applications this becomes too computationally intensive for the most readily available computing resources. The Cooley-Tukey algorithm significantly reduced the computational cost to be proportional to $N \log N$ --a figure more manageable for standard computers. This contribution has made it possible to apply CAFRAN to moiré fringe patterns with computation times of less than 30 seconds on an IBM RS6000 Model 590 workstation.

Considering a fringe pattern such as the one shown in Figure 2.7(a) which represents accumulated strain in the specimen from the temperature of grating application in addition to any carrier fringes intrinsically present. In this case we observe a sample which has had the grating applied at higher temperature and has been allowed to cool to room temperature.

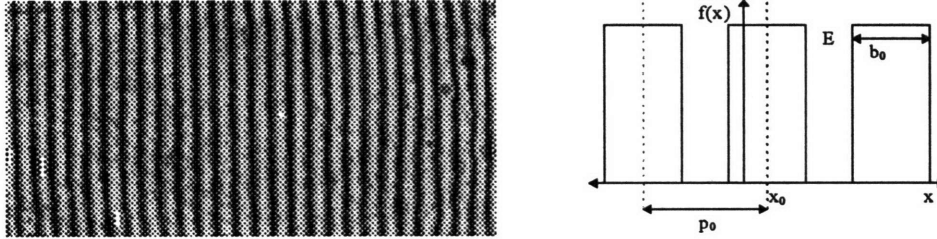


Figure 2.7-(a) Fringe pattern of normal strain in bulk aluminum (b)the intensity profile for a fringe pattern such as the one found in (a).

The intensity profile is given by $f(x)$ as shown in Figure 2.7(b) with a fringe pitch, p_0 related to ω_0 , the frequency by $p_0=1/\omega_0$. The fringe pattern itself consists of alternating bright and dark lines related to the total amount of deformation the sample grating has undergone from its original dimensions (assuming no carrier or reference grating mismatch). We offer only a one dimensional model here but the concept is identical in the 2D case—though the mathematics becomes much more cumbersome in 2D FFTs. The one dimensional expansion of the intensity profile in Figure 2.7 would then become

$$f(x) = \sum_{n=-\infty}^{+\infty} C_n \exp\left[\frac{2n\pi}{p_0}i(x - x_0)\right] \quad (2-6)$$

$$f(x) = \sum_{n=-\infty}^{+\infty} C_n \exp[i2n\pi\omega_0(x - x_0)] \quad (2-7)$$

where C_n , the Fourier coefficient is defined as,

$$C_n = C_0 \sin\left(\frac{b_0 n \pi}{p_0}\right) \bigg/ \left(\frac{b_0 n \pi}{p_0}\right) \quad (2-8)$$

and $C_0=Eb_0/p_0$ where E is the normalized intensity. To appropriately weight phase change represented by the bright region within each periodic unit a fringe opening ratio must be defined where,

$$\alpha = b_0/p_0 \quad (2-9)$$

from Figure 2.7, b_0 is the fringe width and p_0 is fringe pitch. Substituting the function $h_n(x)$ where

$$h_n(x) = C_n \exp[-i2\pi n \omega_0 x_0] \quad (2-10)$$

yields

$$f(x) = \sum_{n=-\infty}^{+\infty} C_n \exp[i2\pi n\omega_0 x] \exp[-i2\pi n\omega_0 x_0] \quad (2-11)$$

$$= \sum_{n=-\infty}^{+\infty} h_n(x) \exp[i2\pi n\omega_0 x] \quad (2-12)$$

Performing a Fourier transform on the fringe pattern intensity function $f(x)$ and subsequently substituting $h_n(x)$ from (2-10) yields,

$$F(\Omega) = \int_{-\infty}^{+\infty} f(x) \exp(-i2\pi\Omega x) dx \quad (2-13)$$

$$= \int_{-\infty}^{+\infty} \sum_{n=-\infty}^{+\infty} h_n(x) \exp[i2\pi n\omega_0 x] \exp[-i2\pi n\Omega x] dx \quad (2-14)$$

Next we are able to show that by swapping the order of summation and integration we are left with the Fourier transform of $h_n(x)$

$$F(\Omega) = \sum_{n=-\infty}^{+\infty} \int_{-\infty}^{+\infty} h_n(x) \exp[i2\pi n\omega_0 x] \exp[-i2\pi n\Omega x] dx \quad (2-15)$$

$$= \sum_{n=-\infty}^{+\infty} \int_{-\infty}^{+\infty} h_n(x) \exp[-2i\pi x(\Omega - n\omega_0)] dx \quad (2-16)$$

which is then,

$$F(\Omega) = \sum_{n=-\infty}^{+\infty} H_n(\Omega - n\omega_0) \quad (2-17)$$

The power function $F(\Omega)$ (shown below) is a representation of the fringe pattern in phase space. The 2D FFT in CAFRAN plots the vertical and horizontal frequency components simultaneously such that a structure with a first harmonic in direction x at ω_1 and a first harmonic in orthogonal direction y at ω_2 would be plotted at point (ω_1, ω_2) in 2D phase space with the intensity of each one dimensional power function being transformed into a normalized gray scale intensity value. Figure 2.8 below shows the 2D FFT for a sample at two different temperatures representing two distinct strain states.

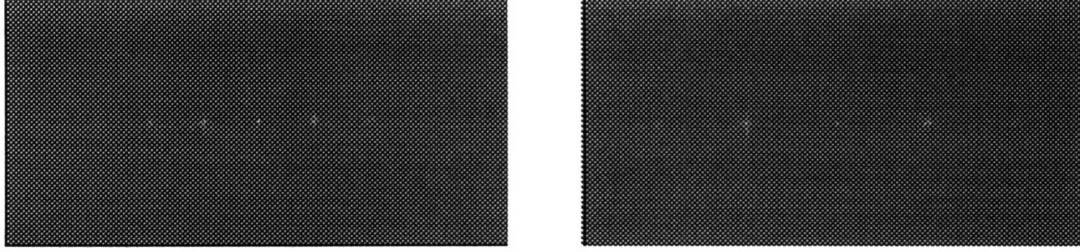


Figure 2.8-(a) 2D FFT representation of sample at lower strain (b) 2D FFT representation of same sample after a finite amount of thermal strain accumulation. Note that these samples exhibit only uniaxial strain as the harmonics exhibit only x-directional periodicity.

Within CAFRAN the first harmonic and the surrounding distribution of phase information are extracted from the higher harmonics and noise in the spectrum. The isolated or filtered first harmonics can then be inverse transformed to recreated the original fringe patterns now smoothed by the FFT filtering. The inverse transform of the 2D power function with isolated first harmonic is given by

$$h_1(x) = \int_{-\infty}^{+\infty} H_1(\Omega - \omega_0) \exp(i2\pi\Omega x) d\Omega \quad (2-18)$$

$$h_1(x) = h_1(x) \exp(-i2\pi x(\omega_0)) \quad (2-19)$$

then substituting for $h_1(x)$ from equation (5) gives

$$h_1(x) = C_1 \exp(-i2\pi\omega_0 x_0) \exp(-i2\pi\omega_0 x) \quad (2-20)$$

consolidating terms yields,

$$h_1(x) = C_1 \exp(-i2\pi\omega_0(x + x_0)) \quad (2-21)$$

This intensity profile derived from the first harmonic of the fringe pattern is more simply manipulated by

$$h_1(x) = C_1 \exp(i\theta_1) \quad (2-22)$$

where

$$\theta_1(x) = -2\pi\omega_0(x + x_0) \quad (2-23)$$

and $h_1(x)$ is a complex moiré displacement fringe pattern reconstructed by the inverse transform of the first harmonic. The smoothing of the fringe pattern is resultant from the elimination of higher frequency noise and lower frequency background noise. The intensity profile of the fringes are smoother and are more easily and accurately interpreted by a phase-unwrapping algorithm. The real and imaginary components of the complex fringe pattern are given by

$$\text{Re}\{h_1(x)\} = C_1 \cos \theta_1 \quad (2-24)$$

$$\text{Im}\{h_1(x)\} = C_1 \sin \theta_1 \quad (2-25)$$

Using the real and imaginary components of the sinusoidally varying intensity functions of the fringe patterns the arctangent function can be used to compute a cumulative phase value across the fringe pattern. The phase is then defined by

$$\theta(x) = \tan^{-1} \left[\frac{\text{Im}\{h_1(x)\}}{\text{Re}\{h_1(x)\}} \right] \quad (2-26)$$

For two fringe patterns representing two different levels of thermal strain, the phase will differ by the amount of strain accumulated or lost in heating or cooling from one fringe pattern's temperature to the other. Thus we can define the phase for fringe pattern A and B, θ_A and θ_B respectively with pattern A having the higher total strain. The difference between the phase of the patterns is then given by $\phi(x)$ where

$$\phi(x) = \theta_A(x) - \theta_B(x) \quad (2-27)$$

Indeed it is not the phase directly that is of interest in determining the strain since for strain we are interested in the change in length per unit of length. The phase itself is the cumulative displacement function of the sample and must therefore be differentiated to yield the change in displacement per pixel (the smallest unit possible in digital images). The Eulerian strain can be shown by

$$\varepsilon(x) = \left[\frac{\Delta\phi(x) \text{ radians}}{(\Delta x) \text{ pixels}} \right] \left[0.417 \frac{\mu\text{m}}{\text{fringe}} \right] \left[\frac{1 \text{ fringe}}{2\pi \text{ radians}} \right] \left[\frac{N \text{ pixels}}{X \mu\text{m}} \right] \quad (2-28)$$

where X is the actual distance covered by the image in the direction of interpretation and N is the number of pixels in the image in that direction. A moving average smoothing function is generally applied after the differentiation step to minimize high frequency noise which may still be present due to fringe edge roughness and anomalous intensity function shape variations. CAFRAN does not allow the introduction of dimension into the computation and as a result the output values are in terms of radians/pixel. These values can be converted to strain using a simple spreadsheet model and equation (2-28). The strain maps produced by this technique are shown in Chapter 7.

Chapter 3

General Experimental

3.1 Introduction

The analysis of strain using moiré for many years was limited not by a lack of technical knowledge about the mechanics of interferometry or data analysis, but by something even more rudimentary: reproducible diffraction gratings. In the last two years IBM has introduced a prefabricated moiré interferometer (PEMI) and has developed a method of producing diffraction gratings with frequencies of 1200 line/mm on ultra low expansion glass. This has eliminated difficulties in maintaining consistent grating quality and frequency and has allowed the independent researcher to focus on the rudimentary sample preparation issues relevant to the sample under investigation. All fringe patterns used in the study were collected on a PEMI-2010-X purchased from IBM Photomechanics Division in Endicott, NY. The work was completed in the Mechanical Thermal Laboratory in the Chandler, Arizona Assembly Technology Development Division. There exist some natural and recurring procedures in the moiré sample preparation protocol. These ubiquitous event will be described here in the General Experimental section. Each sample contained it's own individual sample preparation requirements related to the specific strain state, area of interest or material set in use. Therefore subsequent chapters will include an experimental section to describe the variations and nuances involved in preparing each distinct package type.

3.2 Equipment/Lab Setup

Early on in the project the work was being conducted in several labs, but after roughly two months all of the processes involved in moiré were moved and consolidated into one workspace. Generally this includes the interferometer, an oven for grating application, a fume hood and a personal computer. The only remaining step which was not localized was cross-sectioning, but the much of the efficiency gain in data acquisition has been captured by centralizing the other process steps.

3.2.1 Portable Engineering Moiré Interferometer (PEMI)

The moiré interferometer obtained from IBM-photomechanics, shown below in Figure 3.1, has dimensions of 30 X 30 X 18 cm and weighs roughly 23 kg. The maximum area in which all the beams can be made to superimpose one another on a sample is a circle with a 4.5 cm diameter.

The sample stage or thermal chamber (not shown in Figure 3.1) was positioned such that the samples could be placed in the plane of the mutually intersecting beams emerging from the PEMI ports. The covers for the ports were magnetically attached to the rotating face plate allowing anywhere from zero to four beam interrogation of the specimen. The laser used to create the interference was a class II helium neon laser ($\lambda=632$ nm) with a 10-15 milliwatt output power.

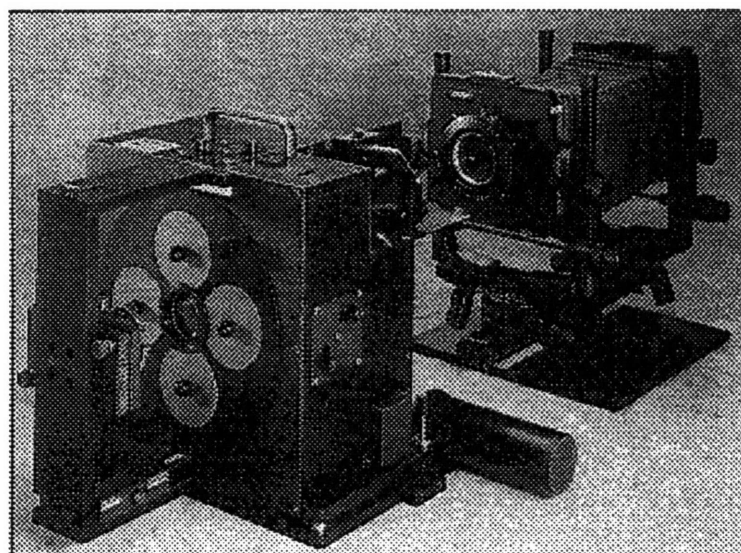


Figure 3.1-Portable Engineering Moiré Interferometer and Polaroid Camera.

As described in Chapter 2 the PEMI was calibrated for each reference grating. This was done by adjusting the knobs on the top and side of the interferometer which control the angle at which the interferometer directs the beams towards the sample. The mirror and their role in the PEMI structure is shown in the figure below (Post *et al*). From equation (2-1) the frequency of the virtual grating can be adjusted to obtain the null field. The details of this procedure will be given later in this chapter.

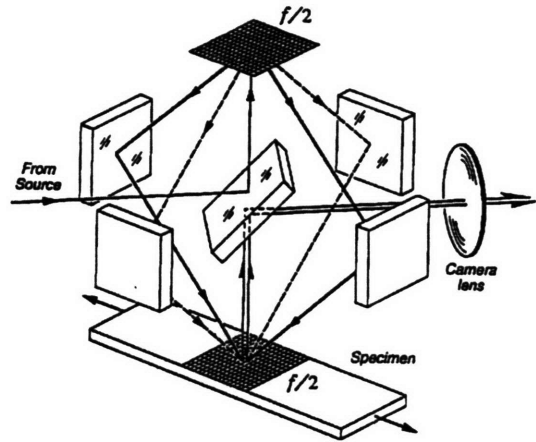


Figure 3.2-Skeletal representation of the optical elements comprising the PEMI.

Another consideration with such sensitive measurements based on displacement of a small region of a sample with respect to a calibrated center or neutral point is vibration. Vibration of the entire sample, PEMI and camera assembly would not affect the quality or accuracy of fringe patterns obtained if the vibration were experienced in unison. This requirement is impossible to achieve in a real system with the suspended adjustable mirrors within the PEMI and mechanically decoupled camera and sample stages. Therefore, to eliminate much of the lower and mid frequency vibration from surrounding laboratory activities the entire assembly was placed on a pneumatic isolation table. The entire system is shown below in Figure 3.3.

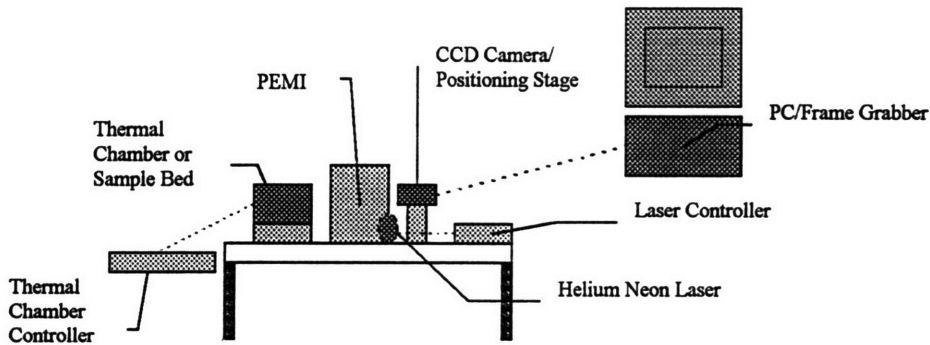


Figure 3.3-Schematic representation of the moiré and data acquisition setup.

3.2.2 Thermal Chamber and Temperature Controller

Many of the analyses required the variation of temperature or thermal load of the specimens. Clearly the resolution and uniformity of the temperature control is of utmost

importance to avoid ambiguity in the strain measurements. An environment chamber was obtained from the University of Texas at Austin to hold the moiré samples at specified temperatures for data collection. In all cases the temperature was assumed to be and intended to be uniform. A diagram of the thermal chamber design is shown below in figure 3.4.

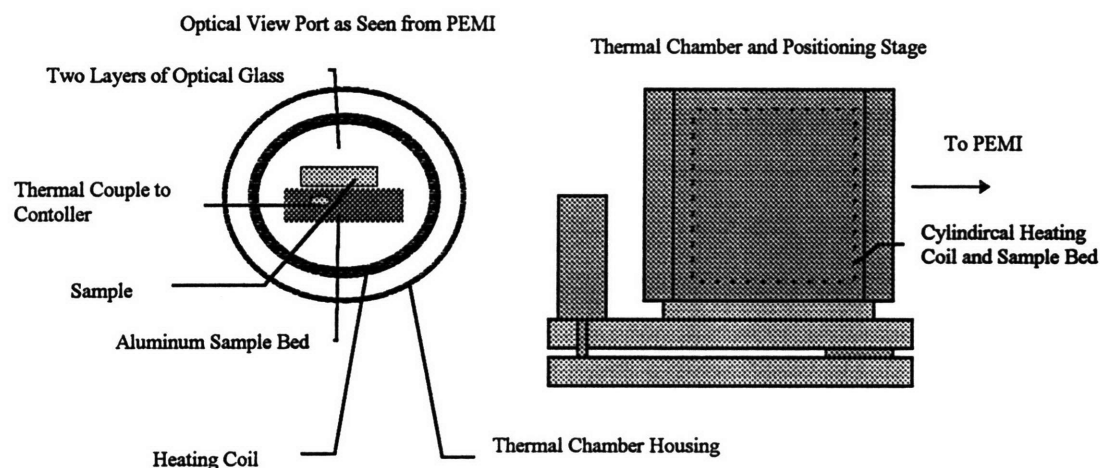


Figure 3.4-Front (left) and side (right) view of the moiré thermal chamber.

The thermal chamber temperature was controlled by a self-adaptive tuned Eurotherm temperature controller which controlled the current to the heating coil. All temperature dependent tests were conducted by heating the sample to above 104 °C and allowing the chamber to air cool to room temperature. It was noted that gradients of ~8-9 °C between the heating coil temperature sometimes persisted upon cooling below 60 °C. Since the sample bed was constructed of thermally conductive aluminum and the sample was mounted directly on that bed they could be assumed to be at the same temperature. The thermocouple from which the temperature measurements was positioned about the same distance as the sample center suspended in the air surround the sample bed. The sample bed thermocouple was connected to the Eurotherm controller to drive the feedback loop. Direct measurements of the sample temperature using Kapton tape attached thermal couples showed that the package never deviated in temperature from the suspended thermocouple by more than ~1.5 °C.

3.2.3 Image Recording System

Initially images were captured using the diaphragm Polaroid camera (0.8X-8X mag) shown in Figure 3.1, but it was determined that satisfactory resolution could be obtained using a

series of lenses and a Pulnix TM-7CN CCD camera to acquire the interference pattern images. The Polaroid camera was cumbersome to focus and convert into digital information for computational strain analysis. In general the Polaroid camera could produce higher quality images albeit at a much slower rate of acquisition.

The charge-coupled display (CCD) camera used had a 1/3" chip with a resolution of 768 x 494 and a variable electronic shutter. The interlaced image output from the camera was captured to a Correco frame grabber for manipulation and storage. Since the image was interlaced it was important that no movement occurred in the system between camera interlace steps or a blurred image would result. In this respect the isolation table was entirely necessary since even the slightest movement during the image capturing process would render the image unusable.

Several combinations of lenses were implemented in obtaining the precise magnification desired for a given analysis. The CCD camera was fitted with a c-mount to allow standard camera lenses to be used. A 70-108mm zoom macro, 90mm macro and 200mm macro in combination with two 2X TV lenses were all used to obtain the proper magnifications. The magnifications ranged from 8X to 40X in this study. An xyz stage with yaw and y-rotational adjustment were designed and built to position the camera and lens setup since the fringe pattern image emerging from the PEMI was often directed to a slightly different position in the plane of the CCD camera chip.

Once the camera was positioned and the image was focused Image Pro-Plus 1.3 (Media Cybernetics), an image capturing and processing software program, was used to capture the image and save it. An electronic shutter controller on the camera as well as the software driven contrast, brightness and nonlinear response controller on the framegrabber card were used to obtain bright and well contrasted images. For manual analysis the image was enlarged with constant aspect ratio to fit an 8.5" X 11" page and was outputted to a laser printer. These hardcopy images were then used for the manual analysis calculations described in Chapter 2. Computationally analyzed images underwent other processing and file formatting which will be discussed in more detail later.

3.2.4 Oven and Fume Hood

The moiré grating replication on samples requires the use of surface cleaning agent and upon grating removal from the master grating the photoresist must be removed to obtain a highly reflective surface. The grating application process was conducted in a standard laboratory fume hood. The oven used to cure the grating attach epoxy was a Blue M Electric Oven Model MP-256E positioned near the fume hood. A hot plate was positioned in the fume hood to help maintain the grating bed temperature as the epoxy was applied.

3.3 Sample Preparation

Perhaps some of the greatest challenges have been and continue to be obtaining reliable and reproducible moiré specimens. The advent of commercially available gratings has solved some of the variation with respect to grating quality, each case analysis requires slightly different techniques in order to obtain reliable results. The general process flow for a sample begins with cross-sectioning of the package along the plane of interest. Next, the epoxy is applied to the sample face of interest and placed face-down on the reference grating. Finally the sample and reference grating are heated to the desired cure temperature and then separated after mechanical bonding of the grating to the electronic package has occurred. The sample is then analyzed using the PEMI.

3.3.1 Electronic Package Cross-sectioning

In cross-sectioning of electronic packages it is necessary to consider that the information one wishes to obtain is that of the actual strain in a real package. Indeed, by cutting a package in half or at all the stress state of the package has already changed. This event is unavoidable, but should also not have a significant impact on the strain values measured. In hybrid finite element methods the model boundary conditions can reflect the package separation, thereby eliminating any error associated with this constraint. The introduction of artifacts such as structural damage, delamination and die cracking would however have dramatic and unavoidable influences on the strain values present. A direct comparison of cracked, and delaminated parts of a certain plastic packages illustrated that they had drastically different stress distributions than their undamaged and otherwise identical counterparts. Thus, in order to obtain meaningful results, damage to the specimens must be eliminated, because it's effect on the stress state can neither be quantified nor corrected. Toward this end three techniques of cutting we attempted: Diamond Saw, Allied SiC₄

Automated Feed Saw, and a LASTEC Reversing Wire Saw. The sectioning of the samples covered in this study was in all cases along a diagonal or perpendicular to the die edge as show below in Figure 3.5.

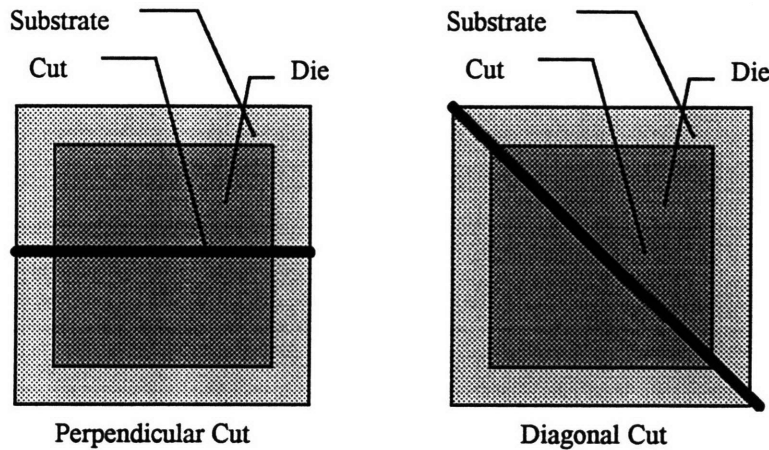


Figure 3.5-Planes of the cross-sectional cuts used in the die bonded substrate and PPGA studies.

These planes captured the highest strain values in the package as well as those which could be inserted easily in Finite Element Models for validation. Each cutting technique proved useful in cutting certain types of packages, they all exhibit essentially different trade-offs between cutting rate and stress-intensity related damage. The following three subsections will explore the observations in greater detail.

Rotary Diamond Saw

The first technique implemented to cut packages was using a conventional rotary diamond saw used to cut ceramics at other hard materials. The packages were oriented at a variety of angles and also at a variety of load and speed conditions. The best results were obtain with moderate load and speed and a 45 ° orientation of the sample with respect to the rotation direction. The technique overall was found to cause considerably more delamination in a plastic pin grid array package compared to other techniques. It cut land grid arrays satisfactorily, but it was difficult to make the cut through solder balls as required since alignment was not easily gauged and the blade was relatively wide. This technique was not used for final data collection but served as a basis of comparison for the other two techniques.

Allied Automatic Feed Saw

One of the weakness of the rotary diamond saw was that the blade tended to bind up in the copper heat slugs used in the package at slower speed and the blade was not designed to cut at higher speed to take advantage of the strain rate embrittlement of the copper. The allied automatic feed saw had a more robust fixture, larger motor and a 5" Si₄C blade rather than diamond. The cutting process appeared to cause less vibration and took less time, but in most cases die cracking and delamination in PPGA and die bonded to substrates were the failure modes. Only the LGA was successfully cut with confidence and even then the blade width consumed much of the solder balls which were of primary interest. This cutting process in general is superior to the rotary saw in two other respects as well: reproducibility of cuts and efficiency. Still this technique did not afford a method of reliably sectioning PPGA and die bonded substrate specimens.

Diamond Impregnated Wire Saw

After several months a diamond-impregnated-wire saw became available to the project. The amount of vibration caused by the cutting was significantly less than that for the first two techniques, though the cutting process took much longer. There were several parameters which dictated the outcome of the cut. A diagram of a portion of the wire saw is shown below in Figure 3.6. The primary parameters were: (1) wire travel speed (2) wire diameter and particle size distribution (3) cutting angle. Implicit within these conditions is that a given package is well fixtured and completely immobilized during the cutting process.

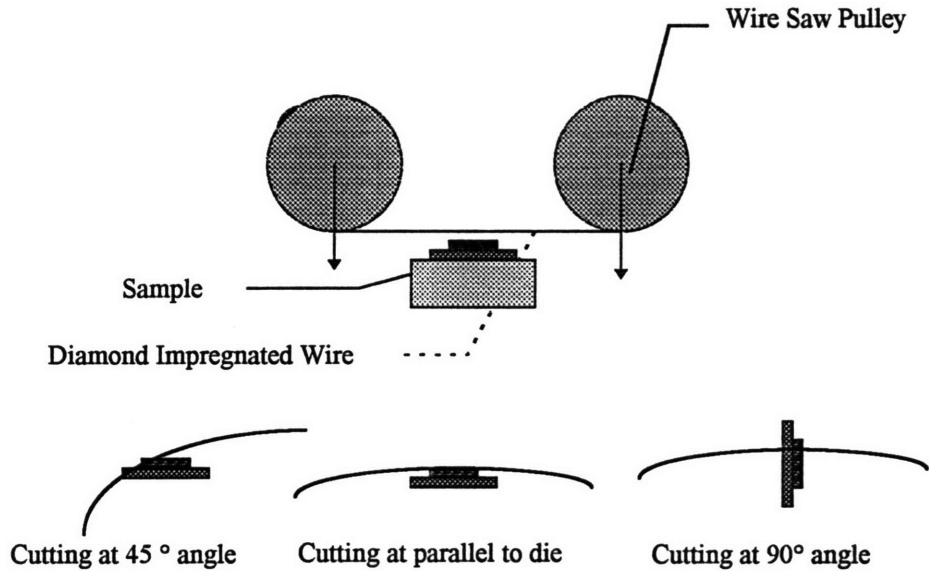


Figure 3.6-(top) Diagram of wire saw pulley mechanism. (bottom) Various orientations in which the packages were fixtured. Note that the wire arcing is highly exaggerated to for illustration purposes.

The wire used had a diameter of 0.010" and a particle distribution centered about 60 μm . It is expected that the 45° cut would cause less damage than the 0° and 90° orientations. The 0° cut appears to flex the die because of the slight wire arc, whereas the 90° cut appeared to cause high peel stresses leading to delamination. Notably, in no cases did the parts cut at 90° experience longitudinal die cracking experienced to varying degrees in the other two orientations. Nonetheless the wire saw technique was successful in cutting the die bonded to both organic and ceramic substrates.

Land Grid Array packages were also cut using this technique with very high yield. The wire was thin enough not to consume the entire solder ball width which made it possible to look at the solder balls on both sides of the cut. Less success was experienced with PPGA packages as the attempt to optimize the cutting technique was hampered by part supply, time constraints and other external factors. Only one PPGA package was cut without inducing at least one of the failure modes. The specific cutting parameters for each package are given in the following experimental focus sections.

Wafer Dicing Saw (Disco-HiTec America)

After encountering difficulties in sectioning parts with the wire saw a small set of attempts to cut parts using a wafer dicing saw were made. Clearly the saw itself is capable of cutting wafers without cracking them when they are not embedded within a package so it was presumed that any cracking observed would be caused by the presence of stress induced in the die by the surrounding package. Packages were embedded in wax on a wafer and then cut using a resin blade impregnated with ceramic particles. The PPGA cut in this manner exhibited very smooth, high quality cut surfaces with the same longitudinal die cracks pervasive in all the other techniques attempted.

3.3.2 Grating Attach Epoxies

The diffraction grating for moiré analysis is composed of a thin aluminum layer deposited on a patterned photoresist and an ultra low expansion glass. The cross-section and an SEM top view of a grating are shown below in Figure 3.7. It is necessary to use an epoxy that is higher in adhesive strength to the sample surface and aluminum layer than the photoresist is to the ULE glass and aluminum layer. This allows the removal or replication of the grating by failure in the photoresist layer while the grating structure remains intact. Once the grating is mechanically coupled to the sample surface, it is necessary that all displacements in the underlying sample material be mimicked in the thin epoxy and aluminum grating. The grating was typically applied at an elevated temperature such that a significant amount of accumulated strain was observable at room temperature.

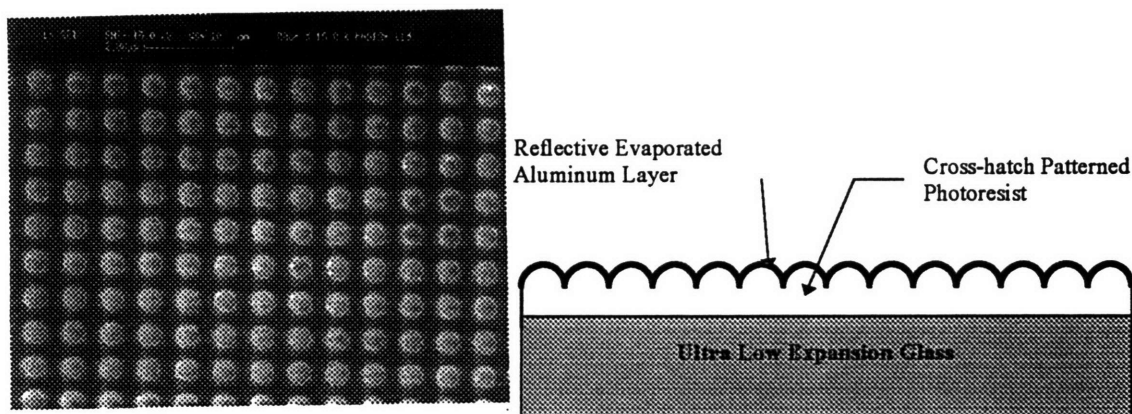


Figure 3.7-Scanning electron microscope image of 1200 line/mm grating used in the study (left), and a cross-section diagram of the ULE type gratings (right).

The necessity to measure strain at a temperature which is distanced by at least $\sim 20^{\circ}\text{C}$ from the grating application is driven by the increasingly dominant fractional fringe counting error noted in Chapter 2. At temperatures close to the mechanical coupling temperature, the number of fringes in these particular packages is small. The percentage of the total displacement value that a fractional fringe might represent is significant when the number of fringes is small and as an inherently imperfect measure it will have a deleterious effect on the precision of the measurement. Information about package strain is desired for all temperatures up to the stress free temperature $\sim 111^{\circ}\text{C}$ in the PPGA and at $\sim 180^{\circ}\text{C}$ for the die bonded substrate. The stress free state for the LGA is of course the solder reflow temperature. In order to capture contiguous strain information it would then be necessary to have applied the grating at one of the extremes of this $22\text{-}180^{\circ}\text{C}$ temperature range. To this end two different types of epoxies were tested using TMA and DMA to determine their thermal stability.

Since it is necessary to cycle the samples and gratings several times during the analysis process it is crucial that the epoxy undergo negligible amounts of plastic or creep deformation. The primary parameter used as a measure of resistance to thermally activated inelastic deformation mechanisms is the glass transition temperature (T_g) of the polymer. A relationship limiting an epoxy cured at room temperature is that the T_g is typically not significantly higher than the cure temperature in a resin-based epoxy. In addition if an epoxy were cured at a temperature below its designed cure temperature, subsequent heating would cause post-curing when excursions exceed the grating application temperature. Thus the tests were expected to yield information about the service temperature range for the epoxies so that the grating application temperatures that would allow continuous strain information could be chosen.

The two epoxies chosen for testing were Tra-Con F-114 Epoxy and Tra-Con F-230. They are both resin based epoxies. Thermal mechanical analysis (TMA) measures the CTE of the epoxy. As the resin passes through the T_g it undergoes a change in CTE. Dynamic mechanical analysis is a three point bend test used to monitor the Young's modulus. As the polymer goes through the T_g the modulus decreases dramatically. The table below gives the results of the tests which were conducted by an outside laboratory.

DMA Glass Transition Temperature (T_g) Results (°C)

	<u>Sample 1</u>	<u>Sample 2</u>	<u>Sample 3</u>	<u>Mean Value</u>
Tra-Con F-114	36.23	47.64	46.77	44.55
Tra-Con F-230	112.97	106.97	119.51	113.16

TMA Glass Transition Temperature (T_g) Results (°C)

	<u>Sample 1</u>	<u>Sample 2</u>	<u>Sample 3</u>	<u>Mean Value</u>
Tra-Con F-114	52.19	46.25	42.20	46.88
Tra-Con F-230	118.92	119.57	117.88	118.79

Table 3.1-Glass Transition Temperature test for grating attach epoxies.

Based on the results of these tests it was determined that if the gratings were attached under the same conditions as the samples in these experiments, they could be heated to temperatures ~5-10 °C below the T_g without experiencing significant plastic flow and hysteresis strain characteristics. The F-114 epoxy was never implemented, but the F-230 was used to acquire data starting at 90 °C and below for all the data in this study.

3.3.3 Diffraction Grating Application

The grating application process was dramatically improved at Intel through refinements to the sample mechanical support structures and other minor process changes. The gratings used were obtained from IBM-Photomechanics Division and had the specifications given in Table 3.2 below. After the samples were cross-sectioned they were then cleaned with acetone, covered with epoxy and placed on the grating for curing at the desired temperature. The Figure below depicts the grating sample bed used to provide thermal mass when the grating was removed from the oven and also to stabilize the sample in the oven as it cures.

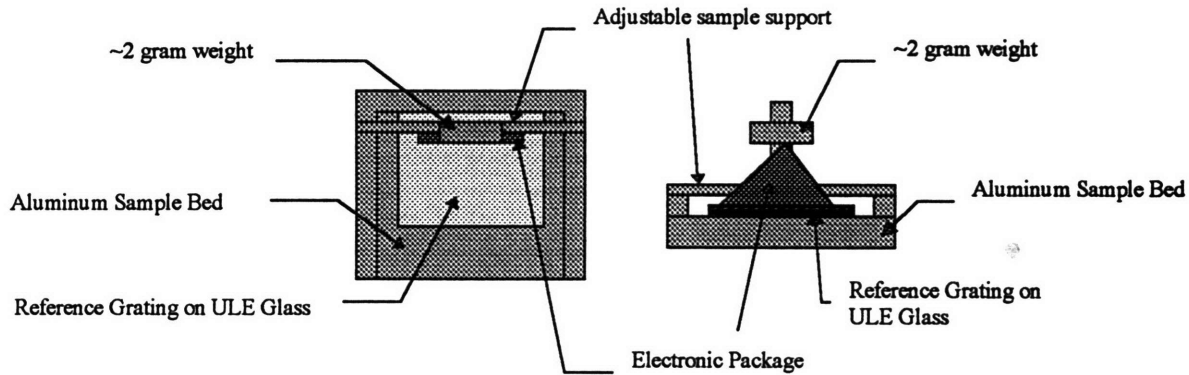


Figure 3.8-Grating application support bed from the top (left) and from the end (right).

After cross-sectioning, the sample is photographed under low magnification and the relevant package layer thicknesses are measured using a Beuchler Optical Microscope measuring system. This information is used later in navigating in the fringe pattern as well as providing a scale to the fringe pattern for strain calculations. When the wire-saw is used this step need not be preceded by a polishing step because the surface finish is of sufficiently high quality. A planar sample surface is required to ensure that the epoxy thickness is relatively homogenous and the sample receives full grating coverage.

IBM Ultra Low Expansion Glass Moiré Gratings

Pattern:	Crossed Lines
Frequency:	1200 lines/mm ($\pm 0.5\%$)
Diffraction Efficiency:	$\sim 15\%$
Intensity Variation:	$< 15\%$
Orthogonality:	$\pi/2 \pm 0.5 \times 10^{-4}$
Null-Field:	< 1 fringe
Temperature Range:	$T < 150^\circ \text{C}$
Grating Size	55 mm square

Table 3.2-Reference grating specifications.

Next, the sample surface is cleaned by swabbing the surface with a lint-free Q-tip dampened with acetone. Care should be used to clean the parts quickly as some components of electronic packages are miscible in acetone and it may degrade the structure. The sample is then dried with compressed air to drive off excess solvent. This step is completed in the laboratory fume hood.

All of the samples presented in this study were applied to the ULE grating at 104 °C. After cleaning the surface of the sample, the piece is then placed in a preheated oven with a constant temperature set to 104 °C. The sample bed with ULE grating and the sample are left in the oven for ~15 min to allow them to equilibrate in temperature. Simultaneously in a nearby fume hood, a hot plate is heated to 104 °C and Tra-Con F-230 epoxy is mixed on a glass plate for application to the sample. The sample and grating bed are removed from the oven and placed on the hot plate. Using a lint-free swab a thin layer of epoxy is spread over the sample and is placed carefully on the grating while attempting not to trap air bubbles underneath it. An alternative method illustrated below in Figure 3.9 shows the epoxy being spread over the grating. This technique produces similar quality gratings but tend to consume more master grating per specimen so the former method is more efficient in cost per sample terms.

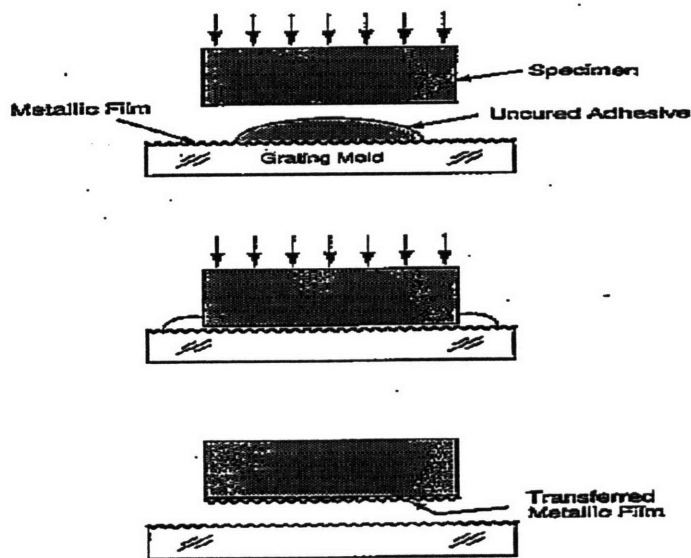


Figure 3.9-Conventional grating replication technique used exclusively for LGA samples in this study.

The adjustable support was positioned to place the sample on an unused part of the grating before the preheating step. Once the sample is in place it is pressed down firmly taking care not to slide it on the reference grating. This will remove air bubbles and insure the entire face is wetted. A ~2 gram weight is then placed on the upright sample support to provide a constant load during sample cure. The entire assembly (with sample) is then placed in the oven to cure for ~1 hour.

After 1 hour, the oven door is opened, and the adjustable sample support is slid away from the specimen which is now fully bonded to the ULE reference grating at 104 °C. Using gloved hands the sample is gently freed from the substrate by applying load to the sample corner (or edge) furthest from the ULE substrate in a direction parallel to the ULE substrate. Once the mechanical separation has occurred between the sample and the ULE substrate, the pieces may be removed from the oven for cooling.

The sample is allowed to air cool for 5-10 minutes and is then gently cleaned using a lint-free swab and isopropanol. After all residual photoresist has been removed the grating is swabbed and then quickly compressed air dried to remove residues that segregate on the grating during normal evaporation of the isopropanol. Using a sharp blade or fine sandpaper, the epoxy lip around the edges of the sample is removed so that only the sample face has grating on it, and the edges are clearly defined. The sample is now ready for analysis on the PEMI.

3.3.4 Failure Modes in Grating Replication

Before continuing a brief discussion of grating flaws is warranted since all subsequent steps rely upon the integrity and mechanical coupling of the diffraction grating to the sample. There are several sources of grating flaws which must be considered. If any of them are present the analysis may be either difficult to interpret or yield erroneous data.

[1] The first flaw is the absence of grating on the sample. Occasionally a region will exist where the epoxy adhesive failed rather than the photoresist and the grating will remain on the substrate. This causes difficulties in interpreting strain if the grating hole coincides with an area of interest.

[2] Second is delamination of a grating due to thermal cycling or peel loading. If care is not taken when cleaning the edges of the sample to compress the epoxy/sample structure rather than placing it in tension, delamination could occur. Delamination is essentially mechanical decoupling of the grating from the sample and renders the data inaccurate.

[3] The third consideration is shear lag⁴—a term used to describe the nonlinear response of the grating free surface to large strain gradients. If epoxy and grating thickness is more than about ~25 μm or exhibits significant variation in thickness the true magnitude of strain may be slightly

attenuated near singularities or high strain gradient regions. The region of attenuation is typically no more than a few tens of microns from a strain singularity. To insure that the bond line thickness (BLT) of the epoxy was thin and uniform, a ~2 gram weight was placed on the sample during the cure step in grating replication. This was intended to be an extra measure to protect against BLT variation and shear lag.

3.4 PEMI Calibration and Specimen Analysis

Although the tolerance for each ULE grating is relatively high, it is still necessary to calibrate the PEMI with the master grating from which the sample to be analyzed is taken. In this section the process of calibrating the PEMI mirror or null field alignment as well as the actual acquisition of sample fringe patterns will be detailed. References to Sections (section on null field and carrier minimization) in Chapter 2 will be made rather than attempting to reiterate the complex set of physical conditions required for interference patterns to be created.

3.4.1 Null Field Alignment

The alignment of the PEMI mirror to obtain a null field is analogous to any other calibration process, it requires a reference with a known characteristic. In moiré that constant characteristic is the frequency of the reference grating. It is known that the grating at the time of application to the sample had an identical frequency to the master grating. As it was shown in Chapter 2 the PEMI fringe pattern represents the local deviation in grating frequency in the sample as compared to the reference grating. We essentially lock in the reference grating frequency through the positioning of the mirrors in the null field alignment.

The PEMI creates fringe patterns by directing two mutually coherent beams of light towards the sample grating at identical angles of incidence. By knowing the wavelength of light and the frequency of the original grating we can calculate the angle of incidence that is required quite accurately. In fact the angle of incidence chosen during the calibration process will yield a diffraction order from each beam which is exactly normal to the sample surface. Since these two primary diffraction orders leaving the reference specimen normal are mutually parallel they will not interfere with one another destructively. A close approximation of what this angle actually is found by solving the diffraction equation below for a reference grating frequency, f_{sample} and laser wavelength λ .

$$\sin \beta_m = \sin \alpha + m \lambda f_{sample} \quad (1)$$

where $\lambda=633 \times 10^{-9} \text{m}$ and $f_{sample} \sim 1200 \text{ m}^{-1}$. For diffraction normal to the specimen $\beta_1=0^\circ$ yielding,

$$\sin \alpha = -(\lambda) \cdot (f_{sample}) \quad (2)$$

$$\alpha = \pm 49.42^\circ \quad (3)$$

But if the sample being analyzed has a slightly different grating frequency a different laser beam incident angle (α) would be required for the two primary diffraction orders to emerge exactly normal and mutually parallel. After calibration or null field alignment, the mirrors are not adjusted and the incident angle is held constant so the two primary diffraction orders will emerge at a small angle from exactly normal when a strained sample is interrogated. This allows the two to destructively interfere with each other and create an interference pattern which is linked to the angles between the two primary diffraction orders. This creates an pattern of constructive and destructive interference or an interference fringe pattern. Since the periodicity of this fringe pattern is linked to the angle of separation between the emerging beams and that angle is linked to the local frequency of the grating from which the light diffracted, the fringe pattern tells us the difference between the local frequency and the reference grating frequency of ~ 1200 lines/mm. The figure below illustrates diffraction under proper null field alignment. The sample is from the reference grating for which the PEMI was calibrated. A more in-depth discussion of the numerous diffraction phenomena in the PEMI is given in Chapter 2.

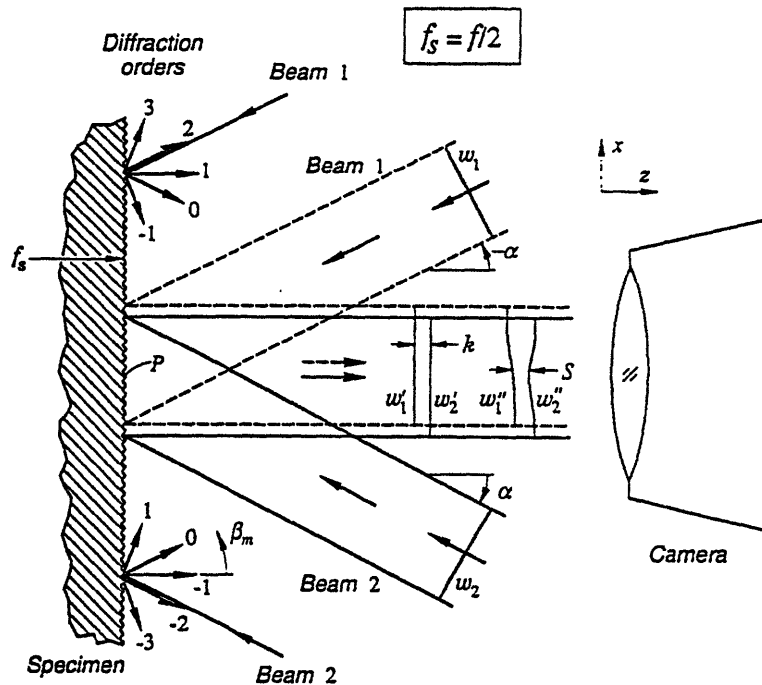


Figure 3.10-Null field condition for the reference grating specimen.

In order to calibrate the PEMI the reference grating is placed in the sample bed and slid the proper distance along the track so that the four beams emerging from the PEMI are all intersecting in the plane of the reflective grating surface. In order to insure that all four beams are incident at equivalent angles to the grating a feature has been built into the PEMI which aids in this alignment. In addition to the primary diffraction order emerging normal to the specimen from all four beams, there also orders which provide direct reflection. The exact mechanism by which they operate is described in detail in Chapter 2, but essentially they are reflected to a white plate within the PEMI. When all four of these reflection orders are centered in the hole in the center of the plate all four beams have an equiangular relationship with the sample.

In addition to this requirement we also want to minimize the total number of fringes emerging from the sample. When the mirrors direction the four incident beams are both symmetric in their angle of incidence and that angle satisfies the diffraction relation for normal diffraction the null field is aligned. Usually a minimum of one fringe across the field of view is realizable. Now a sample taken from the same reference grating can be analyzed to measure the total strain accumulated in the specimen from the grating replication temperature to the temperature of the analysis.

3.4.2 Sample Alignment and Analysis

In loading and aligning a sample, most of the same concepts apply as with the reference grating null field alignment. The sample is fixed to the sample stage and slide so that the diffraction grating on the cross-section is in the plane in which all four beams intersect. Then using the sample stage (not the PEMI mirrors as in null field alignment) the sample is aligned so that the incident beam equiangular relationship is satisfied. There is also an adjustment which controls motion about the z-axis in the sample. When the vertical family of grating lines are oriented perpendicular to the plane shared by the two horizontal beams which interact with it, the dots will be centered in the hole. The same is true for the horizontal grating lines and the vertically incident beams. Since we don't necessarily expect to have the sample grating to have the sample frequency as the reference, we relax the requirement that we minimize fringes. In fact the fringes observed are the strain information for the package.

As discussed in Chapter 2, since we are simply measuring displacement we must define a strain neutral point in order to obtain strain. This is done by several techniques: (1) If the package is mechanically symmetric we can simply center the fringe pattern about the center of the package (or neutral point). (2) If only normal strains are present in a given region then they can be aligned vertically for U-field and vertically for V-field. (3) If no exclusively normal strains are present then with the whole sample in view the total number of fringes present should be minimized. This corresponds to minimized carrier. Once one of these techniques is used to center the carrier and assuming that the two families of grating lines are perfectly orthogonal, both u-Field and v-Field can be viewed without making any further adjustments. Sample u and v field images with properly centered (minimized) carrier are shown below in Figure 3.11.

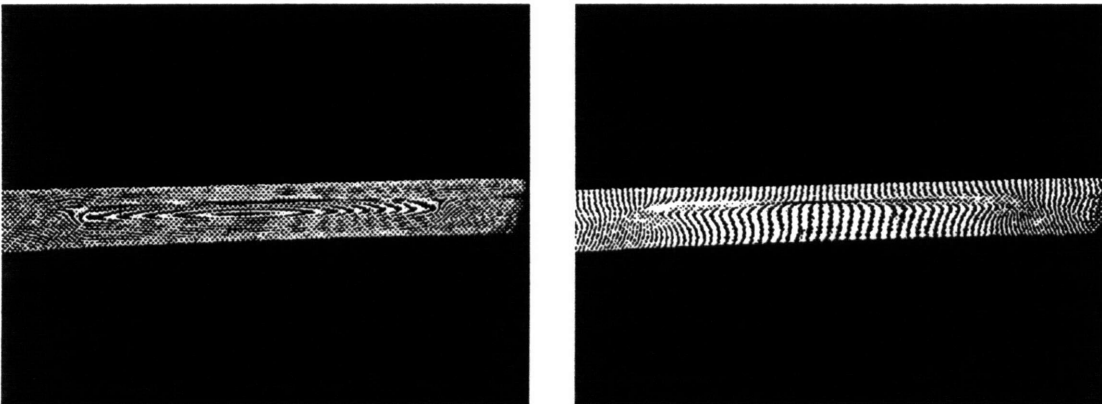


Figure 3.11 (left) v-field of PPGA at room temperature. (right) u-field of PPGA at room temperature.

Chapter 4

Validation of PEMI and Moiré Technique

4.1 Introduction

In order to insure that the fringe pattern observed by the CCD camera as output from the PEMI is truly representative of the deformation of a sample, a control specimen subjected to known strain was analyzed. The analysis for the U-field and V-field was done separately for the bulk 6061 aluminum control specimens. The same specimens were then analyzed using Thermo Mechanical Analysis (TMA) and an automated technique using CAFRAN described in Chapter 2.

4.2 Results

Five samples were selected for the validation experiment in which the results from TMA and Moiré for the same samples and the same axes within the samples were compared. A larger sample set of aluminum specimens was analyzed for both u-field (x-directional) and v-field (y-directional) strains and a subset of that was tested using TMA. In all cases the grating was applied to the aluminum specimens at 104 °C and the moiré fringe patterns were taken at 22 °C. For the TMA, which measures the vertical displacement of a stylus resting on the sample, the slope of the displacement versus temperature plot obtained between 30 and 100 °C was taken as the CTE measure. As described in Chapter 2 CAFRAN requires fringe patterns for two different temperatures for the phase difference method (PDM). Thus, patterns for 22 and 32 °C were used. The temperature measure for CAFRAN analysis was taken from a thermocouple directly attached to the specimen with 0.1 °C resolution. The results of the validation experiments are given below in Table 4.1.

<u>Method</u>	<u>High Value</u>	<u>Low Value</u>	<u>Mean Value</u>	<u>Median Value</u>	<u>Standard Deviation</u>
Moiré U-Field CTE	23.56	21.46	22.58	22.49	0.518
Moiré V-Field CTE	23.63	21.67	22.83	22.56	0.755
TMA X-Directional CTE	23.63	20.63	22.19	22.23	1.063
TMA Y-Directional CTE	22.02	21.24	21.58	21.53	0.369
CAFRAN U-Field CTE	19.3	25.2	22.3		
CAFRAN V-Field CTE			22.1		

Table 4.1-All figures reported in ppm/°C.

A scatter plot of the measured values for each sample using the different measurement techniques is also given in Figure 4.1 below.

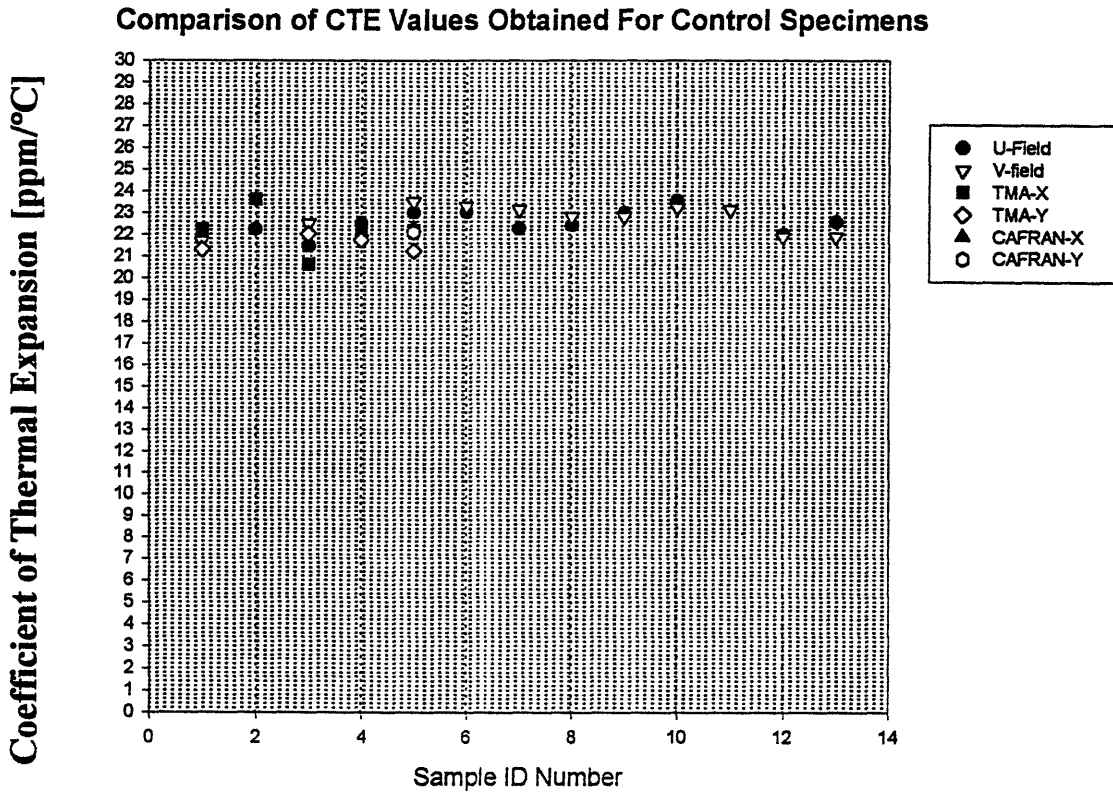


Figure 4.1-CTE data for 6061 bulk aluminum for various directions and techniques of measurement.

The data demonstrate a high correlation between the TMA and moiré results and the strain map obtained from CAFRAN. The strain map generated for the aluminum sample is presented in the section on computational analysis (Chapter 7). This controlled experiment validates the moiré process by comparing it to another well known thermal strain measurement tools. Furthermore, since the sample had a known CTE (~22 ppm) all the values could be assessed with respect to any bias in the measurement technique. The results also serve as validation of the grating replication and manual analysis scheme.

Chapter 5

Die Bonded to Substrate: Ceramic versus Organic

5.1 Introduction

This section summarizes the moiré analysis of silicon epoxy-bonded to organic and ceramic substrates to assess the magnitude of shear strain in the bond layer as well as the die warpage. First a discussion of special sample preparation procedures is given. A comparison of both shear strain in the thin epoxy bond line and warpage of the die is presented. The thermal chamber used to control the sample temperature allowed the observation of temperature dependent strain profiles to insure that the strain behavior followed the expected pattern as the grating replication temperature was approached. Finally, data collected using a laser line profilometer called flexus from the same samples will be used to validate the moiré warpage observations. A comparison between the state of strain in ceramic versus organic based substrate systems is drawn by empirical measurements of the shear strain and warpage in the packages.

Essentially the structure consists of a silicon die which is mechanically coupled at a temperature of ~ 180 °C to either an organic or ceramic substrate by an epoxy bond layer. The package will experience warpage in the manner shown in Figure 1 similar to a bimetallic strip. The coefficient of thermal expansion (CTE) of silicon is ~ 2.6 ppm/°C while the CTEs for the organic substrate and Alumina (ceramic) are 17.4 ppm/°C and 7 ppm/°C. Thus, upon cooling from 180 °C the substrate will contract between 2 and 7 times faster, than the die. The rate at which the die is compressed and package warpage accumulates is directly proportional to the CTE mismatch. Since the operating temperature and room temperature are both lower than the joining temperature, the substrate will always be acting to compress the die at the bond layer interface. The results will also reflect a geometric distinction between the two sample types, namely that the ceramic substrate was 0.020" thicker than the organic substrate.

Another mechanism by which the CTE mismatch strain can be accommodated within the specimen is by shear of the epoxy bond layer. Thus, a portion of the mismatch strain is accommodated through bond layer shear and the remaining strain is responsible for the elastic compression of the die and monolithic package warpage. The relative magnitudes of the three mismatch strain mechanisms is determined by the relative stiffness, thickness and Poisson's ratios of the three material layers. This study attempts to measure the warpage and bond layer shear strain magnitude between the two substrate

types. The results should be considered with keeping in mind that the thicknesses of the two substrates were not identical which could account for some of the relative differences in the two strain measures being tracked. Though it is not integral to the discussion, a model predicting the interfacial strain within the packages similar to Figure 5.1 as a function of the distance from neutral point has been solved by Suhir in *Thermal Stress and Strain in Microelectronics Packaging*⁴⁵. An understanding of the role of the various layer thicknesses could be obtained by experimenting with the model presented in this book.

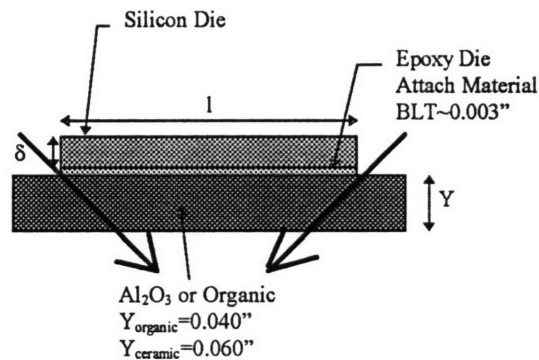


Figure 5.1-Die bonded to substrate samples exhibiting a concave down warpage at temperatures below 180 °C.

5.2 Die-Bonded Substrate Sample Preparation

The die bonded samples were constructed of a silicon die attached to either an organic or ceramic substrate using an epoxy adhesive. A diagram of the samples is shown below in Figure 5.2. Also given are the relative CTEs of the various materials present. The diamond impregnated wire saw was used to section all the samples after assessing the die warpage using laser profilometry. The substrates were fixed to the cutting board using double-sided adhesive tape with the die oriented up. The wire arc during cutting was minimized to reduce nonuniform loading of the compressed die. This technique appeared to produce a higher yield on non-cracked specimens. The organic packages exhibited as greater propensity to crack than their ceramic counterparts. The yield for the organic was ~50% while the ceramics was 100%. The difference in yields is due to the higher stress intensity in the organic versus ceramic system, differences in the flexing of the samples during the cutting process or a combination of the two.

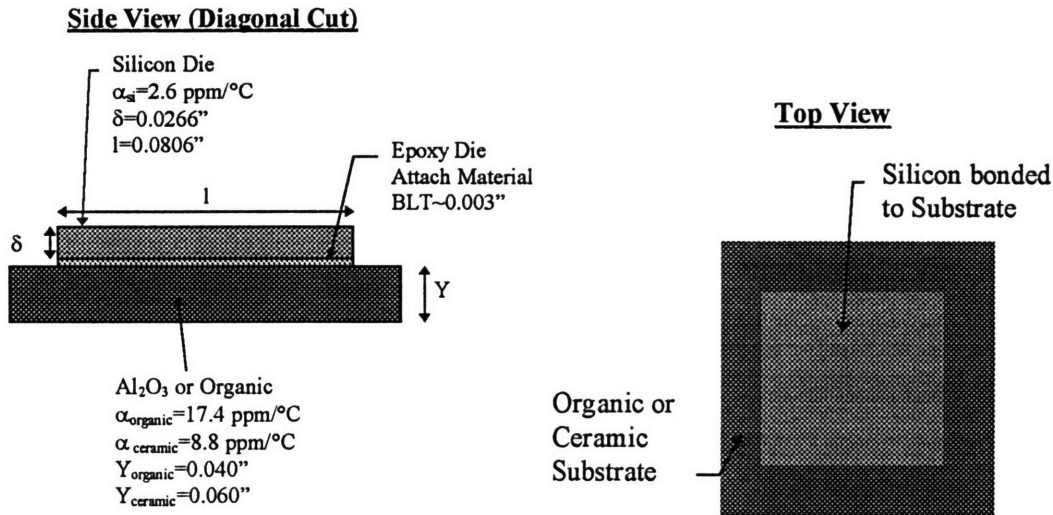


Figure 5.2-Die bonded to substrate structural diagram. (left) diagonal cross section, (right) top view with die facing up.

After the samples were cut they were measured using a Buechler Optical Microscope Scale to verify the dimensions of the samples. Then the grating was replicated on the grating bed at 104 °C in the manner prescribed in Chapter 3. After removal from the master grating the extraneous grating and epoxy was removed using a razor blade from the edges of the die and substrate to allow proper identification of the sample edges within the fringe pattern. The samples were then analyzed using the protocol outlined in the section 3.4.

5.2.1 Thermal Carrier Adjustment

By controlling the sample temperature within the environment chamber the accumulated strain from 104 °C to any temperature down to room temperature was observable. In cooling and heating the specimens it was noted that through the sample fixturing mechanism a temperature dependent rigid body rotation was introduced. The carrier or grating rotation induced mismatch in the fringe pattern changed as the clamps holding the sample in place expanded and contracted. Therefore, it became necessary to minimize the carrier at each new temperature before capturing the fringe pattern.

5.2.2 Manual Analysis Elements

The average corner shear strain calculations were made using the manual analysis technique outlined in Chapter 2 of this study. Essentially an element of known dimensions is defined in the corner (highest shear strain) die bond region. The number of fringes and partial fringes intersected by the perpendicular bisectors of the rectangular element define the average shear strain across the two bisector

lines, or more generally within the element. An element was defined in the epoxy bond line at the corner of the diagonally cut samples to analysis the average strain value. The region analyzed should exhibit the highest shear strain present in the package since its distance from neutral point (DNP) is greatest. Figure 5.3 below shows a sample U-Field fringe pattern and element defined with perpendicular bisectors for manual analysis. The manual analysis equations given in Chapter 2 were applied to the U and V-field fringe patterns for each temperature to obtain strain values from the fringe patterns.

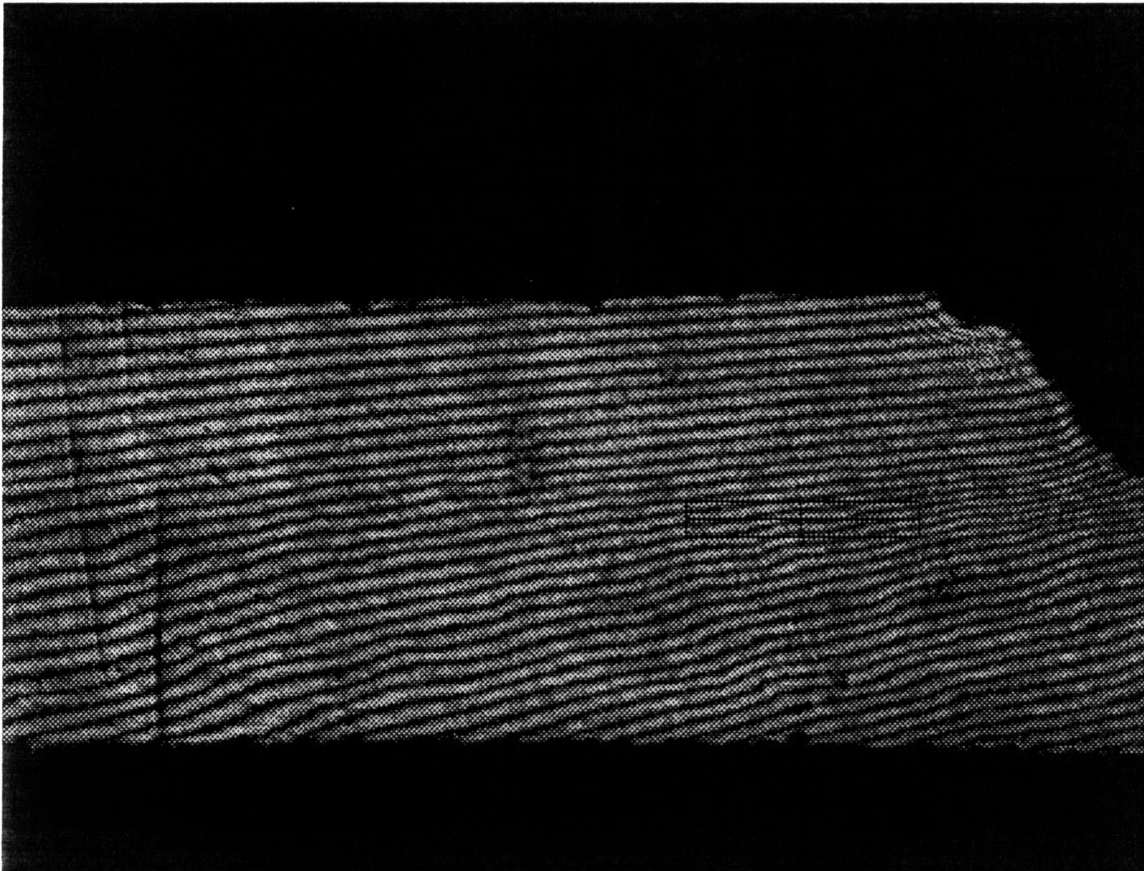


Figure-5.3-Example of element definition used to do manual strain analysis in die-bonded to organic and ceramic samples.

5.2.3 Moiré Warpage Measurement

The warpage of the top surface of the silicon die was analyzed as a function of the distance from neutral point (DNP) and temperature. The V-Field fringe patterns indicate the vertical displacement of the die at the point at which a fringe intersects the top surface of the die. Each intersected fringe represents an incremental vertical displacement of 417 nanometers (0.417 μm). With the carrier centered about the neutral point the DNP of each fringe was recorded to generate a set of vertical displacement (warpage) versus DNP curves for each temperature.

5.3 Shear Strain Analysis Results

Using the thermal chamber the die bonded to substrate samples were analyzed at 5 °C increments from 40 °C to 100 °C and at room temperature (23 °C). It was then possible to calculate the average shear strain magnitude in the die corner bond layer element illustrated in section 5.2. Because of time constraints on the projects two samples of each type of substrate were analyzed. A profile of the strain magnitudes for the same corner bond layer section on each specimen was collected for both substrate types as a function of temperature. The room temperature strain magnitudes in the opposite corner of the die bond layer were also calculated to verify that the values were identical at the highest loading condition (23°C). The results of the strain measurements are given below in Table 5.1. The ceramic epoxy bond layer exhibited room temperature accumulated strain magnitudes of 0.21 to 0.27% while the organic substrate induced values ranged from 1.44 to 1.64%. The actual strain values as a function of temperature are given below in Table 5.1.

<u>Temp °C</u>	<u>Ceramic #1 (side 1)</u>	<u>Ceramic #2 (side 1)</u>	<u>Organic #1 (side 1)</u>	<u>Organic #2 (side 1)</u>	<u>Ceramic #1 (side 2)</u>	<u>Ceramic #2 (side 2)</u>	<u>Organic #1 (side 2)</u>	<u>Organic #2 (side 2)</u>
23	0.22	0.27	1.63	1.44	0.27	0.21	1.48	1.64
25	0.16		1.54	1.32				
40	0.17	0.15	1.46	1.13				
50	0.11	0.13	1.26	0.93				
60	0.13	0.11	1.07	0.78				
70	0.05	0.09	0.92	0.64				
80	0.05		0.71	0.34				
85		0.08						
90		0.05	0.38	0.1				
100		0	0.18					

Table 5.1-The accumulated strain magnitudes in die corner epoxy bond regions defined in Figure 5.3.

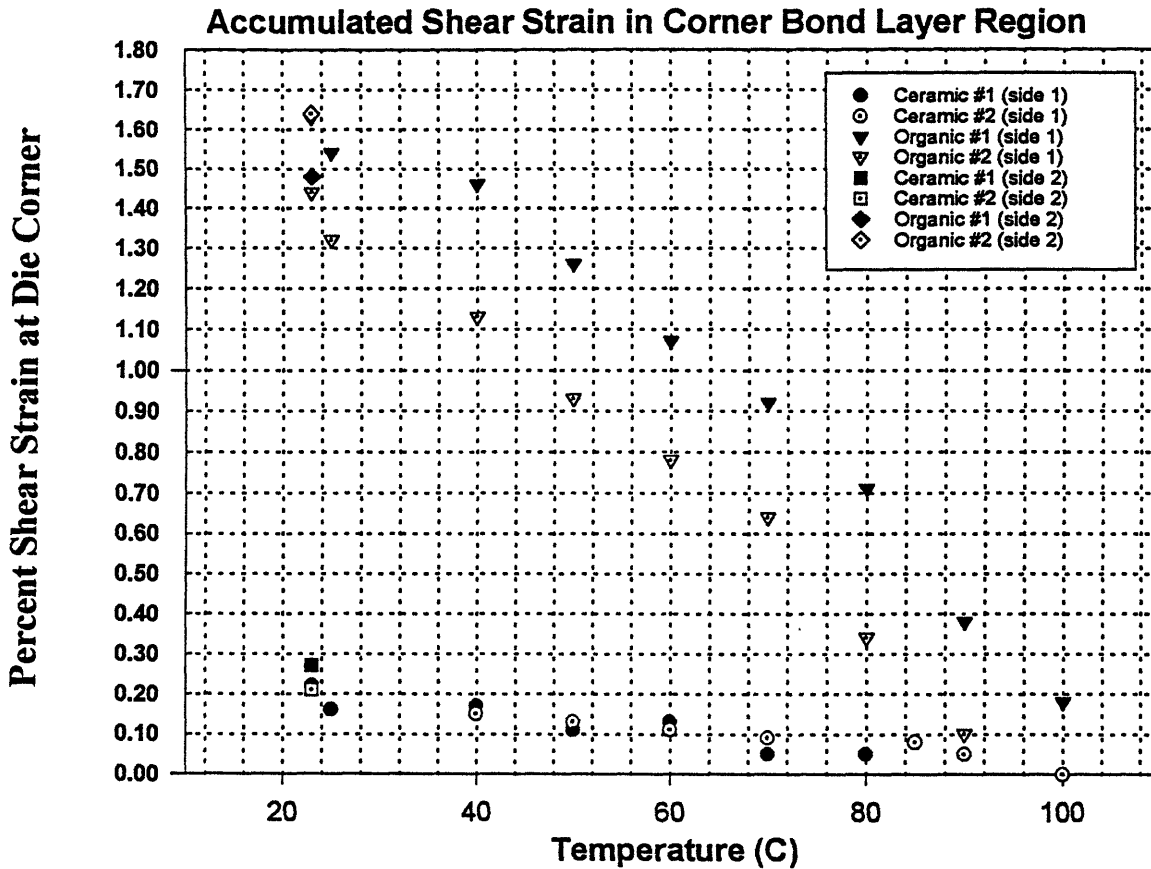


Figure 5.4-Shear strain profile of region defined in Figure 5.3 for all four samples analyzed in the study. The room temperature strain magnitude for the opposite corner is also represented.

5.4 Die Warpage Results

The warpage of the two sets of samples analyzed was characterized by two independent methods, flexus and Moiré. Since the first is a non-destructive technique it was possible to conduct the measurement on the samples and then cross-section them for moiré. It should be noted that the cross-sectioning results in a slight increase in the warpage due to the removal of on half of the package. By comparison of moiré data with flexus data the amount of warpage induced by the cross-sectioning of the organic package was on the order of 9.1 μm . The ceramic package exhibited a change that was not within the resolution of the flexus measurement.

The two samples of each substrate type were analyzed in halves, that is the left and right side warpage analyses were conducted separately and then the two data sets were combined. This procedure,

dictated by the CCD camera resolution limits, allows small amounts of carrier mismatch to exist between the two fringe pattern sets if the center of the sample is not identified exactly and the carrier is centered about a slightly off-center point. This carrier error, though not as important in die bonded substrate samples, will be addressed again in Chapter 6 where its role is more significant. It should be noted that any difference between the vertical displacement values on either end of the sample is a result of this type of error. In the die bonded substrate samples this error was small due to refined center-point definition techniques. The warpage plots obtained for two of the four samples are given below in Figures 5.5 and 5.6. The fringe patterns for both samples are shown in at the end of this chapter.

Ceramic #1 Die Warpage Profile

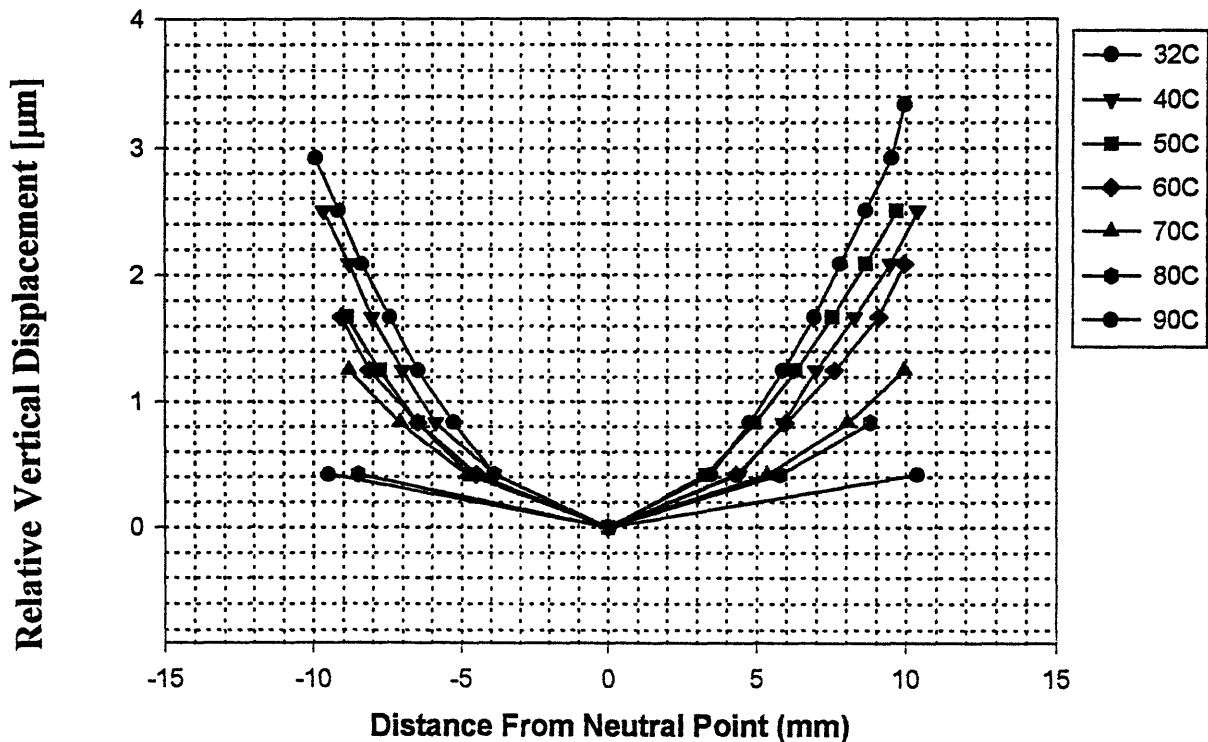


Figure 5.5-Die warpage temperature curves for die bonded to ceramic packages.

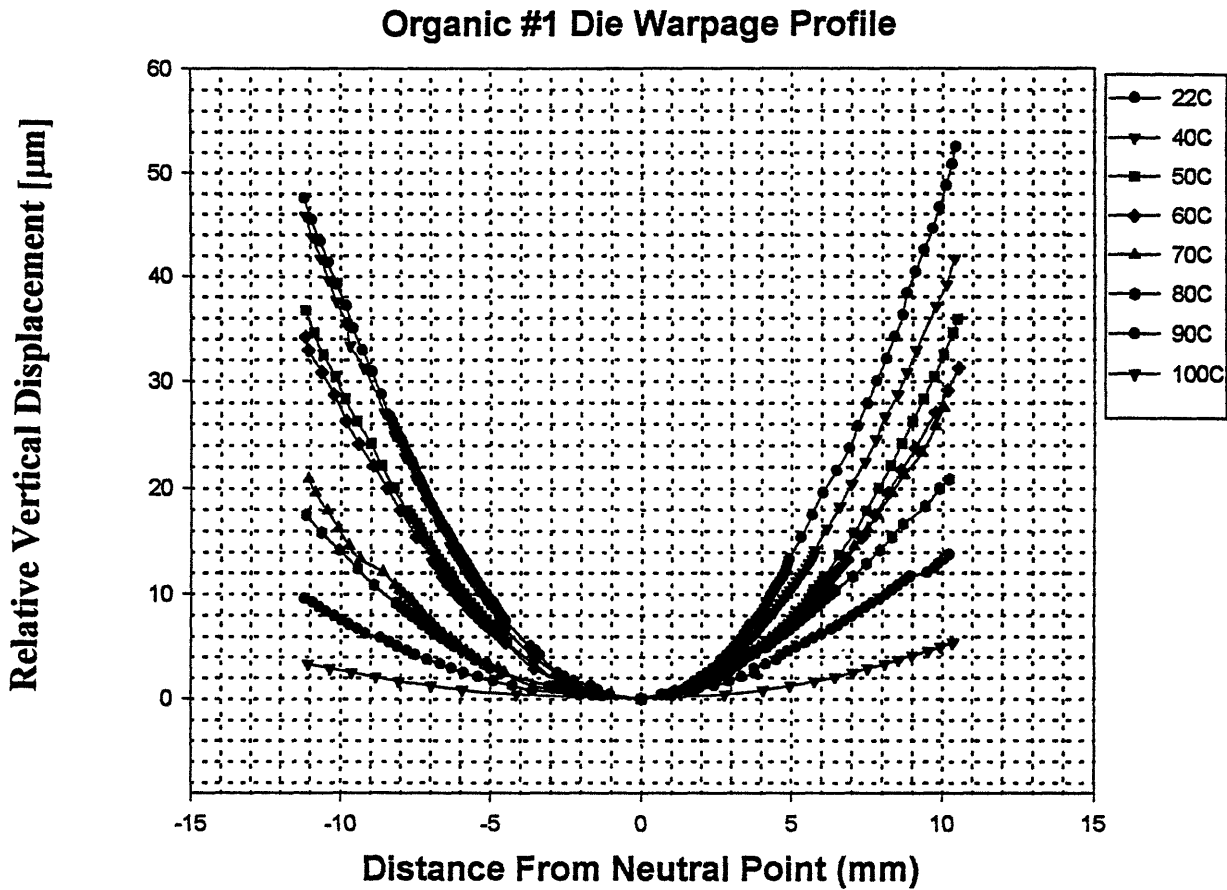


Figure 5.6-Die warpage temperature curves for die bonded to organic packages.

The moiré warpage profiles shown above were nearly identical in both samples of the same substrate type indicating that the technique is consistent in the magnitude of vertical displacements. The values of warpage obtained by flexus and Moiré at room temperature (23°C) are shown below in Table 5.2.

<u>Sample</u>	<u>flexus Warpage (µm)</u>	<u>Moiré Warpage(µm)</u>
Ceramic #1	3.7	3.6
Ceramic #2	7	3.2
Average	5.35	3.4
Organic #1	45	49.7
Organic #2	36.5	50
Average	40.75	49.85

Table 5.2-Vertical displacement values obtained by moiré and flexus.

The values for the ceramic appear not to be significantly affected by the cross-sectioning of the sample whereas the organic exhibited a detectable difference between the sample before and after sectioning. The flexus measurement obscures the difference between the two because the lower resolution it possesses. The difference in warpage using the average values for cut versus uncut samples is 1.95 (μm) and 9.1 (μm) for the ceramic and organic samples respectively. A much larger sample set must be analyzed to assess the difference in warpage before and after sectioning accurately. The average values were 3.4 and 49.85 (μm) for vertical displacement for ceramic and organic packages

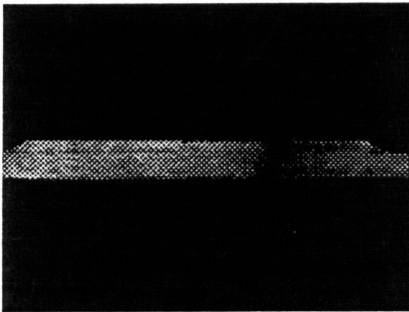
5.5 Conclusions

General industry trends toward more economical resin based substrates and away from higher cost and thermomechanically superior alumina substrates have heightened the interest in the fatigue failures in direct chip attach assemblies. As more cost effective organic substrates are implemented the CTE mismatch increases causing a commensurate increase in stress intensities. This study empirically found the substrate economic value of the less expensive organic substrate is offset by an equally important fatigue failure concern driven by a heightened stress intensity factor. Thus, for electrically equivalent packages of ceramic and organic substrates, the potential for failure due to fatigue in the organic will be much greater than in the ceramic. The magnitude of the difference in fatigue life between the two can be predicted by supplying moiré strain information to computational fatigue models.

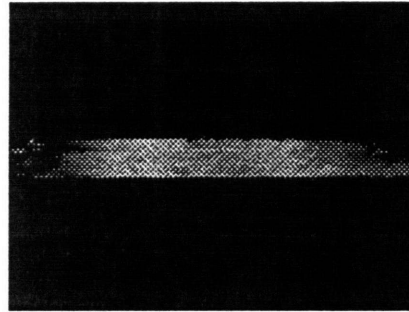
Average shear strains in the corner regions of the epoxy bond layer for organic samples to be ~ 6.14 times higher than for their ceramic counterparts. Intrinsic to the measurements was the destabilizing effect of cross-sectioning and removing half of the package and the 0.020" difference in substrate thickness. Although both sample sets were cross-sectioned in the same manner the amount of strain induced by the cross-section step is expected to be greater for the higher strained, thinner, more pliable organic substrate. As an indirect measure of the amount of strain introduced into the systems by sectioning along the diagonal, flexus data (before sectioning) was compared to moiré warpage data. With the small sample size obtained the approximate increase in warpage of organic samples was ~ 9 μm which is an increase of $\sim 22\%$. The same comparison of samples before and after sectioning for the ceramic yields a decrease of ~ 2 μm which is a decrease of $\sim 36\%$. The trend in the ceramic structures of course are dominated by the resolution limits of both moiré and flexus. For larger sample sets numbers representative of the true change in warpage would allow one to assess the effect of the package

separation on the observed strain values. These values whether they be manually or computationally obtain can then be used to validate mechanical models after adjusting with a correction factor. In turn these models will assist engineers in assessing the trade-offs between immediate substrate costs in production versus long term package failure costs through shortened fatigue lives.

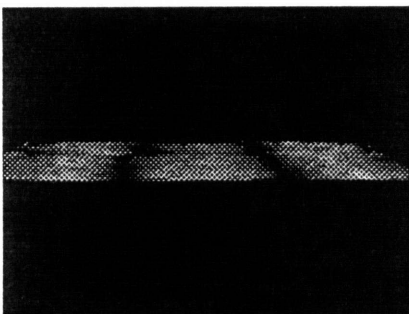
Die Bonded to Ceramic V-field Fringe Patterns



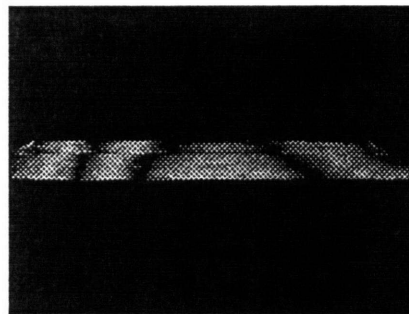
104 °C



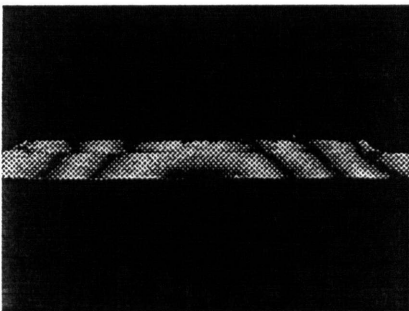
100 °C



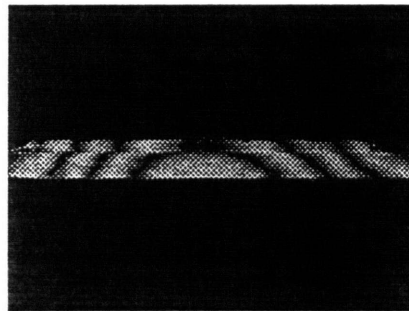
95 °C



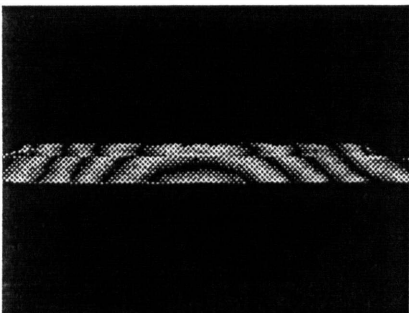
90 °C



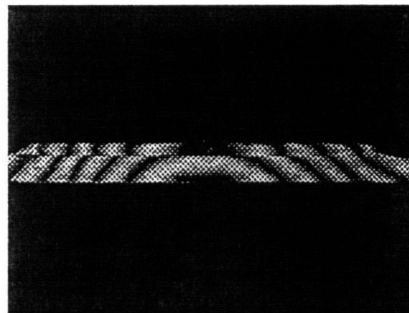
85 °C



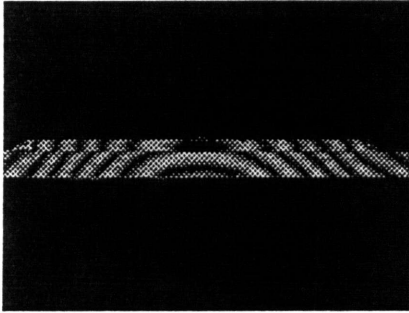
80 °C



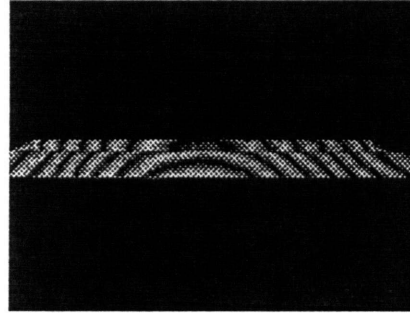
75 °C



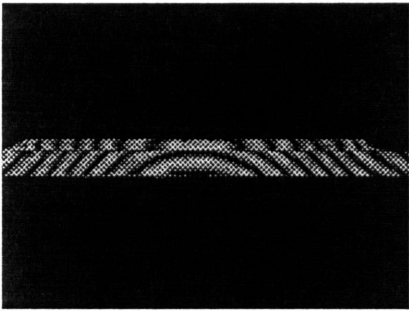
70 °C



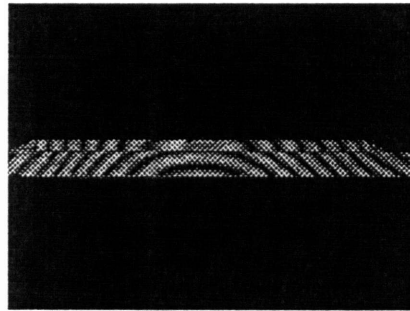
60 °C



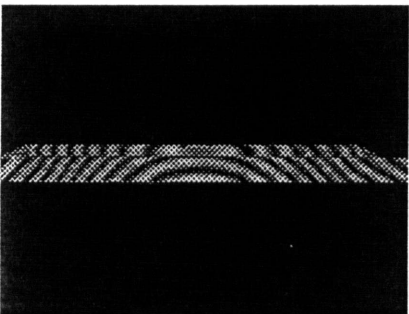
55 °C



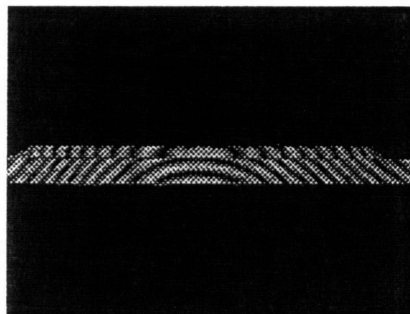
50 °C



45 °C



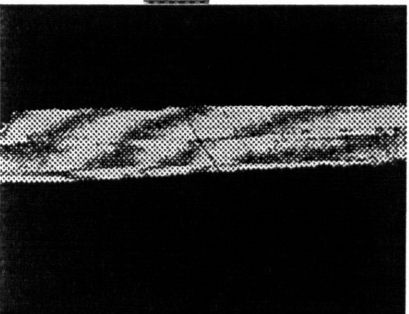
40 °C



30 °C

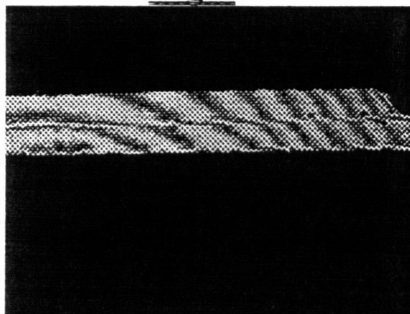
Die Bonded to Organic V-field Fringe Patterns

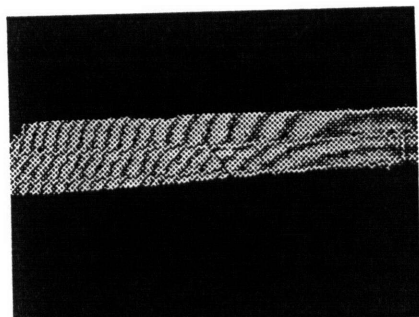
Left



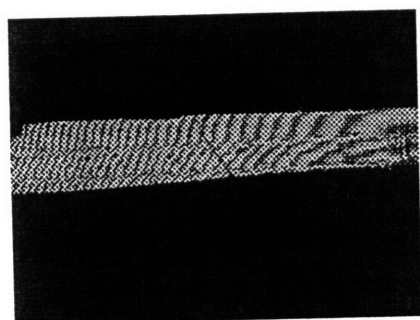
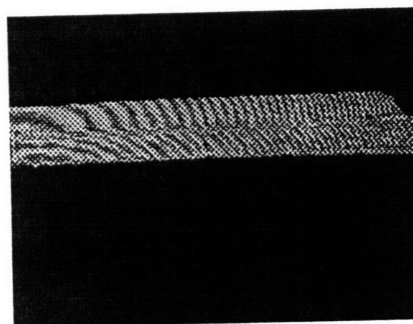
104 °C

Right

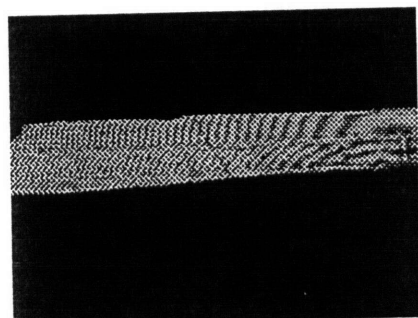
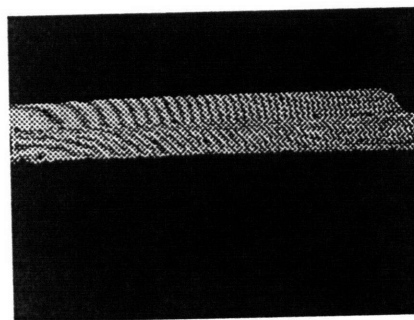




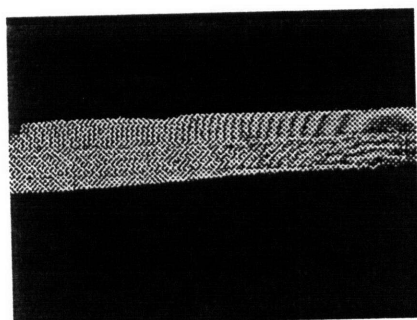
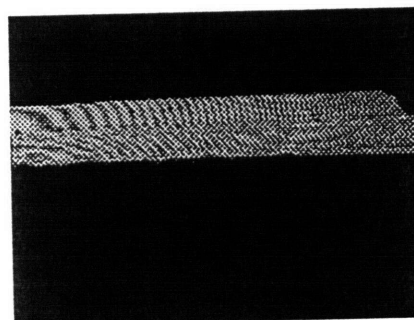
90 °C



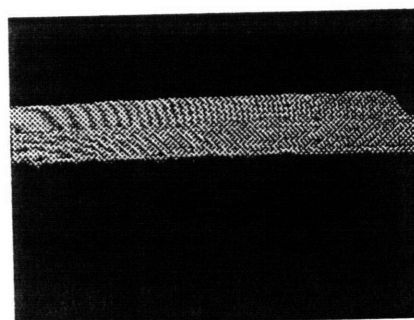
85 °C

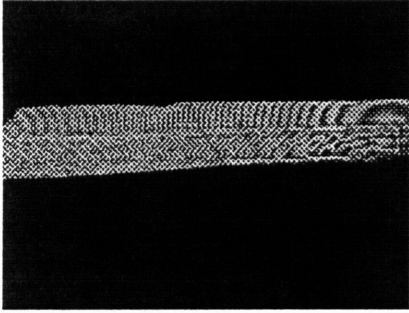


80 °C

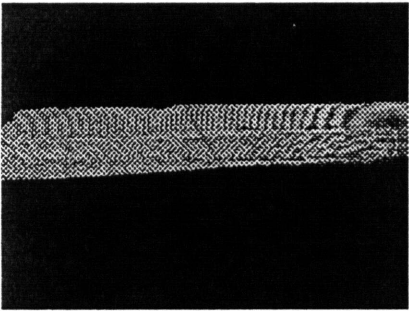
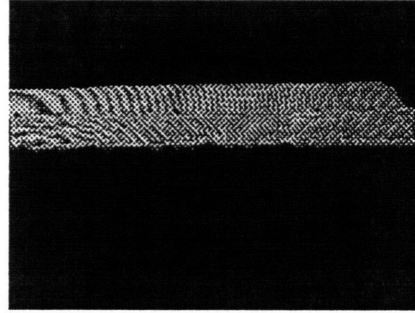


75 °C

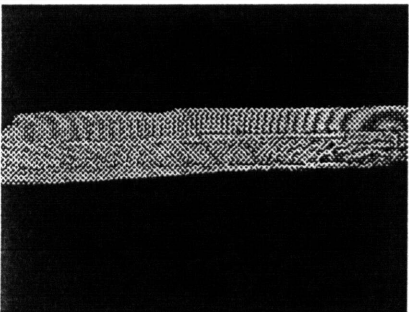
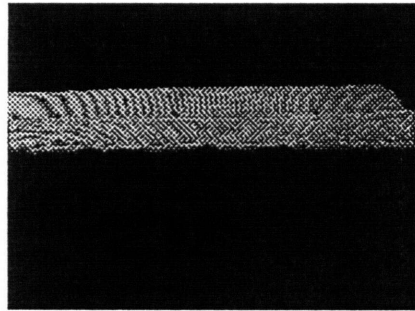




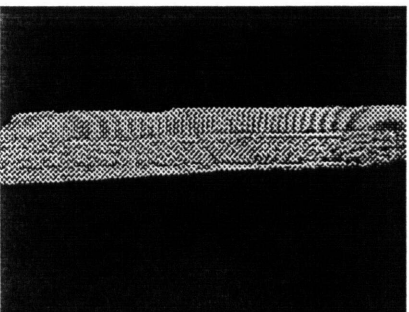
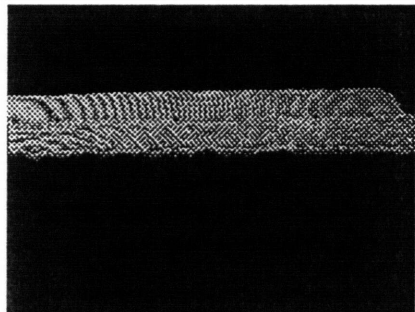
70 °C



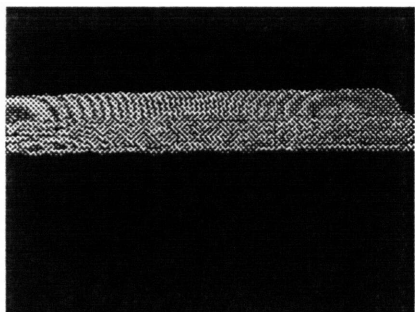
65 °C

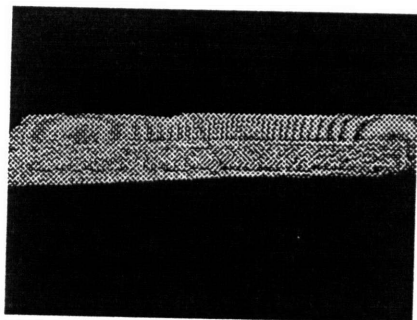


60 °C

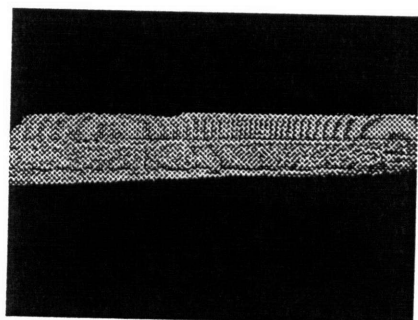
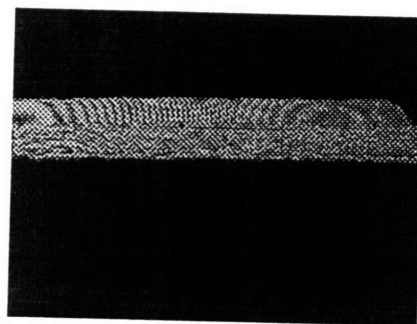


55 °C

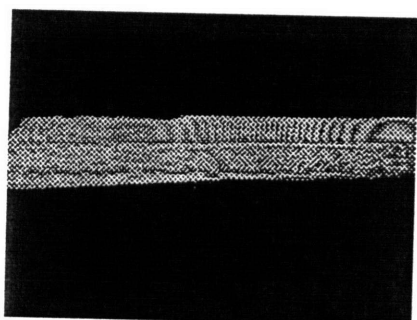
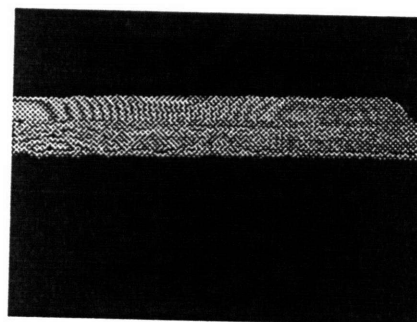




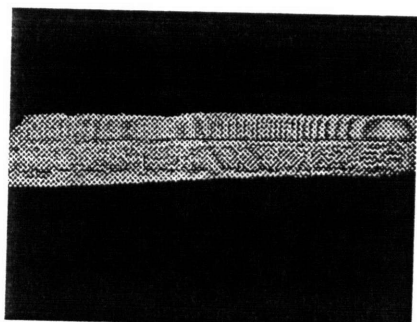
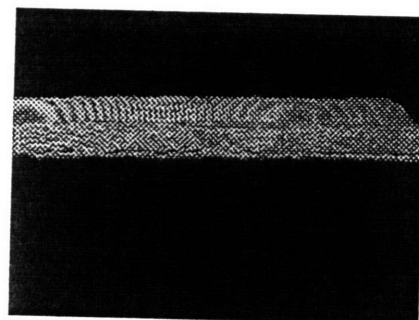
50 °C



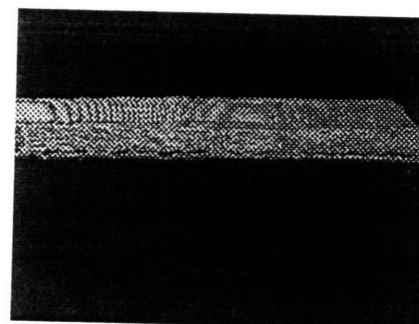
45 °C



40 °C

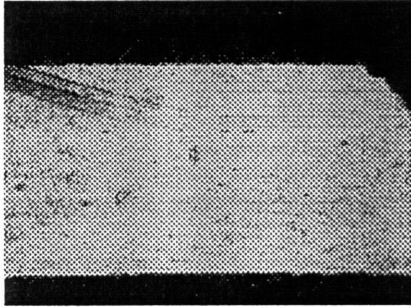


23 °C



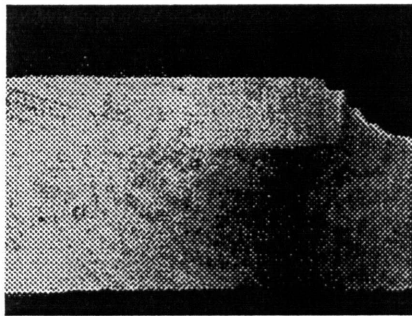
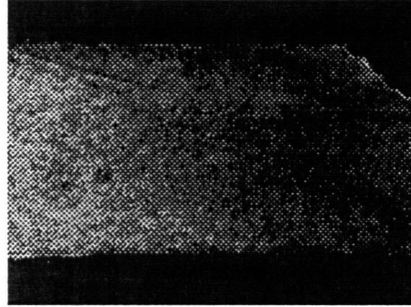
Die Bonded to Ceramic-Bond Layer Shear

U-Field

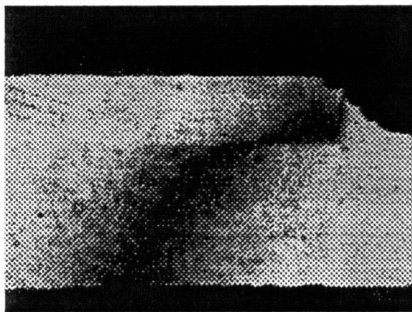
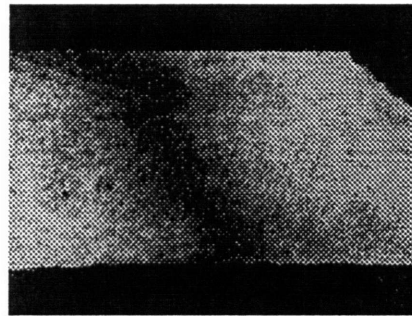


104 °C

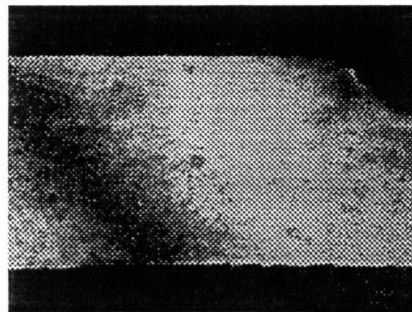
V-Field

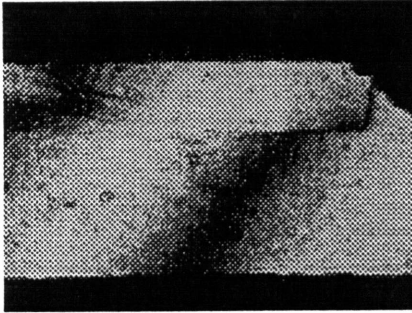


100 °C

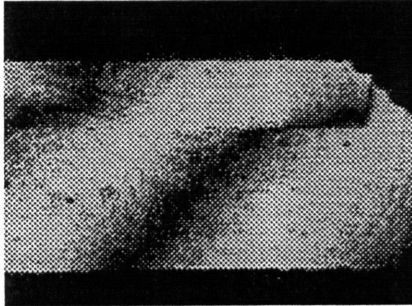


95 °C

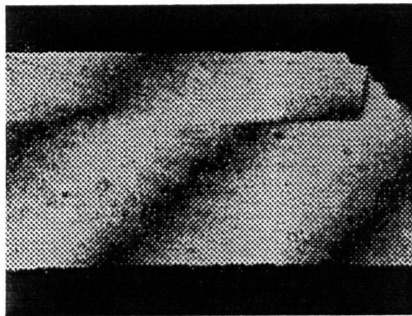




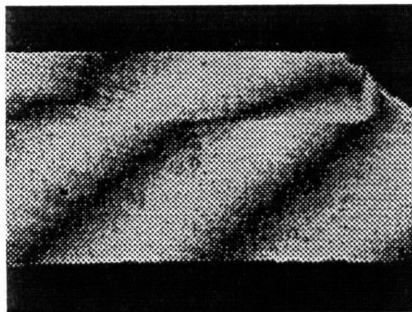
90 °C



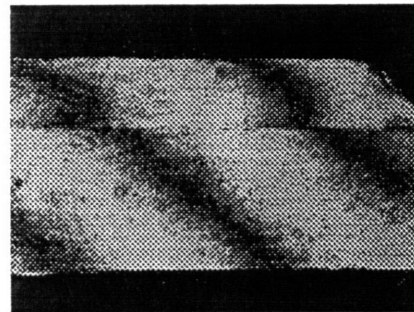
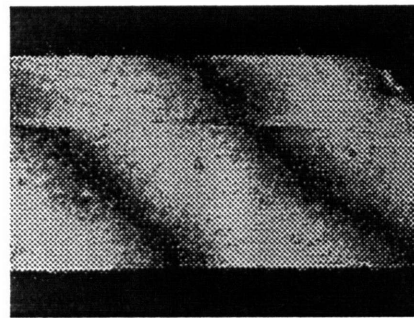
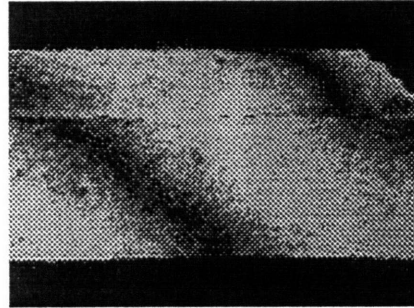
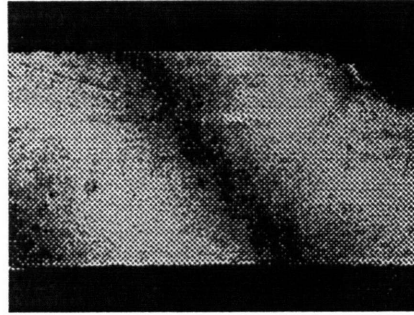
85 °C

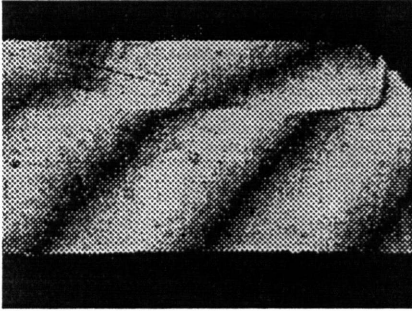


80 °C

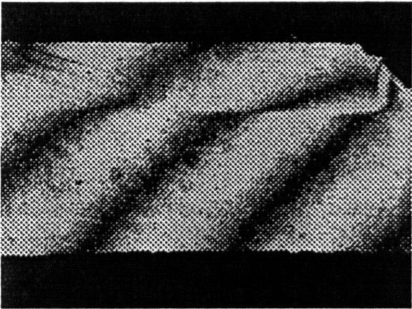
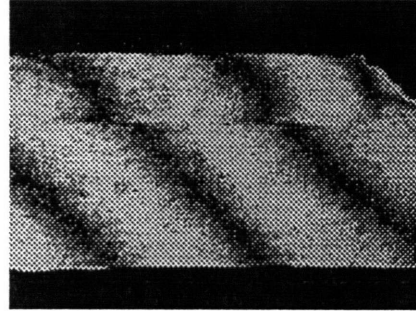


75 °C

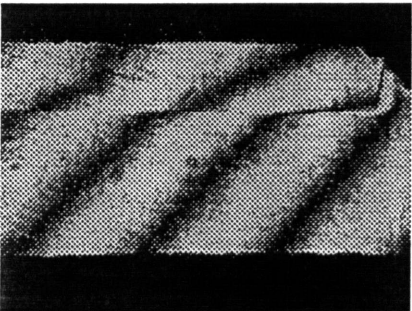
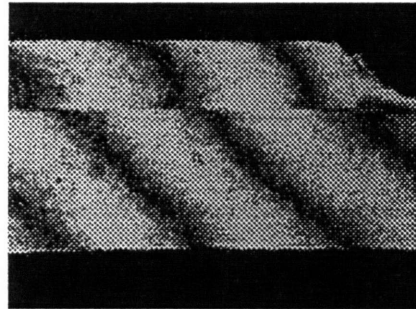




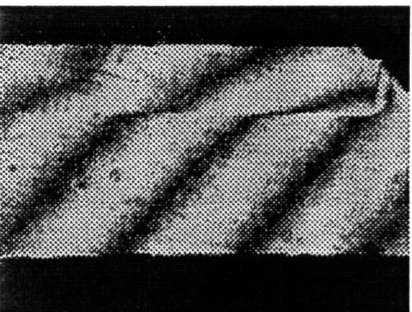
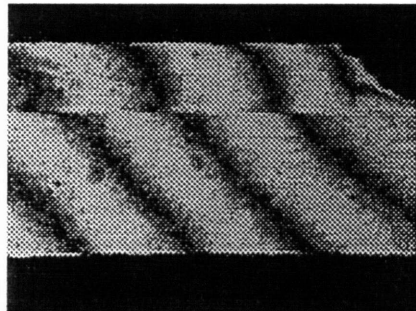
70 °C



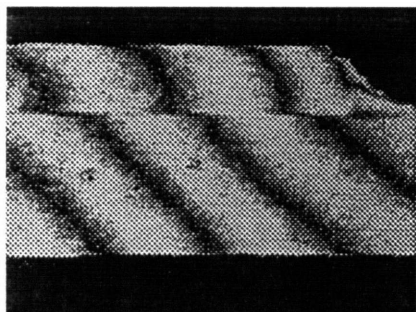
65 °C

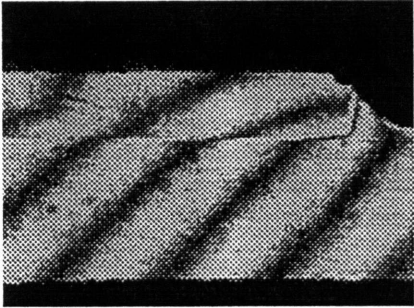


60 °C

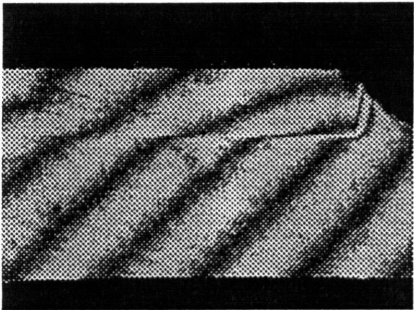
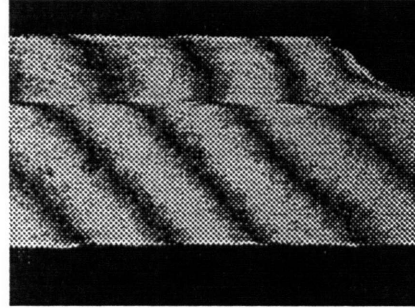


55 °C

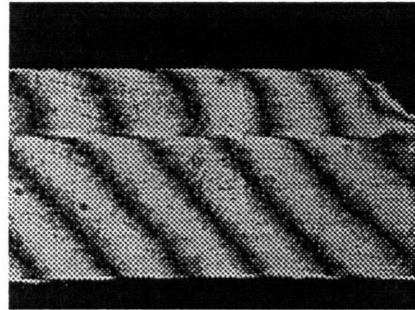




50 °C



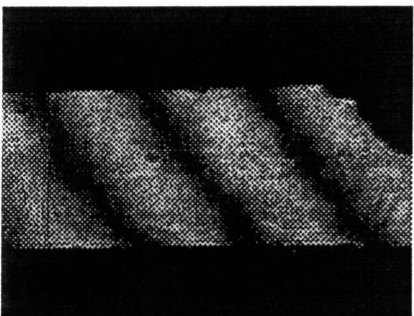
40 °C



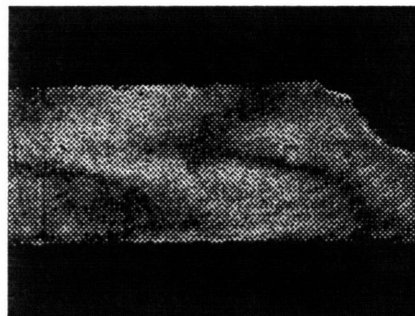
Die Bonded to Organic-Bond Layer Shear

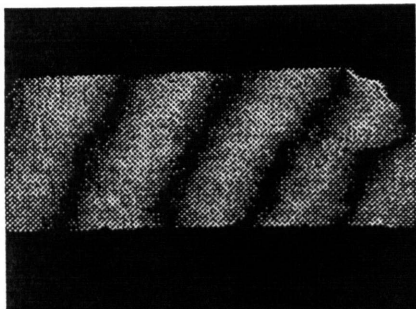
U-Field

V-Field

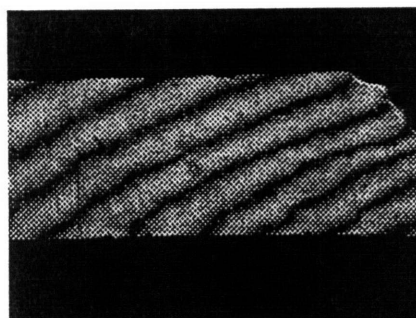
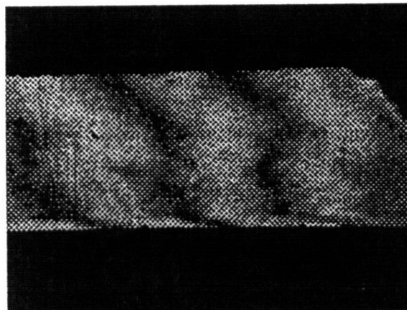


104 °C

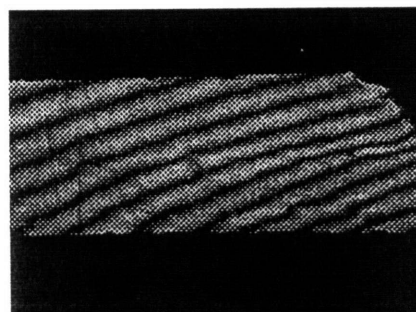
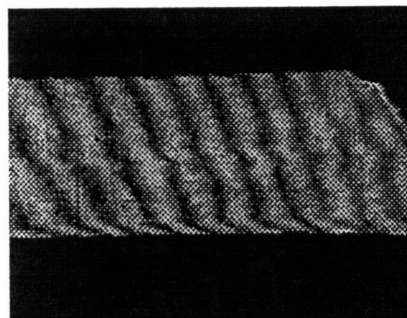




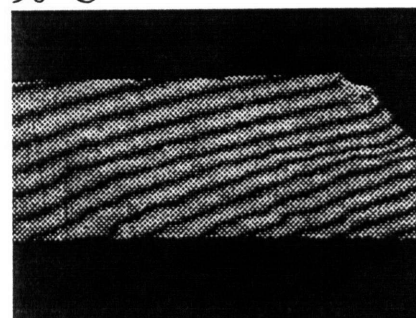
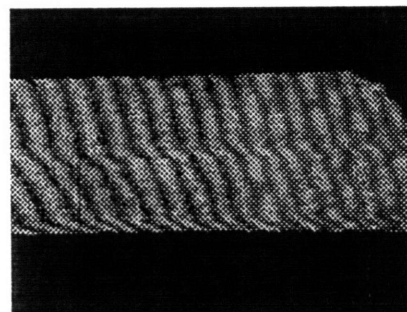
100 °C



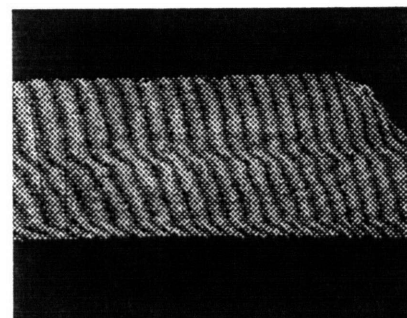
95 °C

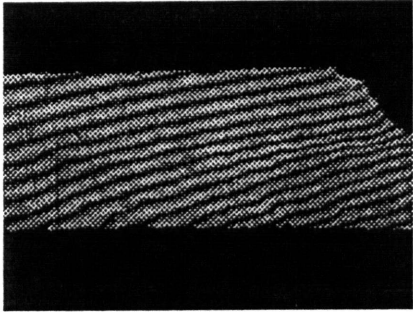


90 °C

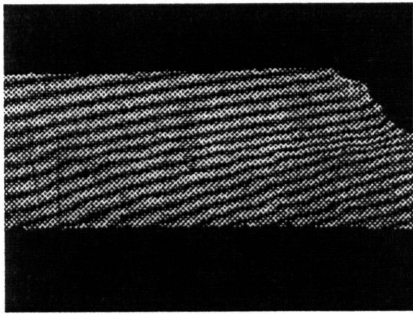
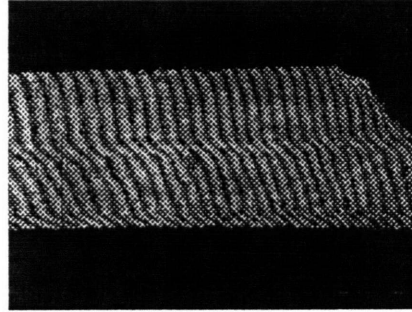


85 °C

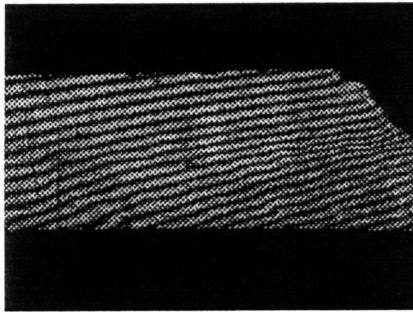
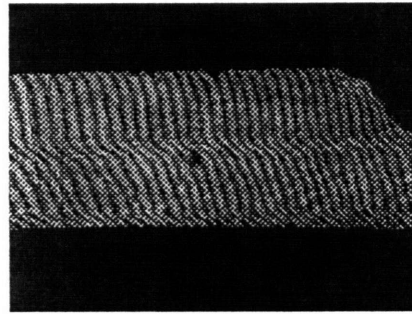




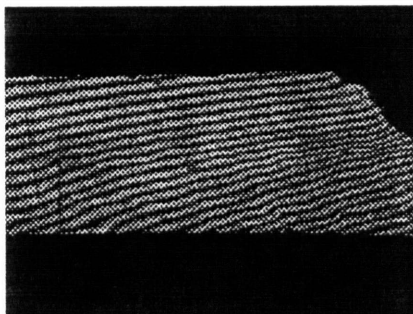
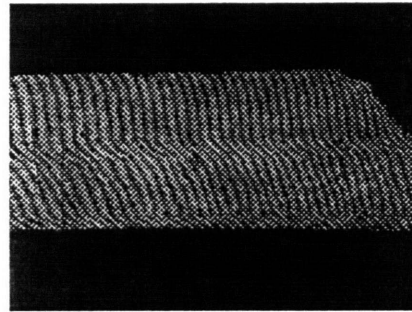
80 °C



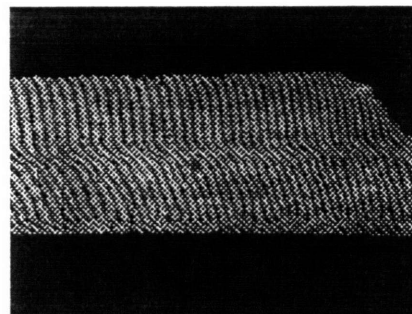
75 °C

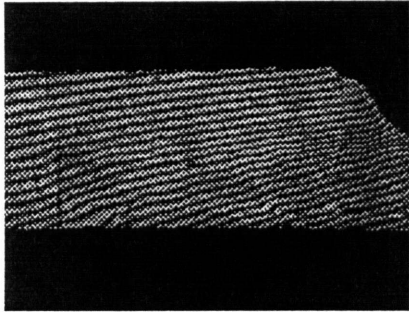


70 °C

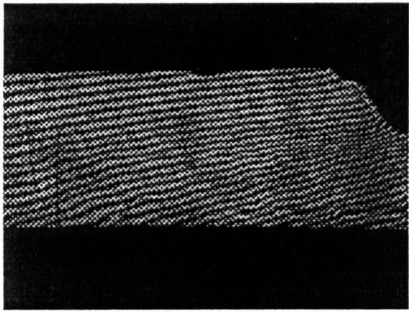
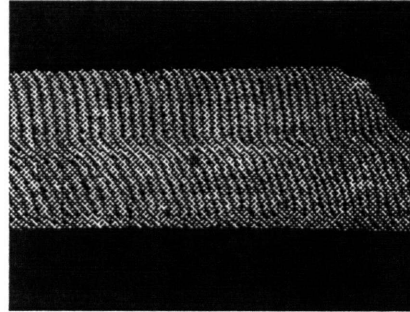


65 °C

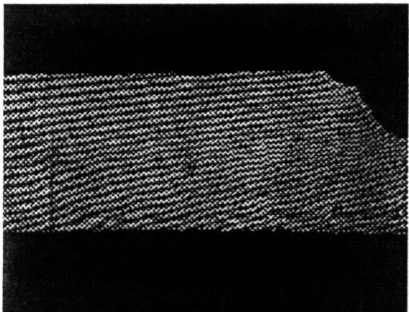
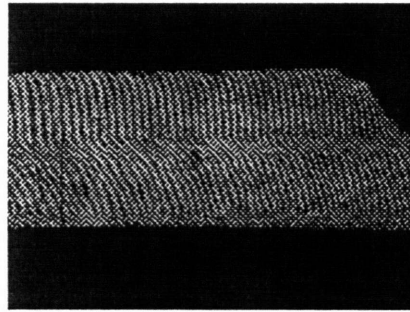




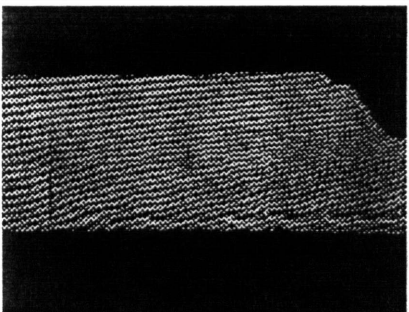
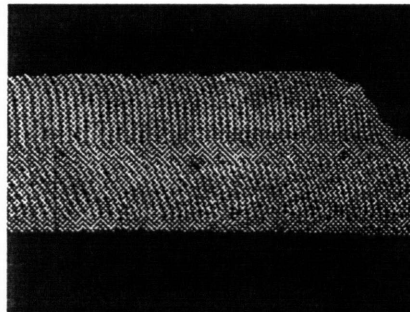
60 °C



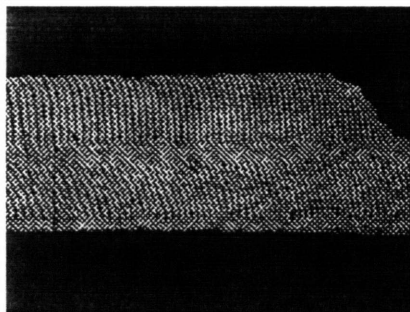
55 °C

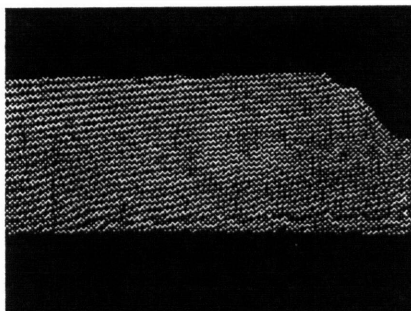


50 °C

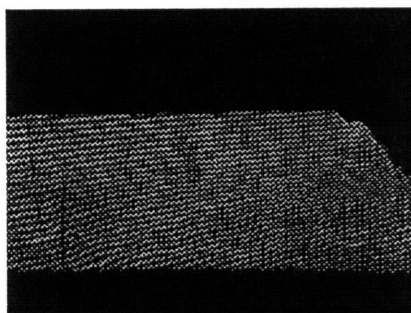
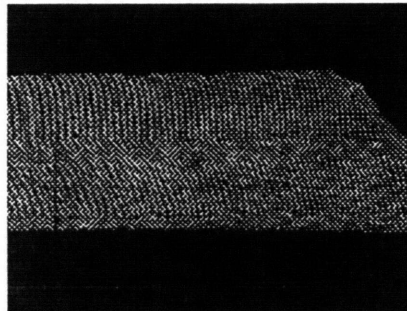


45 °C

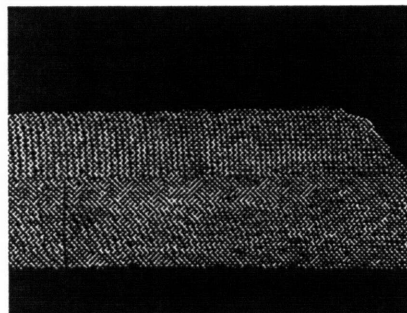




40 °C



23 °C



Chapter 6

Encapsulated Versus Non-encapsulated PPGA

6.1 Introduction

The plastic pin grid array (PPGA) is a cheap and efficient means of integrating microprocessors to boards. The PPGA is more complicated than the DCA assembly simulated in the previous chapter since it involved attaching silicon to a copper slug which is markedly stiffer than the organic substrate, yet imposes nearly as high a CTE mismatch. Thus, the thermomechanical strain mismatch will be compensated by three mechanisms: (1) through the elastic and viscoelastic shear in the thin die attachment (DA) epoxy layer, (2) by silicon die compression, or (3) by monolithic package warpage. The copper and die are joined mechanically at higher temperatures resulting in die compression throughout the operation of the device. A common practice is to encapsulate the side not bonded to the copper substrate with a plastic encapsulant. These typically force the die into compression and diminishes plastic strain accommodation in the DA layer which in turn enhances the fatigue life of the die-copper interface. To evaluate the effectiveness of encapsulants in decreasing shear stresses in the DA layer, manual analysis of the corner DA region encapsulated and non-encapsulated packages was conducted. Analysis of the warpage of the copper slug and die was completed for both sample types. Using flexus data for packages with the same encapsulant the moiré warpage data was validated.

The objective was to evaluate the effect of the presence of the encapsulant on the stress state of the package as a function of temperature. The encapsulated sample strain behavior was made more complex by the relatively low glass transition temperature of the plastic encapsulant ($T_g \sim 91^\circ\text{C}$). Accompanying the glass transition temperature is a significant change in the CTE and elastic and viscoelastic behavior of the encapsulant. Since the die is attached to the copper substrate at a temperature of around 150°C the system begins accumulating mismatch strain at that temperature. Upon cooling the copper (CTE $\sim 16.5 \text{ ppm}/^\circ\text{C}$) contracts ~ 6.3 times more per $^\circ\text{C}$ than the silicon die (CTE $\sim 2.6 \text{ ppm}/^\circ\text{C}$). The organic circuit board has a CTE of $\sim 13 \text{ ppm}/^\circ\text{C}$ which is ~ 5 times that of silicon. These CTE mismatches causes the structure to warp in the manner shown below in Figure 6.1.

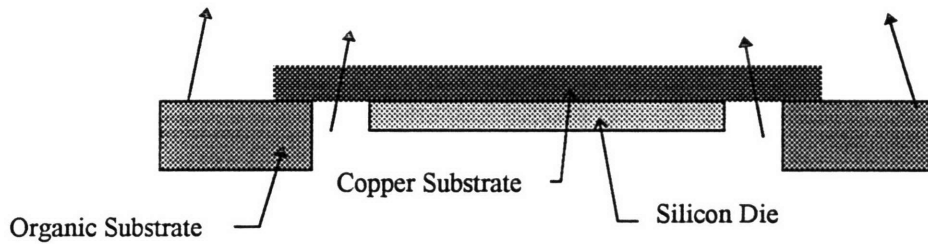


Figure 6.1-Direction of warpage upon cooling of a die-copper substrate mounted on an organic circuit board with die cavity without encapsulant. The copper has a larger CTE than both the organic board and the silicon.

The introduction of an encapsulant into the mechanical structure above creates introduces many temperature dependent and potentially many time dependent phenomena. The encapsulant Young's modulus increases at the same time the CTE decreases from it's high value of 67-72 ppm/°C to 17 ppm/°C below the glass transition temperature. As the temperature decreases the CTE of the encap approaches that of copper and the modulus increases. Without empirical measurement it becomes difficult to predict the net affect the encap material will have on the overall warpage of the package and the underlying stress state.

This study will utilize both flexus and Moiré warpage information to study the effect of the encapsulant material on the overall warpage of the package as compared to a unencapsulated package. In addition the average shear magnitude in the DA layer at the die corner was analyzed to capture the encapsulant's effect on the shear stress in that critical region. The study determined whether the strategy of encapsulation of silicon acts to compress the die effectively.

6.2 PPGA Sample Preparation

The PPGA samples were constructed of a die attached to copper slug which was then bonded to a multilayer board which routes from the die to the I/O pins on the opposite. The general structure of the PPGA is shown below in Figure 6.2 One of the samples contained a plastic encapsulant and the other did not but both were prepared in the same manner otherwise.

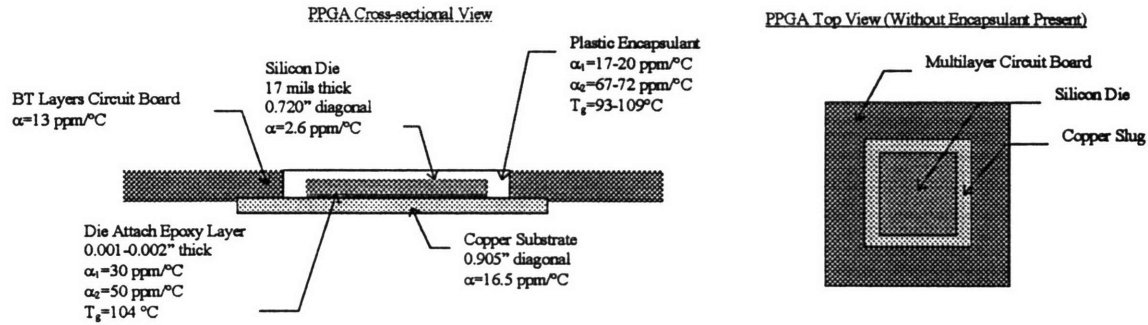


Figure 6.2-PPGA encapsulated package used in moiré and flexus testing.

The sample preparation of encapsulated PPGA packages proved the most challenging task of all and proved to be quite limiting in the study. Only one encapsulated package was successfully cross-sectioned in almost 50 attempts. The package was sectioned using the wire saw and was fixture at a 30–40° angle as described in section 3.3.1. The other packages experienced either delamination in the DA region or longitudinal die cracking similar to that illustrated in Figure 6.3 below. Several packages were also sectioned using a wafer dicing saw described in Chapter 3 and were fixtured using wax melted on a wafer. The samples were placed copper side down in the wax during cutting and exhibited identical failure phenomena to the wire sawed samples.

Notably the two failure modes occurred in almost a completely mutually exclusive manner. The fact that the die cracking and delamination did not occur in the nonencapsulated PPGAs suggests that the elastic loading or compression of the die heightened its susceptibility to crack initiation and certainly the stored elastic strain would provide the energy required to propagate the cracks through the die once initiated. A thorough study of the failure mechanisms was not conducted but these are the conclusions indicated by the observed failures.

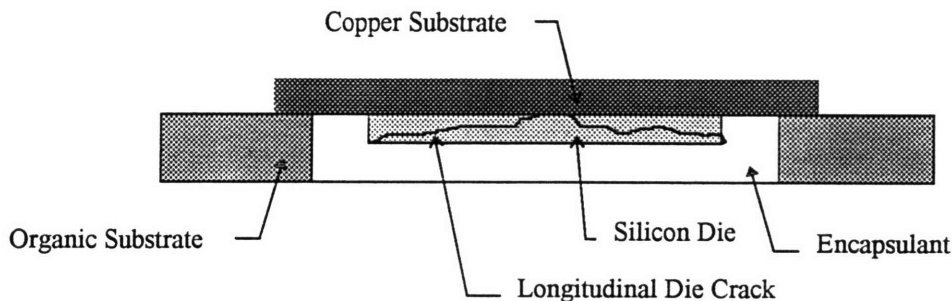


Figure 6.3-PPGA cross-section illustrating the longitudinal cracking that was the dominant failure mode of the cross-sectioned PPGA packages.

After sectioning of the two samples was completed they were measured using the Buechler optical microscope scale to verify the dimensional agreement of the two. The grating was then applied to both parts in the manner described in Chapter 3. After grating replication the extraneous grating material was removed from the edges using a razor blade to allow proper identification of the sample edges within the fringe pattern.

6.2.1 Thermal Carrier Adjustment

The PPGA samples were cycled in temperature using a thermal chamber in order to capture the fringe patterns as a function of temperature. Using these fringe patterns the warpage and strain profiles were compiled to understand how the strain state of the package changed within the temperature range of 23 to 104 °C. The same rigid body rotational carrier unintentionally introduced through the fixturing in the die bonded to substrate study was present in this study. As the chamber and stage changes in temperature, the sample undergoes slight rotation that must be adjusted in order for the displacement map or fringe pattern to represent the displacement from the center or neutral point in the sample.

The warpage fringe measurements for the nonencapsulated package were made while being centered around a point just to the side of the center. Although for shear strain measurements in the DA region this would present a problem, for warpage information the vertical displacements of both ends can simple be averaged to extract what the true displacement would have been had the carrier been centered. In fact this technique was used in nearly every warpage calculation since only rarely was the exact center of the sample identified. Whether the warpage profile appears skewed to one side or not the average value obtained does not differ from what it would be if the pattern had been perfectly centered. In the shear strain measurements, the carrier was centered as close to the center as possible to minimize discrepancies in carrier fringe between the two corners analyzed.

6.2.2 Manual Analysis Elements

The average corner shear strain calculations in the DA layer were done using the manual analysis technique defined in Chapter 2 of this study. Essentially an element of known dimensions was defined in the corner (highest shear strain) region. The number of fringes and fractional fringes intersected by the perpendicular bisectors of the rectangular element of interest defined the

average shear strain across the two bisector lines, or more generally within the element. An element was defined in the die attach bond line at the corner of the diagonally cut sample to analyze the average strain magnitude there. This region being the greatest distance from the neutral point of the die-copper interface should exhibit the highest shear strains. The manual strain calculations technique given in Chapter 2 were applied to the U and V-field fringe patterns for each temperature to obtain strain values from the fringe pattern. Figure 6.4 below illustrates a sample element defined for the analysis of encapped versus nonencapped PPGAs.

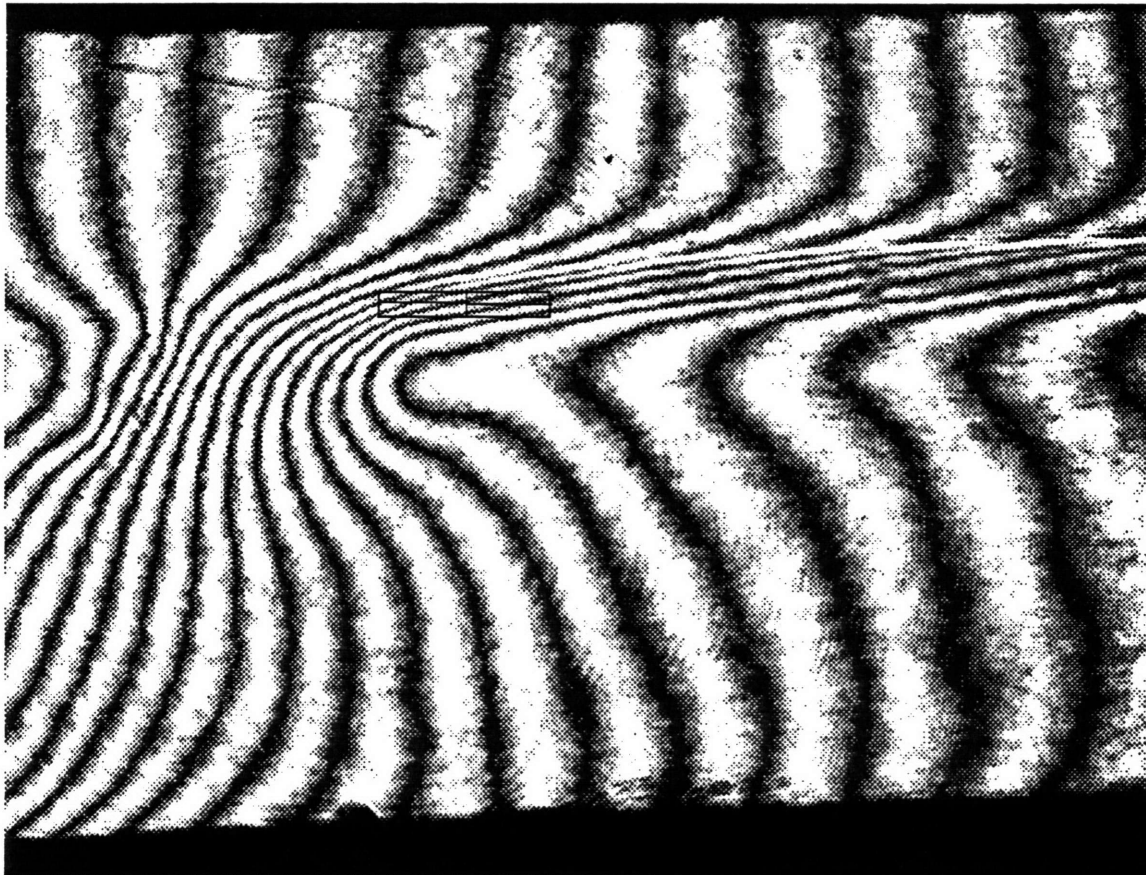


Figure 6.4-Example of the 88 x 490 μm element used for manual calculation is the PPGA.

6.2.3 Moiré Warpage Measurement

The warpage of the exterior surface of the silicon and copper slug were analyzed as a function of distance from neutral point (DNP) and temperature. Clearly the information regarding warpage as a function of DNP relies on the carrier being centered or otherwise the average of the values from the two identical DNPs must be taken. To measure vertical displacement the V-Field

fringe patterns are analyzed since the vertical displacement of the die at the point that a fringe intersects the top surface of the die represents an incremental vertical displacement of 417 nanometers (0.417 μm). With the carrier centered approximately about the neutral point the DNP of each fringe was recorded to generate the vertical displacement (warpage) versus DNP curves for each temperature.

6.3 Shear Strain Analysis Results

Using the environmental chamber the samples were analyzed at 2-5 °C increments between 23 and 100 °C. Using the combined U and V-Field fringe pattern information the average shear strain was then calculated for the elements. A profile of the strain magnitudes for the same corner in the encapsulated and unencapsulated samples was collected. Originally the intent was to compare both sides of the packages, but grating flaws precluded the analysis of side two on the unencapsulated package. The strain profile data is shown below in Figure 6.5 where the encapsulated exhibited an accumulated shear strain at 23 °C of ~0.45% whereas the unencapsulated package exhibited as much as ~1.5% shear. The encapsulant caused a factor of three reduction in shear strain in the die attach layer where accelerated life testing (ALT) has shown the failures occur.

Accumulated DA Shear Strain

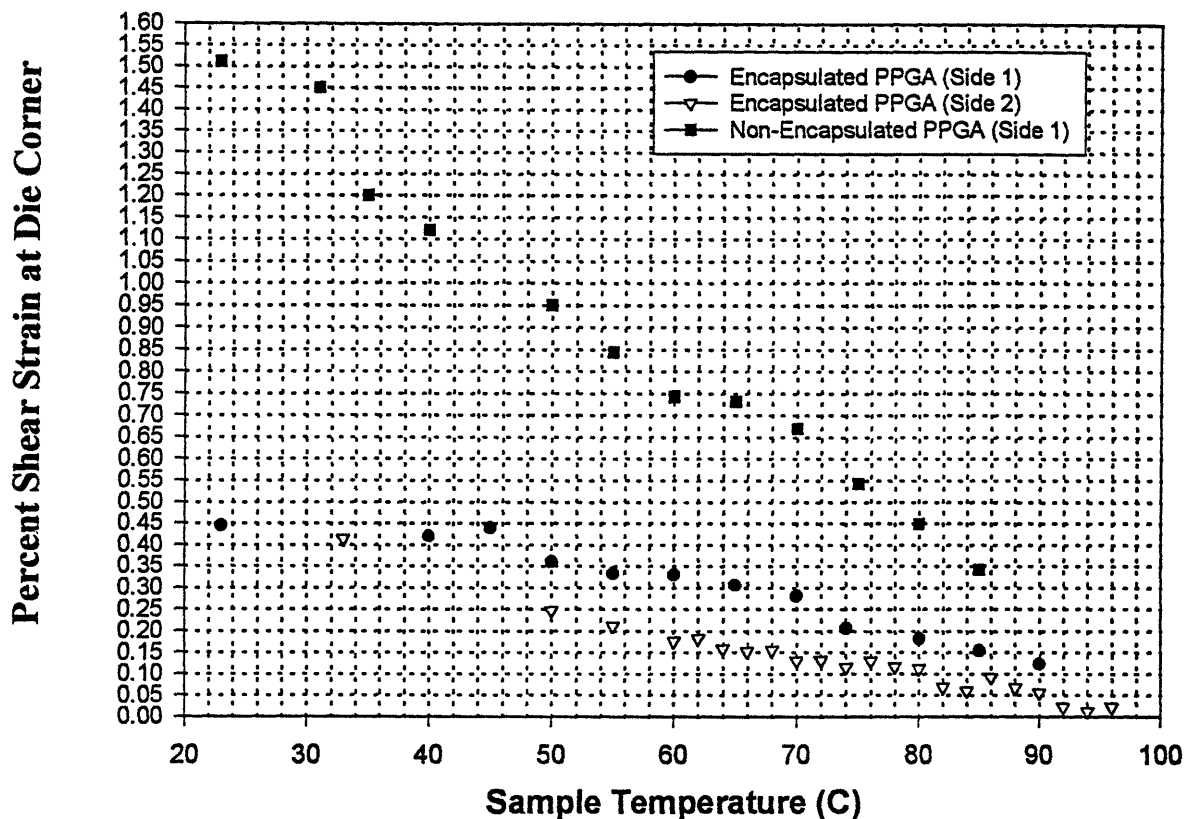


Figure 6.5-Strain profile data for encapsulated and unencapsulated PPGAs illustrating the effectiveness of the encapsulant in reducing the shear strain the critical die attach bond layer.

6.4 Slug and Die Warpage Results

In approaching the task of analyzing the warpage of a large and complex package such as the encapsulated PPGA it is necessary to note several details of the measurement process. Moiré does not yield absolute displacement information, but rather the relative change in displacement from the grating replication temperature to the temperature represented in a fringe pattern. Thus for a simple die-bonded to substrate system since the analysis does not pass through any glass transition temperatures the strain trends are rather intuitive and simple. By adding two polymeric systems, the die attach epoxy and the encapsulant, both with glass transitions within the range of the analysis, the strain profile is expectedly more complex. Without the encapsulant we do not see a similar trend to the die bonded to substrate case indicating that it is the encapsulate which is introducing most of the complexities. In approaching the problem a series of slug warpage curves

for encapsulated parts obtained by flexus was used to validate the observed moiré strain values and vertical displacement trends.

As in the die bonded to substrate samples in Chapter 5, the CCD camera resolution required both samples to be analyzed in halves. The two data sets were then combined to yield the vertical displacement verses DNP. In the unencapsulated sample it should be noted that the fringe pattern was centered just left of center yielding a skewed profile. A correction for this variation is described earlier in section 6.2.1. Since failures in the packages have occurred at both the die attach bond line and the copper substrate-organic board bond line, both the slug and die warpage values were sought.

The slug warpage profiles for the encapsulated and non-encapsulated samples are shown below in Figures 6.6 and 6.7 where it is evident that the same relative displacement trends present in the encapsulated PPGA are not in the uncapped PPGA.

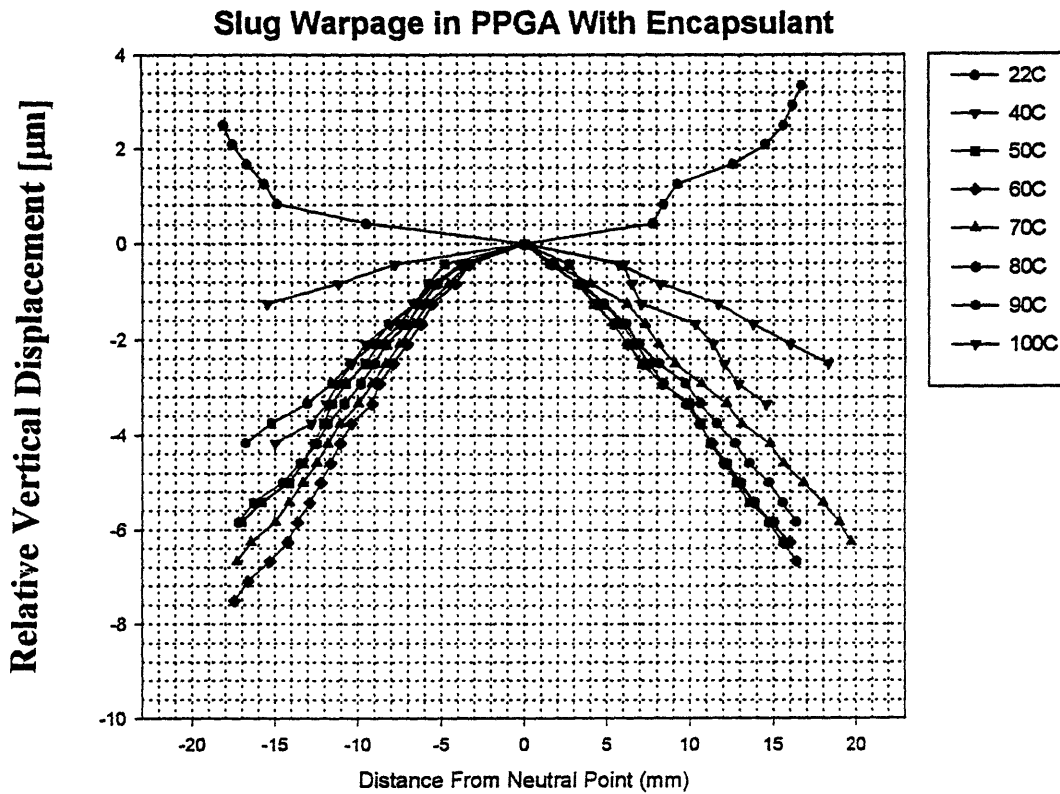


Figure 6.6-Warpage profile of encapsulated PPGA exhibiting a reversal in relative warpage direction(slug oriented up).

In the vertical slug displacement profiles the slug is oriented up similar to Figure 6.1 and a negative warpage is one with the copper substrate exhibits more concave down bending (or less concave up in an absolute sense) and the amount of the displacement of the corners in the negative y direction is the negative magnitude. That is to say that the magnitude of relative concave down displacement is represented by an equal concave down representation on the warpage plot. Generally the slug was observed to have begun in a relative sense to bow concave down initially upon cooling from 104 °C. In the 70-80 °C range however, the direction of relative warpage began to move in the concave up direction, or decrease in magnitude. In fact the net relative warpage of the package became concave up somewhere between 40 and 22 °C. Juristically the slug was warped in an absolute sense in a concave up manner, upon cooling became less concave, upon further cooling returned to the initial level of concavity and finally at room temperature reached an even higher level of concavity. The absolute warpage was therefore a concave up curvature throughout the temperature range of the analysis. The actual warpage values for the encapsulated versus unencapsulated packages is given below in Table 6.1.

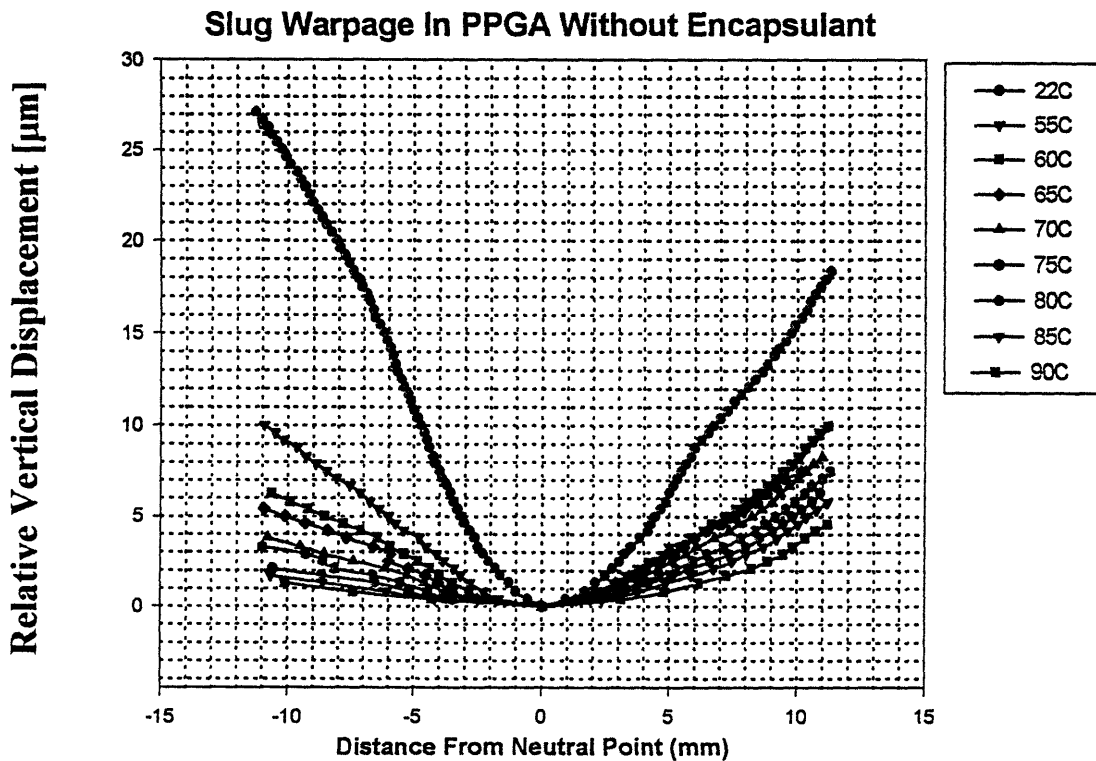


Figure 6.7-Warpage profile for unencapsulated PPGA exhibiting a monotonically increasing warpage with temperature decrease.

In the absence of the encapsulant material the warpage profile of the PPGA is significantly different than the encapsulated sample. As the plastic encapsulant is cooled its mechanical properties change as it passes through the glass transition temperature. In the temperature range surrounding the T_g the CTE of the material decreases while the modulus increases. This effect leads to the relative warpage reversal observed in the encapped package. The same differences in encapsulated versus unencapsulated PPGA slug warpage were also noted in the die warpage measurements as seen in Figures 6.8 and 6.9.

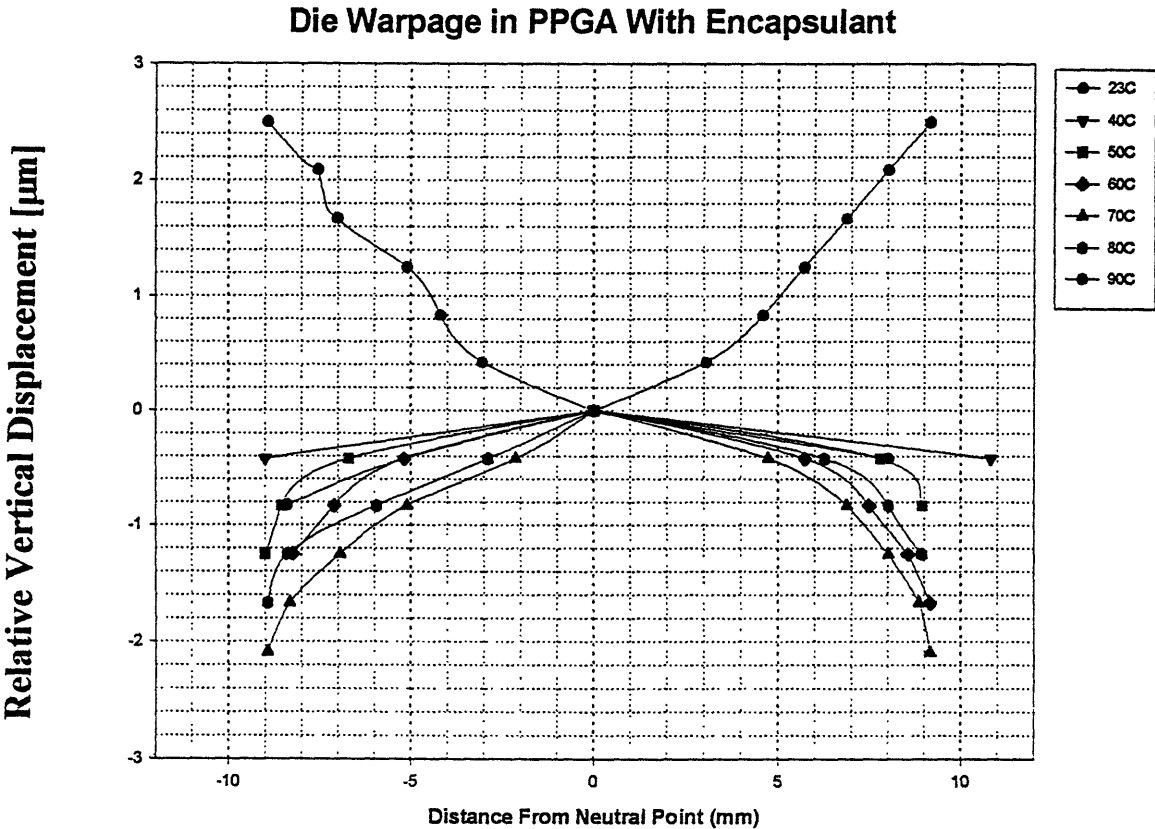


Figure 6.8-Warpage Profile in die of encapsulated PPGA exhibit relative warpage reversal between 23 and 40 °C.

The relative warpage reversal observed in the die corresponded to the same reversal in the slug warpage in the same temperature range. The correlation is not surprising since the die and copper substrate are essentially mechanically coupled it is useful however to insure that the vertical displacement analysis was conducted properly. Like the encapped sample the die in the unencapsulated sample

exhibited similar behavior to its copper substrate. Again the data appears skewed in the profile but will be averaged in the summary table in the previously described manner.

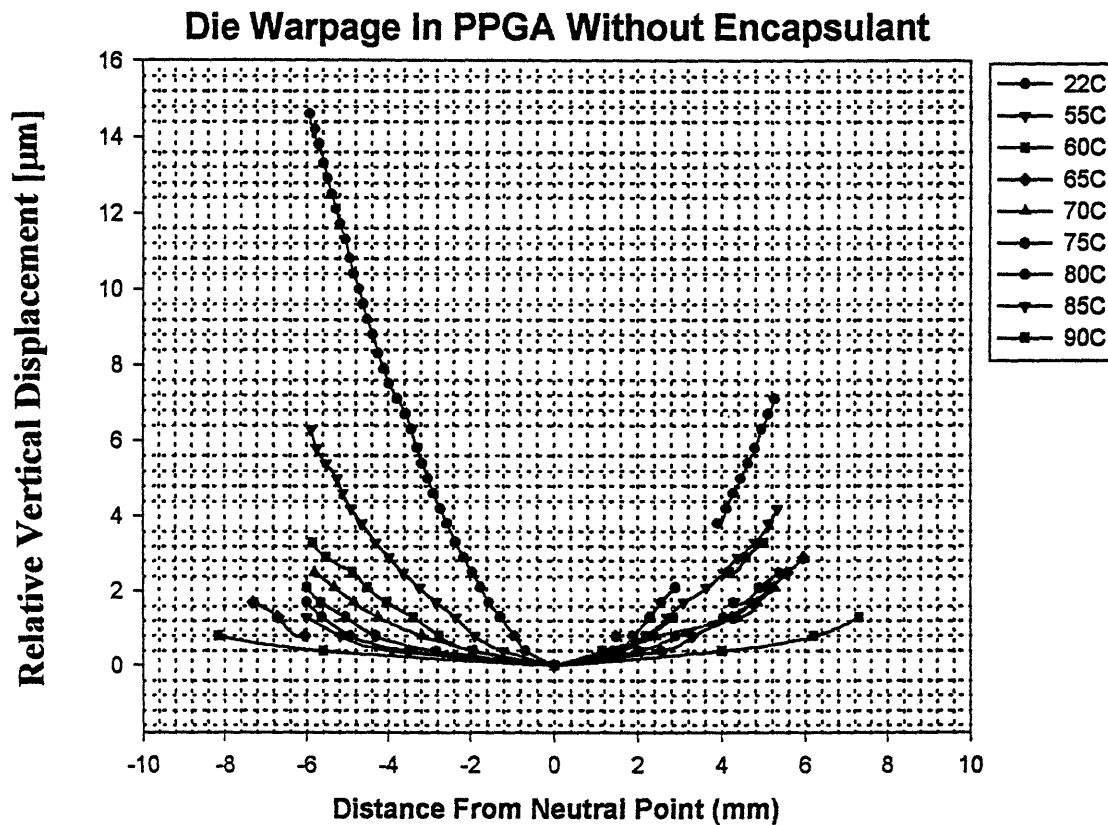


Figure 6.9-Unencapsulated PPGA die warpage profile exhibiting constant strain accumulation similar to the copper slug in the same package.

To be able to compare the data between the two samples the apparent differences in carrier adjustment must be eliminated to allow the temperature by temperature comparison of the warpage values. As described in section 6.2.1 the data for die and slug warpage of both packages has been averaged to eliminate the carrier bias and compiled in Figures 6.10 and Table 6.1 below. In the following section the flexus data collected for the same encapsulated package type will be compared with the moiré data as a means of validation. With the aid of the flexus data the complicate mechanical phenomena occurring within the encapsulated packages will be addressed.

Vertical Displacement Relative to Amount Present at 104 C of Encapsulated and Unencapsulated PPGAs

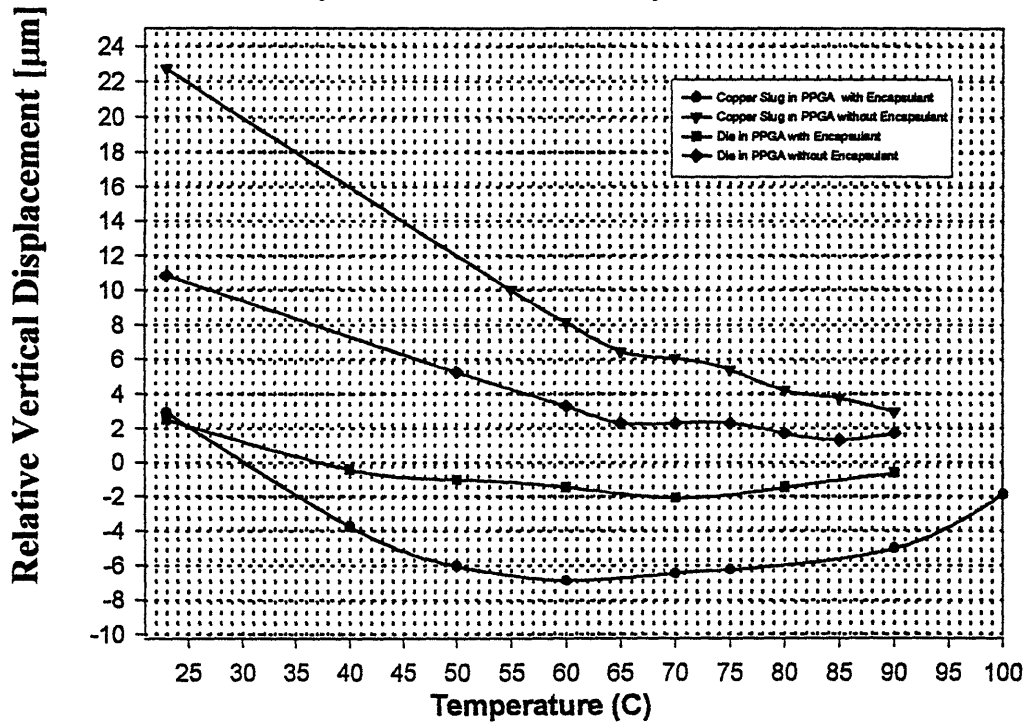


Figure 6.10-Profile of the vertical displacement of the copper and die relative to the absolute preexisting warpage magnitude at 104 °C. The encapsulated PPGA first decreases in absolute warpage magnitude before increasing again. The unencapsulated PPGA increases consistently with decreasing temperature.

<u>Temp (C)</u>	<u>Copper with Encapsulant</u>	<u>Copper without Encapsulant</u>	<u>Die with Encapsulant</u>	<u>Die without Encapsulant</u>
23	2.92	22.73	2.5	10.85
40	-3.755		-0.42	
45				
50	-6.05		-1.04	5.25
55		10		
60	-6.885	8.15	-1.46	3.3
65		6.45		2.3
70	-6.465	6.05	-2.09	2.3
75	-6.255	5.4		2.3
80		4.2	-1.46	1.7
85		3.75		1.3
90	-5.005	2.95	-0.625	1.7
100	-1.875			

Table 6.1-Relative vertical displacement values obtained by averaging the two values for both corners of the slug or die for each temperature.

6.5 Flexus Warpage Analysis

In an effort to verify the validity of the observed warpage direction reversal in the encapsulated PPGA, flexus data was obtained for the same package structure. The flexus measurement analyzes absolute warpage inherently whereas the moiré is only capable of measuring absolute warpage if the grating replication temperature coincides with the state of zero warpage in the package. Since 104 °C does not coincide with this temperature, moiré fringes will represent the warpage accumulated upon cooling from 104 °C, a relative measure. By calculating the change in the absolute measure of flexus from the value at 104 °C a basis of comparison of the two data sets is established. The absolute warpage measure of the slug is given below in Figure 6.11.

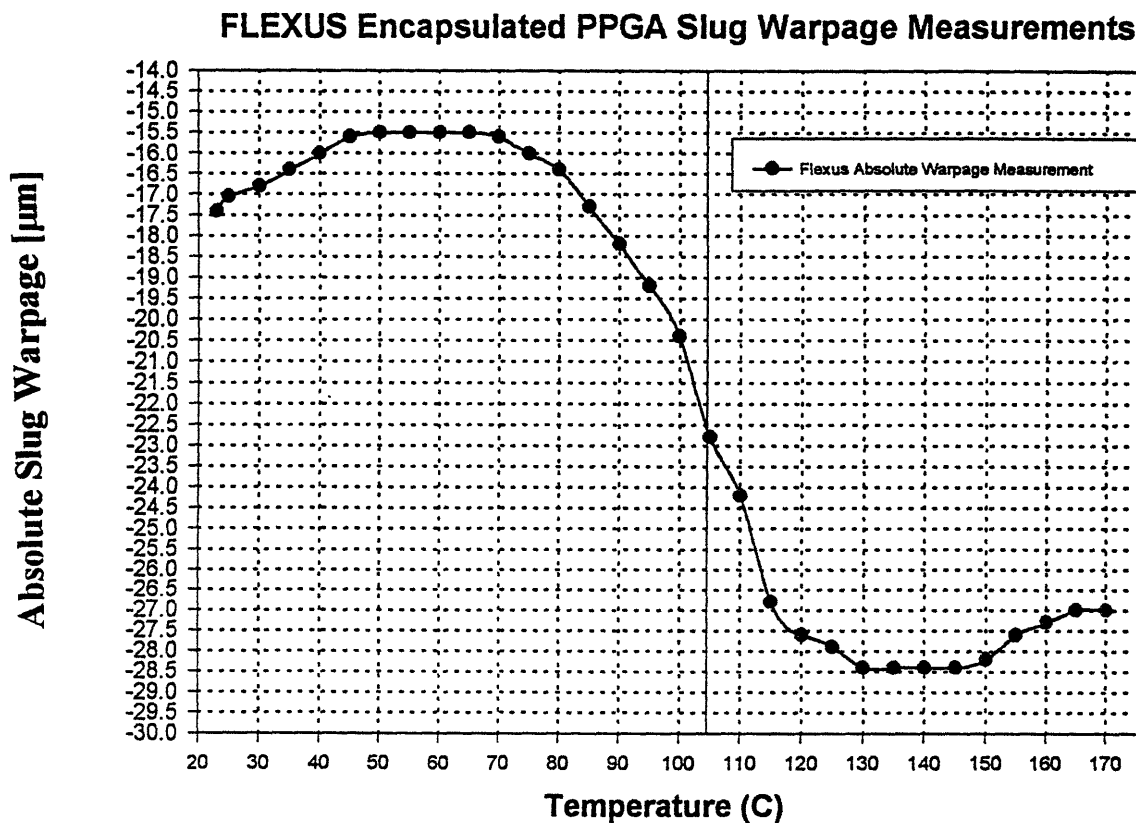


Figure 6.11-Absolute warpage measurements of encapsulated PPGA slugs as a function of temperature. The vertical line passes through the value used as the basis for relative measurement below 104°C.

By calculating the accumulated or decrease in warpage from the 104 °C baseline in the flexus we are able to compare with the values directly to the moiré data. The change in the

magnitude of the absolute warpage value at 104 °C as measured by moiré and flexus is shown below in Figure 6.12.

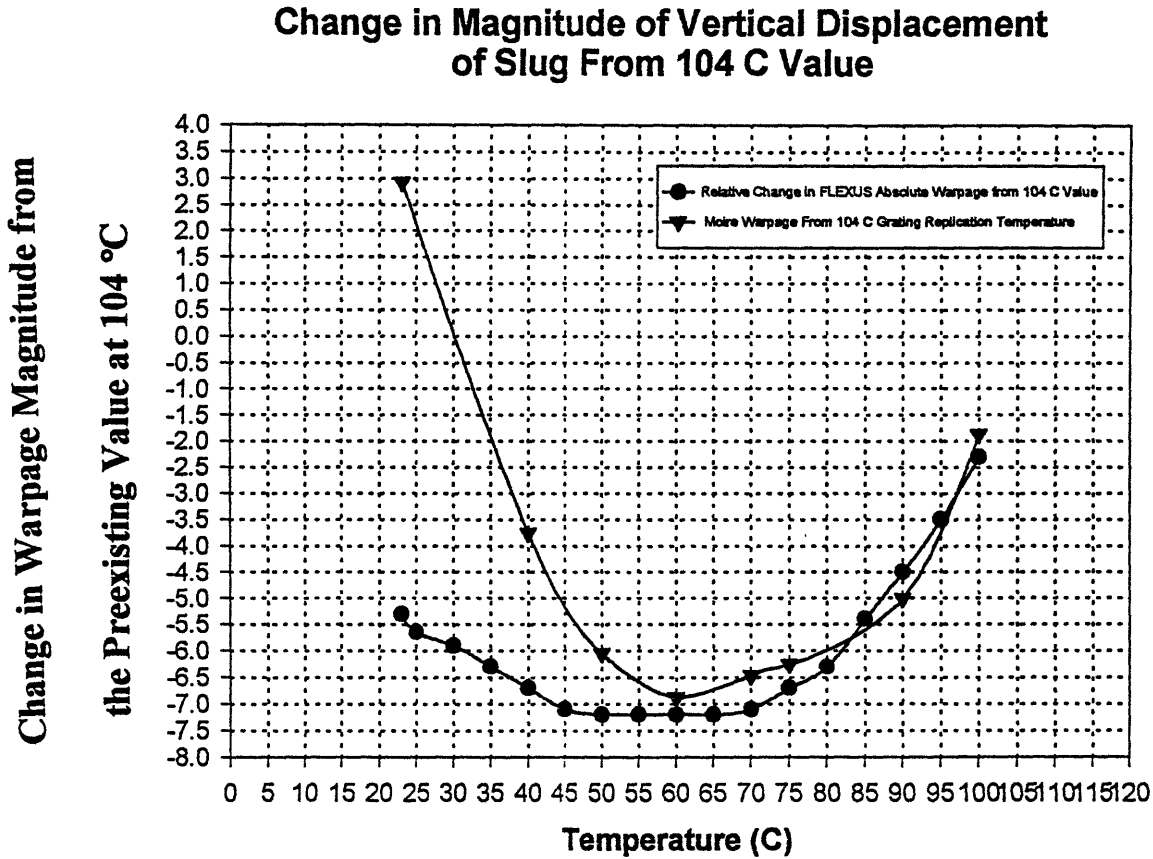


Figure 6.12-Relative change in PPGA slug warpage magnitude with respect to the absolute warpage state at 104 °C as measured by moiré and flexus.

The two measures correspond very well in terms of the trend present in which the warpage initially decreases in magnitude and then begins accumulating. Given that the fringe density is proportional to the resolution of strain in moiré it is expected that the moiré data is more accurate since at room temperature the fringe density should be highest. The flexus data may also differ because of sample to sample variation as well as the fact that the moiré sample is only half of a package.

6.6 Summary

An assessment of the effect of plastic encapsulants on the stress state in critical regions in PPGA packages was conducted using both shear and warpage data. Sample preparation issues limited the number of packages that could be analyzed however, flexus data for structurally identical encapsulated packages exhibited nearly identical warpage trends to the one observed using moiré. Generally upon cooling from a higher temperature, the copper slug experienced greater thermomechanical contraction than the organic board and die. This causes the unencapsulated structure to accumulate ~22.73 microns in slug corner vertical displacement upon cooling from 104 °C. This was compared to both moiré and flexus data for encapsulated, but otherwise identical packages showing that over the same range the warpage accumulated was ~2.92 μm and ~5.30 μm respectively. The value of relative strain accumulation with temperature measure by moiré and flexus in encapsulated packages was almost identical over most of the temperature range as shown in Figure 6.12. The divergence of the two measures at lower temperatures could be attributed to cooling rates, and the absence of half of the package in the moiré case.

The mechanism by which the encapsulant decreases the package warpage and underlying stress levels is in a general sense by compressing the silicon die (CTE ~2.6 ppm/°C) such that the compression strain imparted by the higher CTE (17-72 ppm/°C) encapsulant decreases the magnitude of the mismatch strain and the resulting DA shear strain value. The effect of the die compression can also be viewed as giving the silicon a higher apparent CTE thereby decreasing the $\Delta\alpha$ for the copper and silicon. The mismatch and warpage strain components are deminished by the encapsulant compression. By manually calculated strain values shown in Figures 6.5 the presence of the encapsulant decreases the maximum die attach shear strain from ~1.5% to ~0.45%. Thus for the encapsulated packages the fatigue life is significantly enhanced over the unencapsulated package.

The benefits of plastic encapsulation of PPGA packages have been demonstrated clearly through the decrease in shear strain and warpage by a factor of ~3.3. Embedded within this phenomena is a very complex elastic and viscoelastic mechanism by which the strain decrease is realized. Revisiting Figure 6.11, the absolute warpage measurement for the encapsulated PPGA slug versus temperature, the warpage begins decreasing rapidly below ~120 °C. The trend continues to ~85 °C where the curve again levels out. Noting that the T_g for the plastic

encapsulant is between 93 and 109 °C and in cooling through the glass transition the CTE for the encapsulant changes from ~72 ppm/°C to ~17 ppm/°C. During this temperature range the Young's modulus of the material changes from being on the order of hundreds of MPa to ~8 GPa. Thus the thermomechanical strain accumulation in the encapsulant as dictated by the CTE is still greater than that of copper as the Young's modulus increases to a more significant 8 GPa value.

Clearly above the glass transition temperature the CTE of the plastic encapsulant is ~72 ppm/°C and thus in cooling from 150 °C the thermomechanical strain accumulation rate is higher in the encapsulant, however with such a small modulus the influence of the encapsulant on the monolithic package warpage value is insignificant. The compressive stress imparted by the encapsulant in the 150 to 120 °C range is negligible in impact and is continually dissipated through viscoelastic and plastic flow of the encap. As the encapsulant is cooled throughout the glass transition temperature, the CTE value remains at a premium to the copper and the Young's modulus increases rapidly to a non-negligible quantity. This causes the encapsulant to influence the monolithic stress state of the package more significantly as shown by the flexus data. Upon cooling from 120 to 85 °C in absolute terms the warpage magnitude is decreased by 22.73 µm. The cooling rates for flexus were ~3 °C/min essentially limiting the viscoelastic strain relaxation that can occur as the stress in the encapsulant increases.

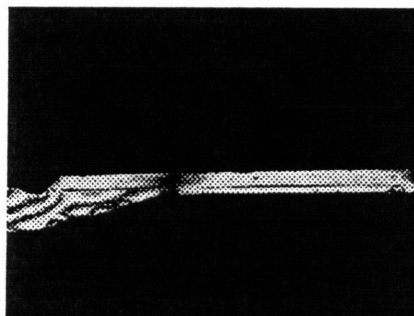
As 85 °C is approached the relatively compressive behavior of the encapsulant begins diminishing in influence of the monolithic stress state of the package. First, the CTE of the encapsulant begins approaching that of the copper substrate (16.5 ppm/°C). This diminishes the ability of the encapsulant to decrease the warpage magnitude in the copper dominated package. flexus and moiré data show that at 60 °C the package begins accumulating warpage again since the encapsulant is contracting at roughly the same rate and has a Young's modulus of only 8 GPa as compared to Copper, 120.6 GPa. This phenomena is illustrated by Figure 6.12 although the two data sets disagree on the rate of strain accumulation beyond the minimum.

Thus using moiré and flexus it has been demonstrated that the encapsulant material properties can have a significant effect on the monolithic stress accumulation in PPGA packages. Furthermore moiré can be implemented to evaluate the effectiveness of plastic encapsulant materials in decreasing package warpage and die attach shear.

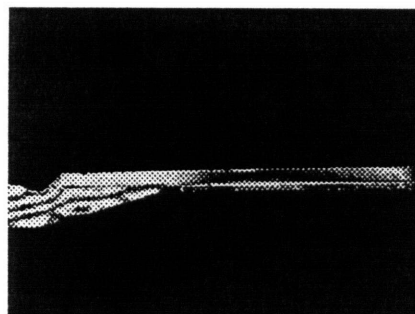
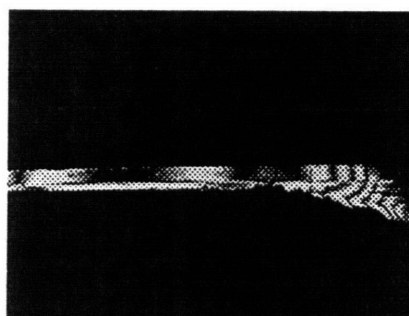
Unencapsulated PPGA V-field Fringe Patterns

Left

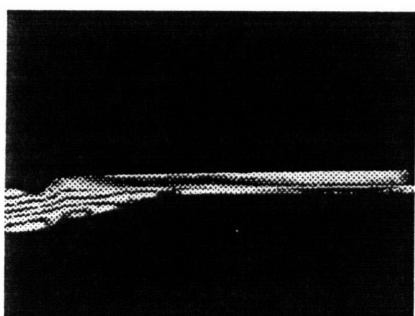
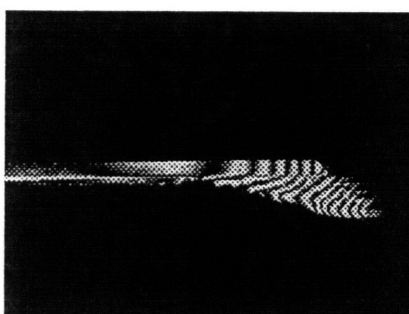
Right



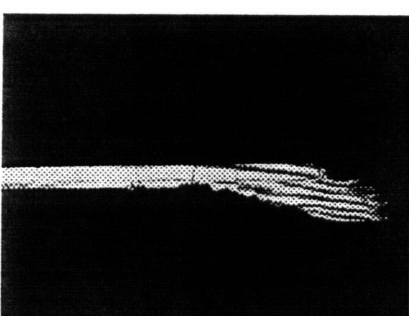
102°C

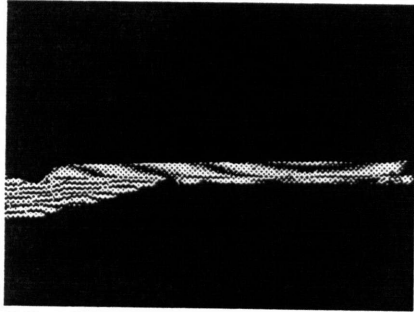


100 °C

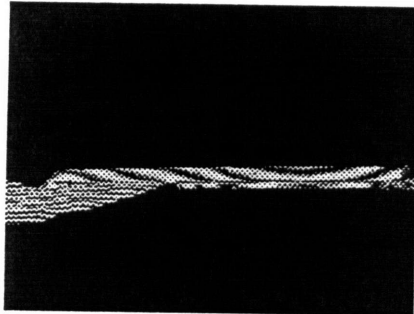
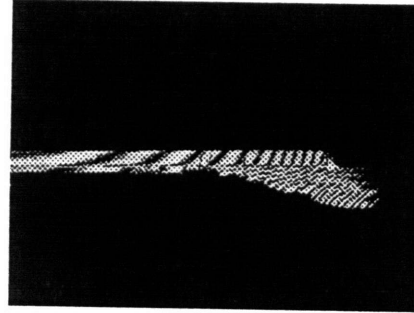


95 °C

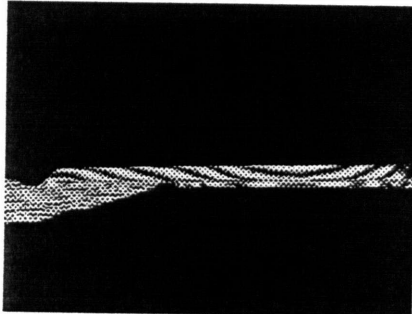
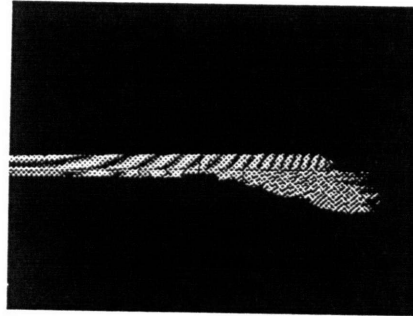




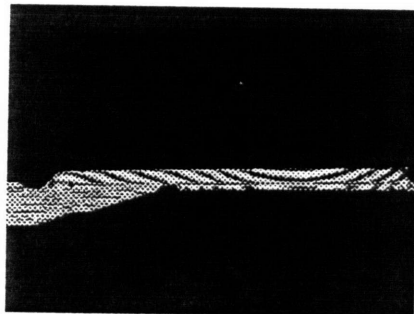
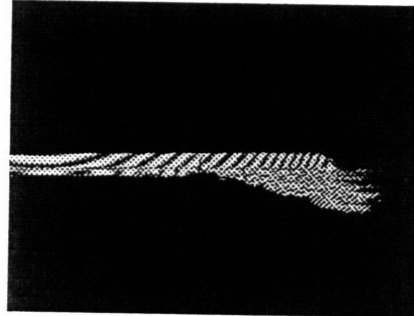
90 °C



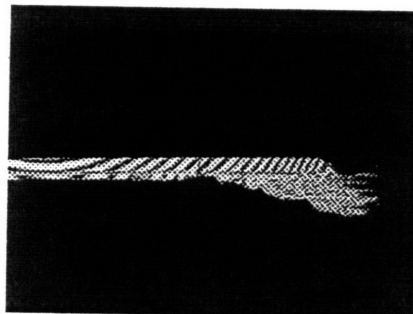
85 °C

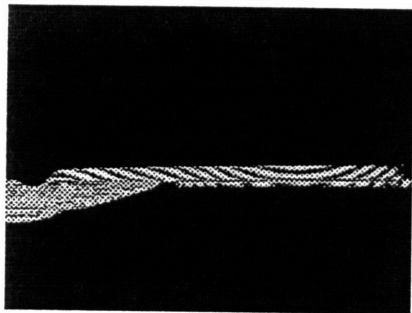


80 °C

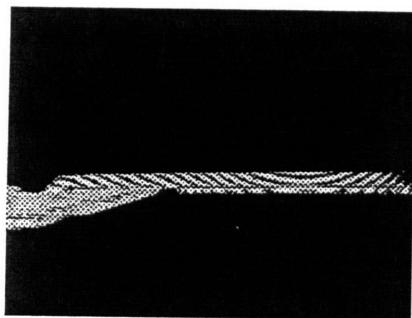
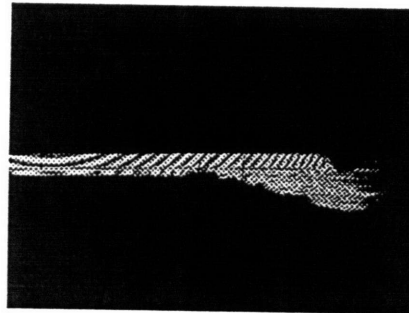


75 °C

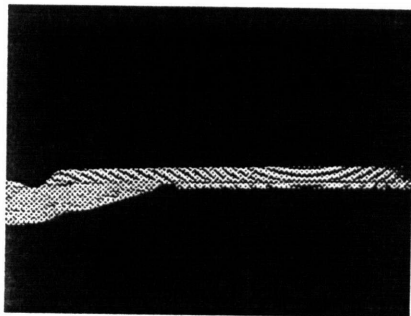
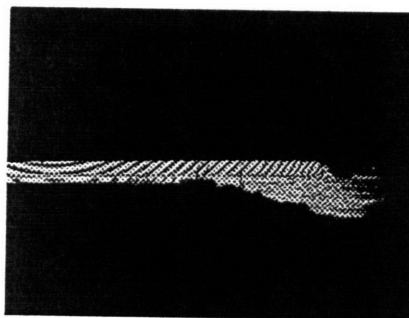




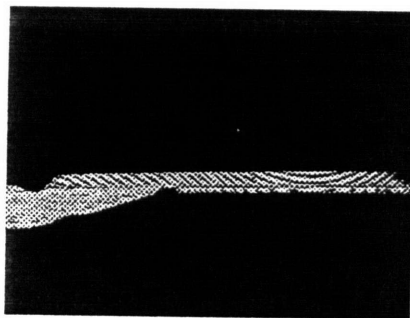
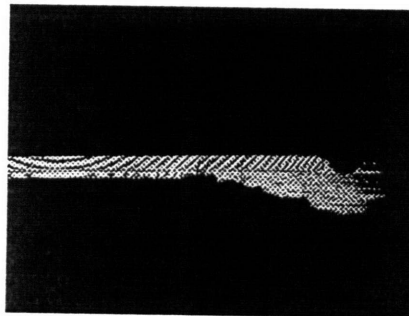
70 °C



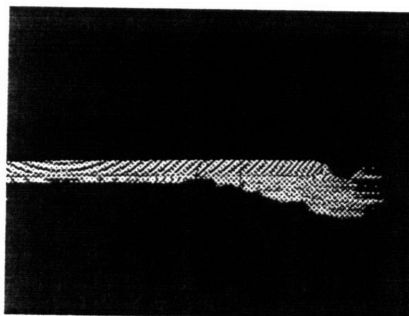
65 °C

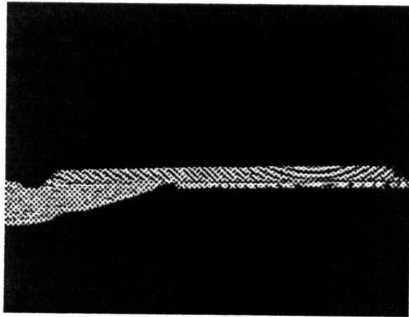


60 °C

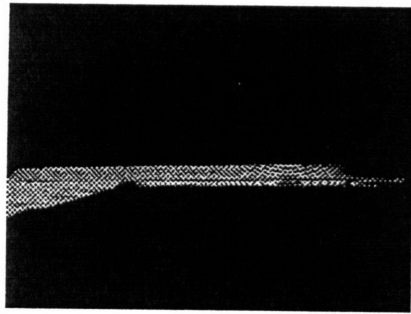
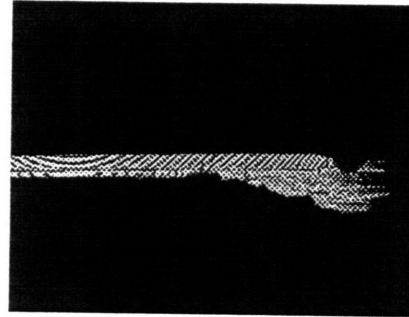


55 °C

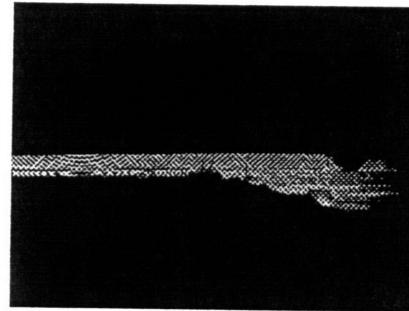




50 °C

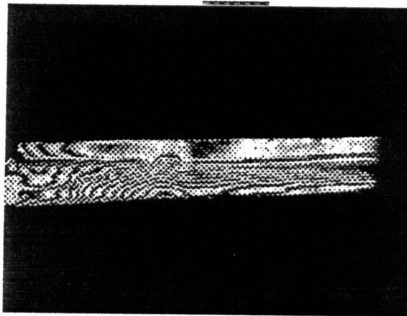


23 °C



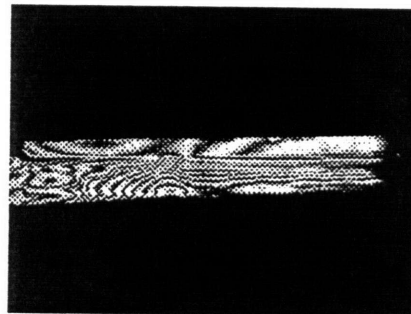
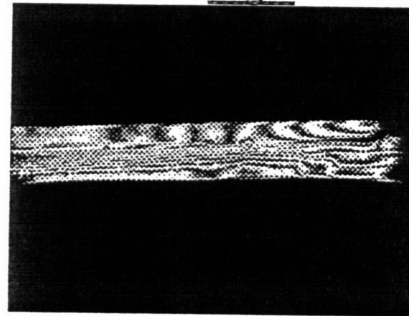
Encapsulated PPGA V-field Fringe Patterns

Left

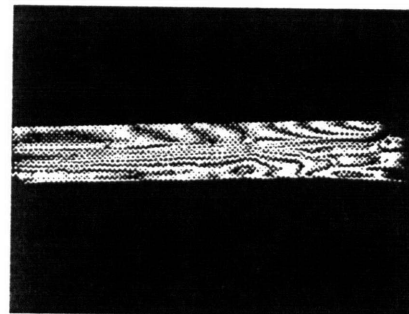


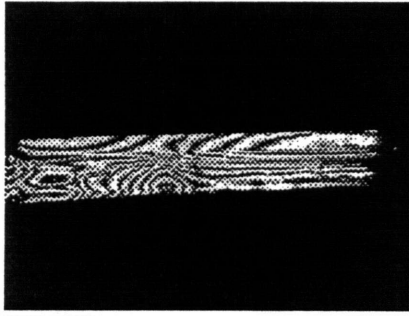
104 °C

Right

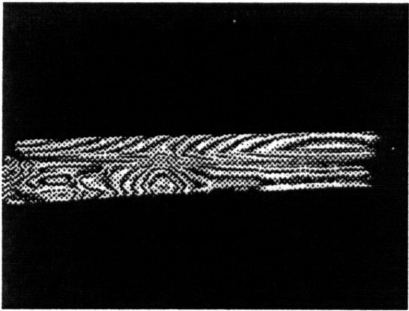
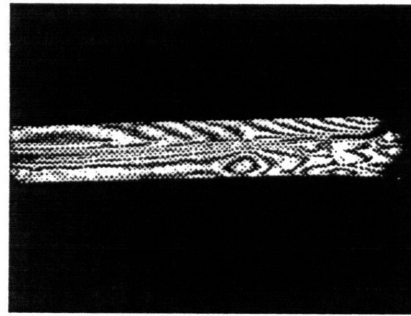


100 °C

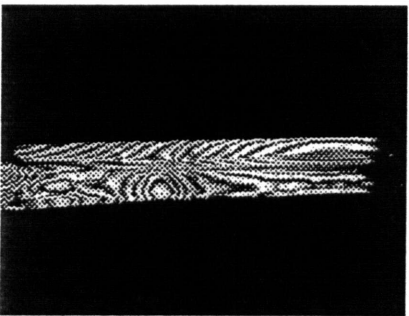
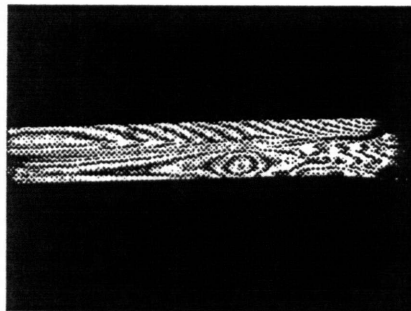




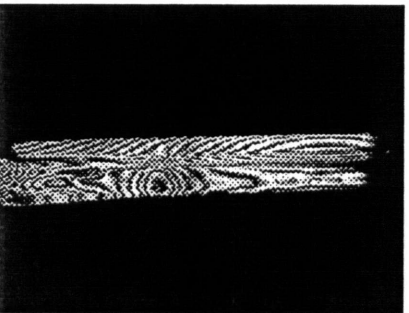
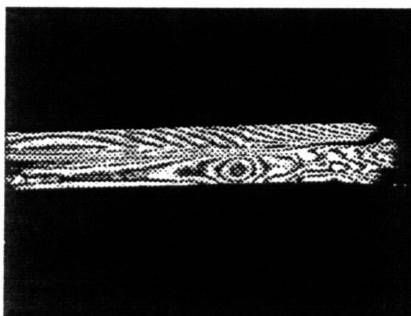
95 °C



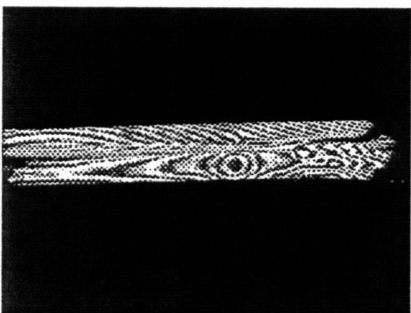
90 °C

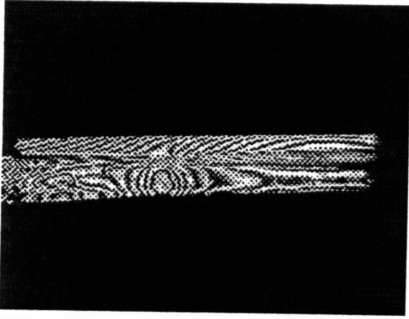


85 °C

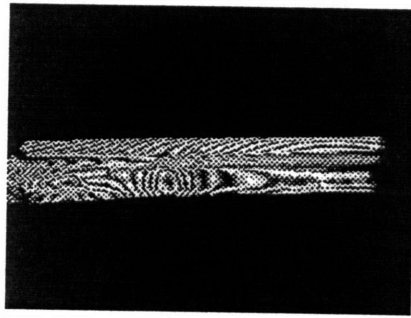
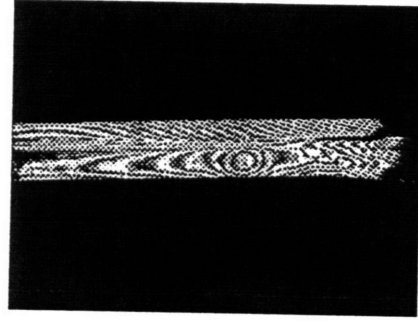


80 °C

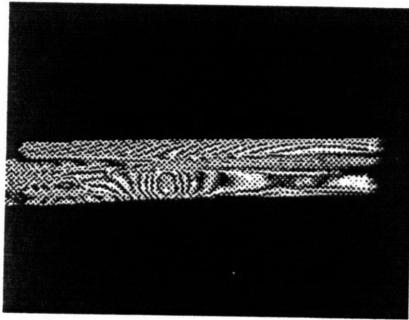
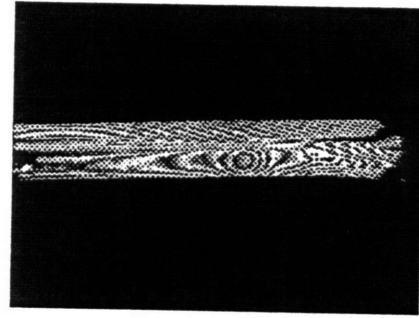




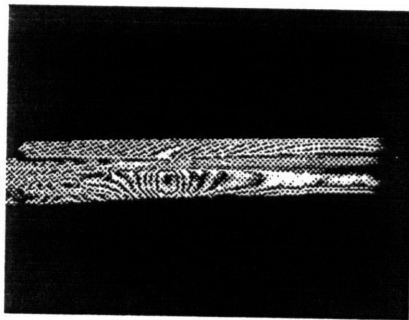
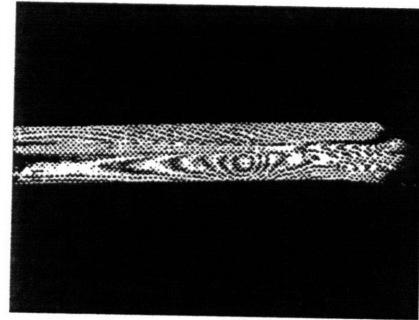
75 °C



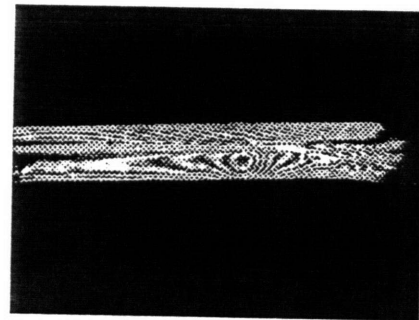
70 °C

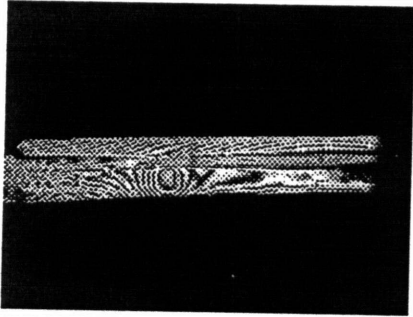


65 °C

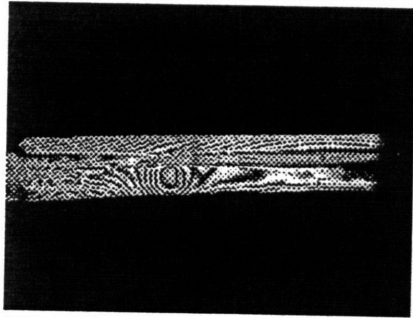
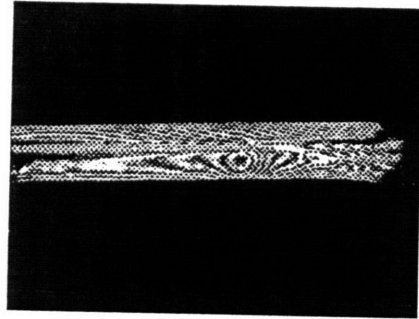


60 °C

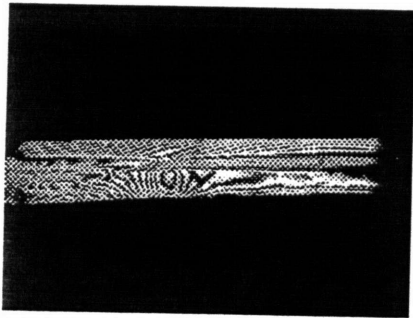
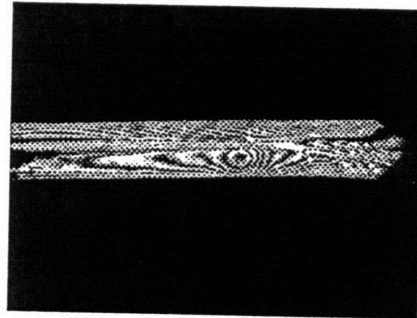




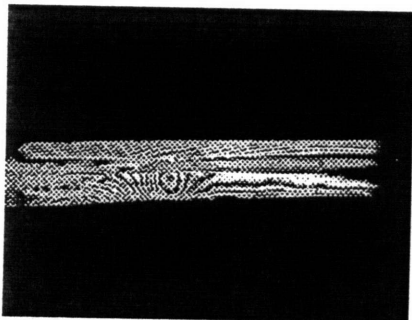
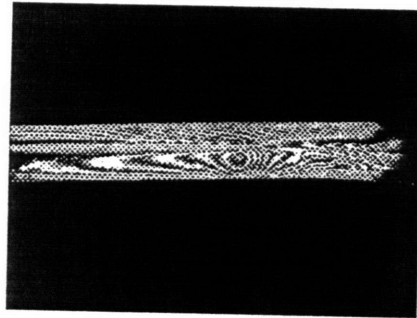
60 °C



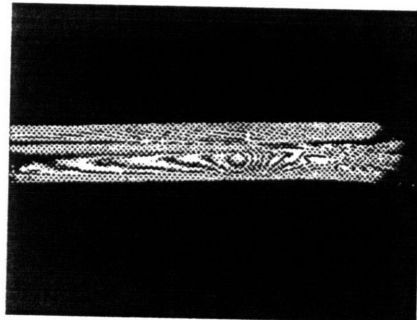
55 °C

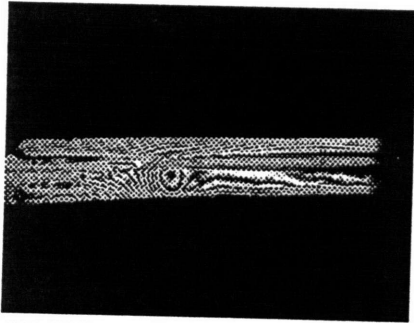


50 °C

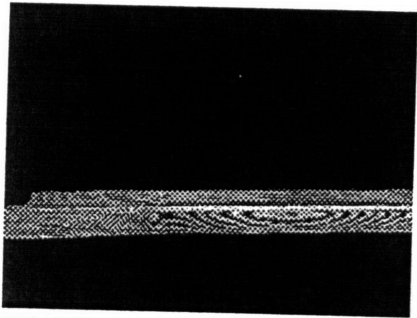
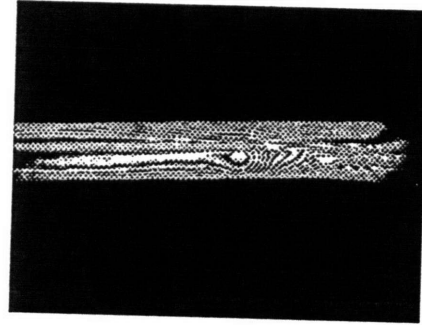


45 °C

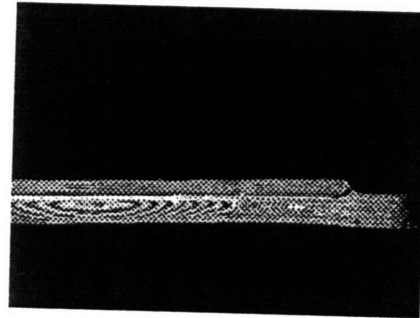




40 °C

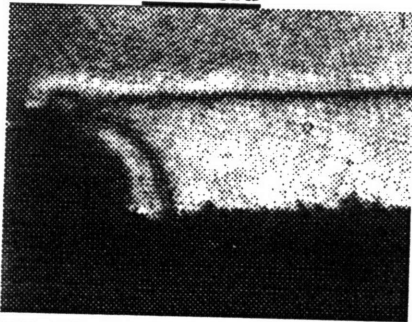


23 °C



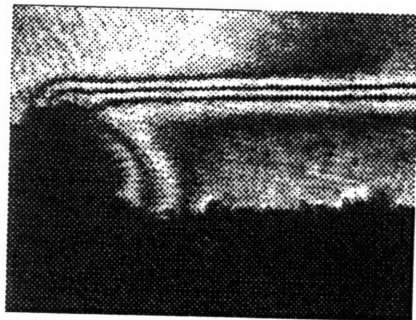
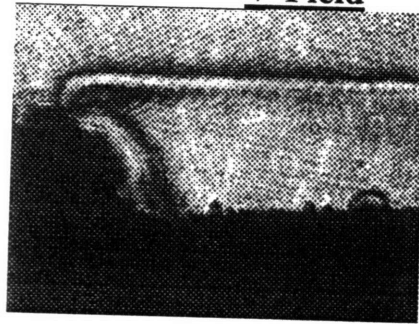
Die Attach Shear in Unencapsulated PPGA

U-Field

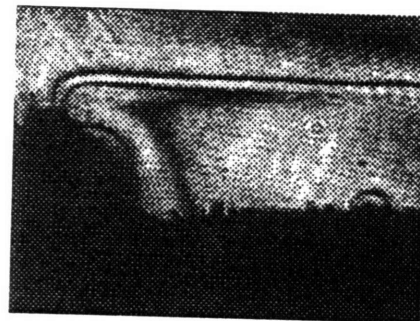


90 °C

V-Field

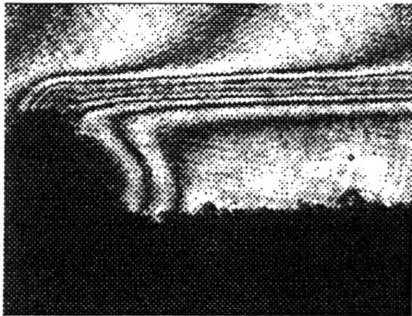
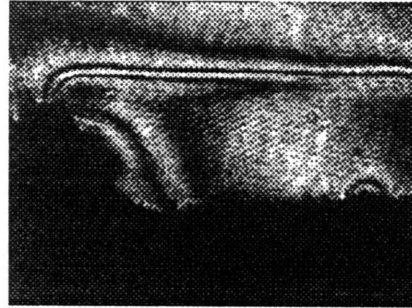


80 °C

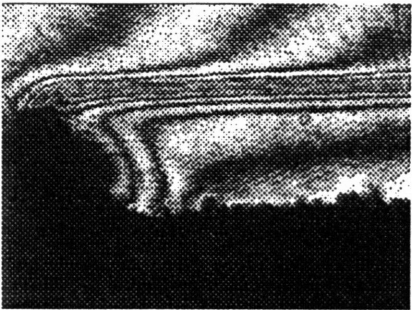
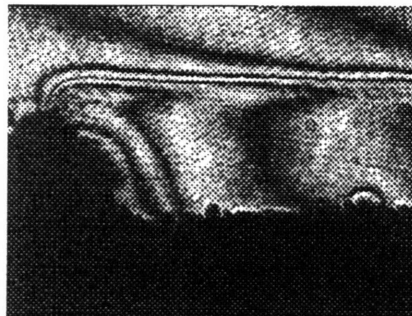




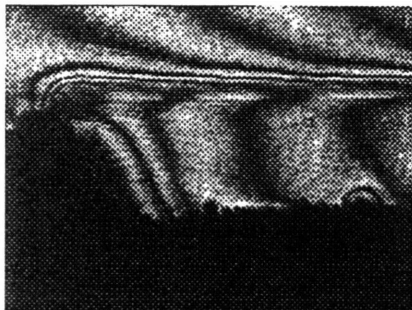
70 °C



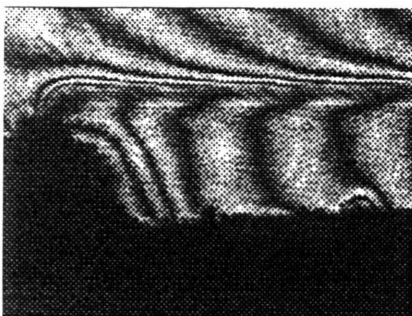
60 °C

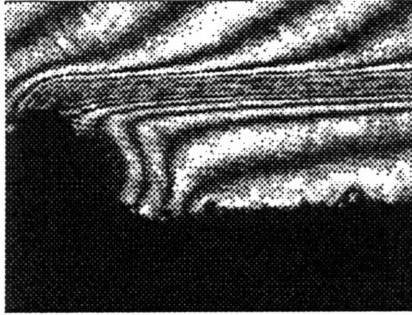


50 °C

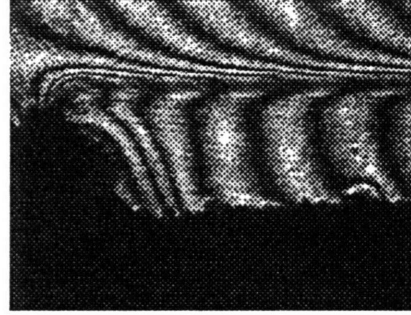


40 °C





30 °C



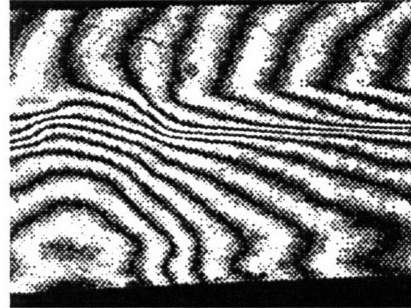
Die Attach Shear in Encapsulated PPGA

U-Field

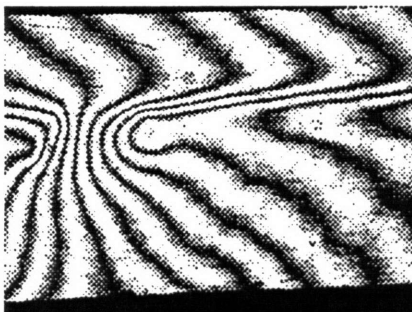
V-Field



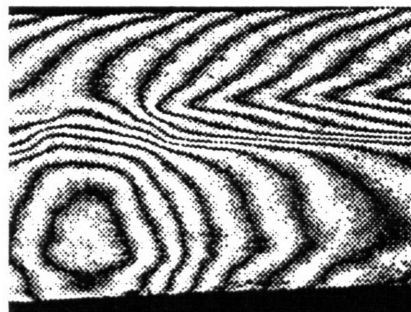
90 °C

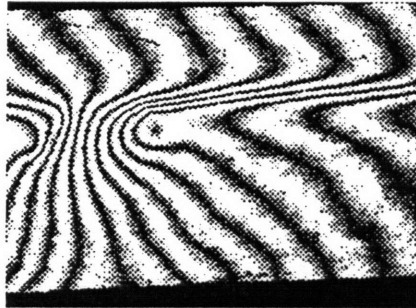


80 °C

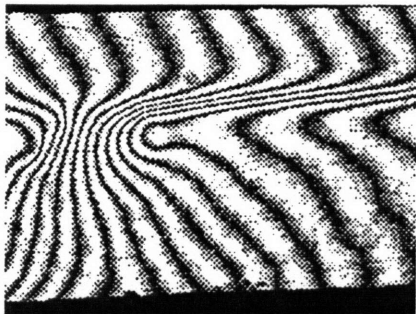
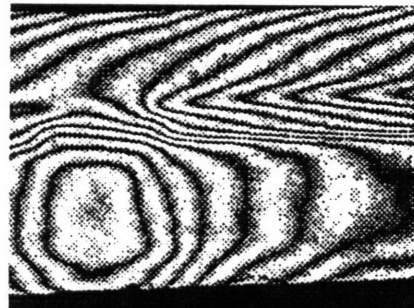


70 °C

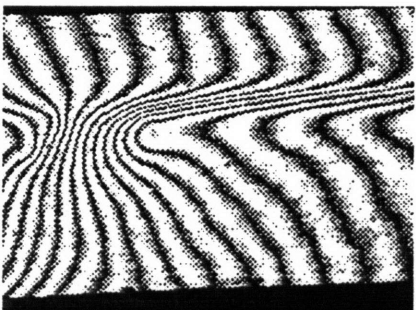
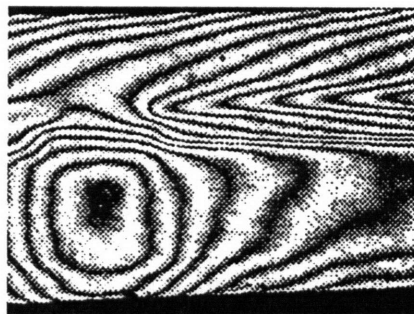




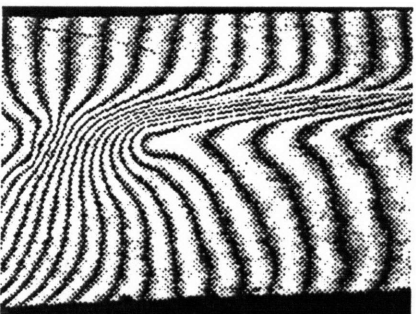
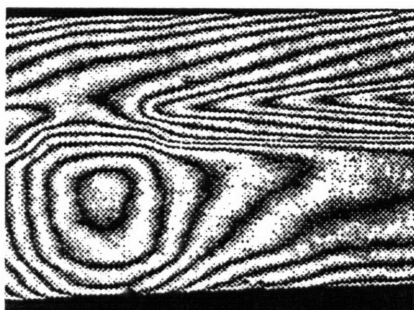
60 °C



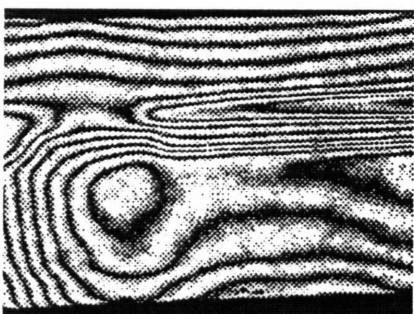
50 °C



40 °C



23 °C



Chapter 7

Computational Moiré Fringe Analysis of Aluminum and PPGA Die Attach Layer

7.1 Introduction

Although the sensitivity and versatility of moiré is almost unparalleled among other techniques the full potential of the technique can not be realized without an analysis method which considers the continuous strain information in each fringe pattern. A discrete manual analysis technique such as the one used in Chapters 4 through 7 are limited in that higher resolution requires smaller elements which in turn guarantees fewer fringes and greater fringe counting error. These competing phenomena can only be overcome digitally, that is by digitizing images and interpreting them in an approximately continuous manner.

This chapter will demonstrate computational fringe analysis on a bulk aluminum specimen exhibiting only normal strains, and then the die attach region on the encapsulated PPGA discussed in Chapter 6 of this thesis. Since in both cases the preparation of the samples were already described in Chapters 4 and 6, that part of the process are addressed only superficially. A detailed discussion of computational fringe analysis using the software package CAFRAN is given in Chapter 2. The specific parameters and for capturing, filtering and interpreting the two samples are given herein. First the general constructs of the image interpretation process are discussed in a practical sense. Next the actual image analysis and resulting strain maps will be presented and interpreted. Finally the results are contrasted with the results from manual moiré and TMA measurements.

7.2 Computational Fringe Analysis

A detailed mathematical demonstration of the analysis of fringes using computational discrete Fourier transforms (DFT) is given in Chapter 2. This section will provide the practical details necessary to apply CAFRAN to real samples and packages. One of the obstacles limiting computational fringe analysis (CFA) in moiré has been the generally unreliable quality of the diffraction grating and resulting fringe pattern. The automated technique presently available are relatively primitive in their ability to distinguish grating discontinuities from actual intensity

variation. Missing or discontinuous grating on the sample surface results in a black region which might be interpreted as the imaginary or dark fringe regions. Thus, only recently have large area and high quality gratings allowed production of fringe patterns with virtually no discontinuities to disrupt the computational analysis. Many other factors with respect to image qualities must be considered as well to decrease the probability of interpretation error.

7.2.1 Image Quality Control

In the aluminum and PPGA packages analyzed, care was taken to adjust the contrast and brightness of the image so as to obtain the maximum amount of phase resolution. The intensity recorded at each cell on the Pulnix CCD camera was assigned to a number between 0 and 255 with 255 being pure white. The numbers in between 255 and 0 correspond to a gray scale which incrementally approaches pure black at 0. In order to maximize the amount of phase information it is desirable to adjust the gain and brightness of the camera output to center the distribution of pixels between 175 and 225. If the gain or brightness is too high much of the phase information within the bright part of the fringes will be lost since across the fringe in a perpendicular sense most of the pixels will be at one of the two values (255 or 0) and will not indicate if the intensity is increasing or decreasing. Image Pro Plus was used to monitor both the intensity profile and create histograms of pixel intensity distributions. In this manner the maximum information about the transition region (imaginary part) of the fringe pattern was obtained.

After digitizing an image with the proper contrast characteristics, the region which is to be mapped can be selected within Image Pro Plus and saved to disk. Two requirements must be met for this region of interest. Since CAFRAN uses a truncated Fourier transform technique with higher computational efficiency, it only allows the analysis of images from a table of pixel dimension acceptable to the algorithm. The author of the software supplied the compatible values upon request.

Another caveat in selecting the area of interest (AOI) is that the pixel/fringe (p/f) ratio distribution within the region should not be out of the range of 4-10 pixels/fringe for several reasons. First, if the p/f ratio is smaller than 4 there is very little phase information available to analyze and the resulting strain map will be highly sensitive to image noise. Second, at higher p/f ratios the scattered first and second harmonics of a pattern will begin to overlap causing the loss of

crucial phase information during filtering¹⁰. One additional limitation may apply depending on the complexity of the strain field. If a broad range of p/f ratios are present within a single AOI, the first and second harmonics for each specific ratio may overlap a first or higher harmonic belonging to another ratio resulting in a trade off between filtering and phase information loss. Poor filtering may cause subsequent interpretation error whereas the loss of phase information will certainly preclude its subsequent analysis. The challenge is made more interesting by the requirement that the fringe pattern representing the relative load condition follow these same guidelines in order to be compared by CAFRAN to the first image. Finally one should recall that eventually a precise actual linear dimension for the image will need to be known in order to compute strain, so a means of scaling an AOI must be maintained.

Bearing these limitations in mind the image can then be edited using a standard paintbrush program to correct any discontinuities which existed in the grating or other anomalies which are apparent. This edited image is then exported using the Silicon Video Image Processing (SVIP) software, in an X-Y string format with no headers. This allows the image to be read by CAFRAN and specifically by the fast Fourier transform (FFT) within CAFRAN.

7.2.2 CAFRAN Image Analysis

Once the image has been transported in XY string format to the IBM workstation on which CAFRAN runs, it is imported into the CAFRAN program. The same process of image capturing and quality control is carried out again for the sample in another thermal load state. The image representing the samples in relative load to the first is then imported in like manner. An FFT of the images (both loaded and unloaded) is then conducted and their 2-D FFT representations viewed in 2D phase space. The first harmonic of each fringe pattern is extracted using a filter function. An inverse fast Fourier transform (IFFT) is then executed on the phase information to recreate only the dominant periodic structure present in the original image, the fringes. This operation recreates the fringes with smoothed sinusoidally varying intensity profiles which are much more palatable for the phase unwrapping algorithm.

After filtering and smoothing both the original image and relative load image, the phase of the fringes are spatially determined using a the phase unwrapping algorithm described in more detail in Chapter 2. This assigns a cumulative 2D phase value to each pixel in the fringe patterns.

By selecting the direction (strain component) of interest, the phases representing analogous pixels in the original and relative load phase maps are subtracted. The cumulative phase value in the direction of interest is used in this process. This produces a phase map difference map (PDM) which depicts the pixel by pixel difference in phase between the two fringe patterns in the direction selected.

Juristically the phase is related to an incremental amount of displacement per unit (2π) of phase. This is derived from the concept that one light fringe represents 417 nm of displacement. The phase is simply a contiguous representation of the fringes allowing the consideration of fractional fringes more readily. Thus, the PDM represents the difference in displacement between the two fringe patterns or alternatively the accumulated displacement in going from one stress state to the other. Recalling from elementary mechanics that small strain is defined as change in length per unit length, if we calculate the length represented by each pixel and differentiate the PDM we obtain pixel by pixel strain information. Instead of only an average value for an entire element, we now are able to obtain up to 312,320 data points for the same region.

The actual data output from CAFRAN was represented in terms of radians/pixel and was translated into strain using an Excel spreadsheet conversion model. The primary equation is shown below

$$\varepsilon(x) = \left[\frac{\Delta\phi(x) \text{ radians}}{(\Delta x) \text{ pixels}} \right] \left[0.417 \frac{\mu\text{m}}{\text{fringe}} \right] \left[\frac{1 \text{ fringe}}{2\pi \text{ radians}} \right] \left[\frac{N \text{ pixels}}{X \mu\text{m}} \right] \quad (7-1)$$

where X is the actual distance covered by the image in the direction of interpretation, N is the number of pixels in the image in that direction and ϕ is the phase in radians. In the case of the aluminum bulk specimen the thermocouples measuring sample temperature were mounted directly to the sample and the CTE of aluminum had been measured by manual moiré and TMA. Thus, the temperature change between the original fringe pattern and the relative thermal load fringe pattern was known with 0.1 °C resolution. It was therefore more practical not to present the data in strain values but rather in extracted CTE using the equation below.

$$\varepsilon = \alpha_{Al} \Delta T \quad (7-2)$$

This extracted CTE value comparison approach was taken in the moiré strain calculations to allow the mutual comparability of the manual moiré, TMA and computational moiré data. This approach is only possible (if not practical) on the bulk aluminum since only normal

thermomechanical strains are present, whereas in the PPGA die attach the values would be meaningless given the elastic and plastic deformation occurring continuously within the package. The PPGA results are therefore the actual strain values obtained from CAFRAN using only equation 7-1.

7.3 CAFRAN Analysis of Aluminum

The thermomechanical strain induced in an the same aluminum sample tested using the moiré manual analysis and TMA in Chapter 4 was analyzed using computational fringe analysis. Two fringe patterns representing two different thermal loads, or temperatures were acquired using the guidelines cited *supra*. The figures below are the edited images before they were imported into CAFRAN for further processing.

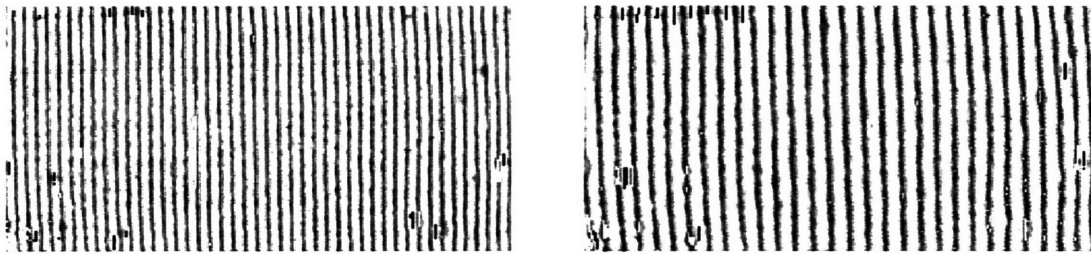


Figure 7.1-A (left) and B (right): Moiré fringe pattern of bulk aluminum on which the grating was replicated at 104 °C. The fringes represent displacement due to thermal strain accumulated in cooling to the sample temperature of A (23.9 °C) and B (52.8 °C). CAFRAN is used to compute the difference in strain (CTE) between the two fringe patterns.

After translating the image data represented in Figures 7.1-A and B into the proper X-Y string format it was imported into CAFRAN. An FFT of the images was then conducted to obtain a frequency domain representation of their structure. By eliminating all the periodic structures except the first harmonic, much of the high frequency intensity variation and low frequency background noise were eliminated. The frequency domain representation of Figures 7.1-A and B are shown below in Figures 7.2-A and B respectively.

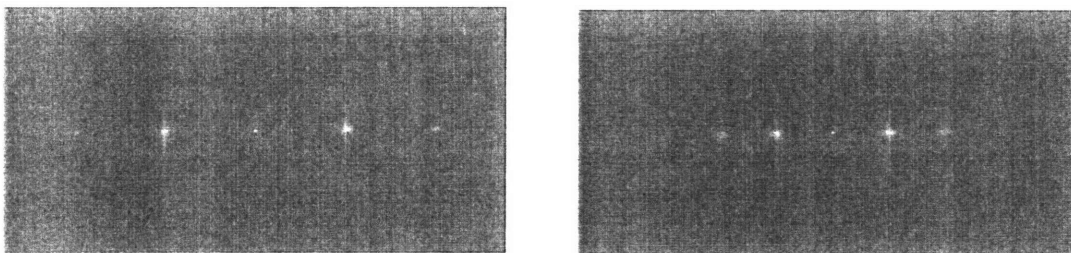


Figure 7.2-A and B-Two-dimensional frequency domain representation of Figures 7.1-A and B within CAFRAN.

The single bright dots in the center of the figures denote the origin of the phase map. The harmonic on the right side nearest the origin is isolated and the other phase information in the image is erased. This eliminates higher frequency intensity variations and lower frequency background noise as long as they are not within the frequency distribution associated with the first harmonic. The isolated first harmonics are shown below in Figures 7.3-A and B.

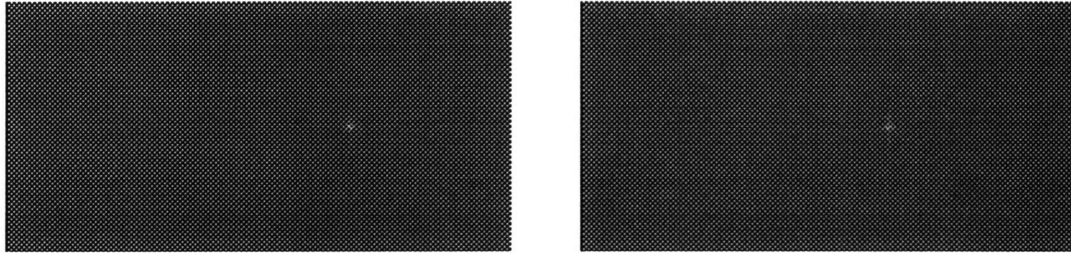
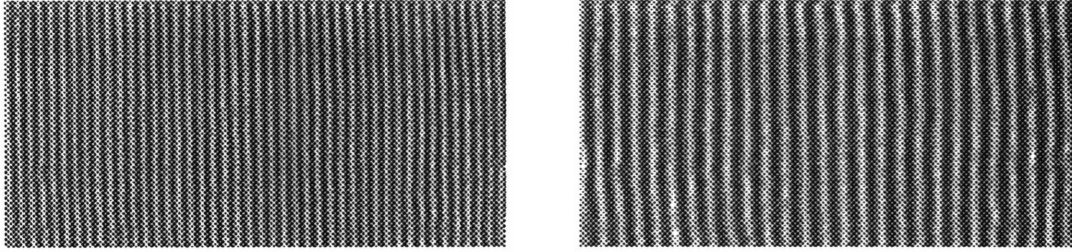


Figure 7.3-A and B-Isolated first harmonics for Figures 7.4-C and D respectively from left to right.

Something worth noting is that the distance of a harmonic from the origin is proportional to the frequency of the harmonic. The actual pixel/frequency proportionality factor was not known. The discretization or pixel/frequency proportionality appears to be identical although it isn't necessarily. The discretization need not be identical either since no interplay between the images will occur until after the fringes are recreated. In some techniques however, a reference grating (used to calibrate the PEMI) of lower frequency is used to increase the number of fringes in a pattern. If this had been applied here it would be necessary to shift the entire first harmonic toward the origin by the amount of the fringe frequency mismatch caused by the lower reference grating frequency. This is called the moiré mismatch method mentioned in Chapter 2 and though it was not implemented in this study, CAFRAN is capable of performing the Fourier space shifting functions required.

After isolating the first harmonics, the IFFT was invoked to yield Figures 7.4-A and B below. This IFFTd image is free of almost all of the high frequency and low frequency noise from the original image. The smoother intensity profile eliminated the higher frequency intensity variation not representative of the fringes and eliminates background intensity levels to maintain a more constant intensity amplitude across the sample.



Figures 7.4-A and B-Fourier transform filtered complex fringe pattern exhibiting smoothed intensity profiles.

By computing the arctangent of the ratio of the imaginary to real part of the smoothed complex fringe pattern the phase in the horizontal direction was determined. The phase map output given below from Chapter 2 (Equation 2-26)

$$\theta(x) = \tan^{-1} \left[\frac{\text{Im}\{h_1(x)\}}{\text{Re}\{h_1(x)\}} \right] \quad (7-3)$$

is discontinuous and must be connected by adding or subtracting 2π jumps to yield a continuously accumulating phase value from the starting pixel to the ending pixel. The phase maps for Figures 7.4-A and B are shown below in Figures 7.5-A and B respectively.

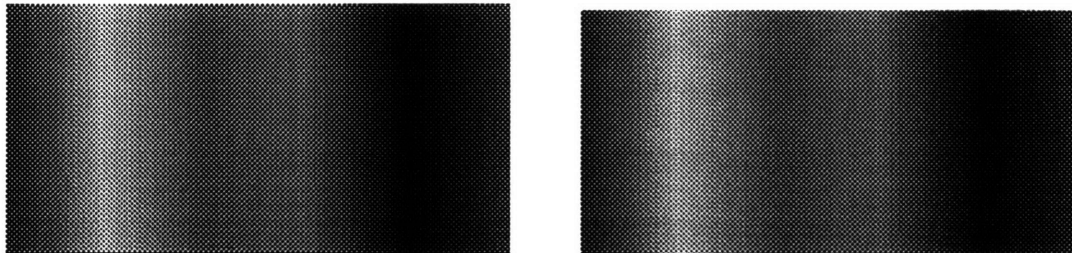


Figure 7.5-A and B-The cumulative phase maps representing the original fringe patterns. The phase accumulates from left to right.

Each color represents a normalized increment of phase within each map and should not be used as a basis to compare two different maps. CAFRAN stores the phase values underlying the phase map representation and uses those values for subsequent computations. By taking the pixel by pixel difference between the two phase maps shown above a phase difference map (PDM) is created. This represents the phase (or displacement) accumulated over the temperature range between the two fringe pattern temperatures represented. The PDM created by subtracting the phases of 7.5-A and B given below in Figure 7.6.

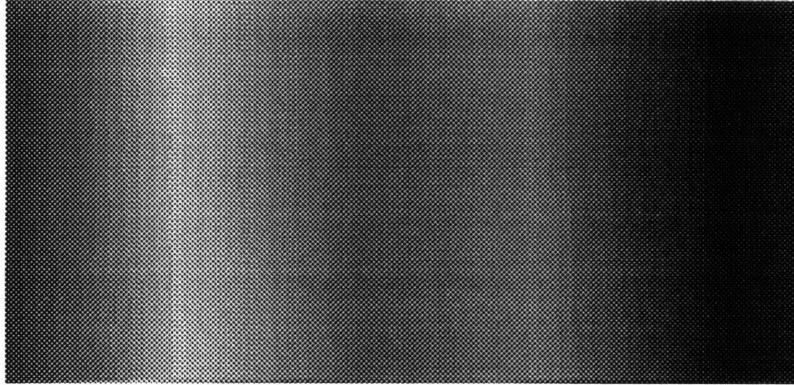


Figure 7.6-Phase difference map representing the pixel by pixel cumulative phase difference between the two aluminum fringe patterns.

By taking the derivative of the PDM and smoothing the data with a ten point moving average the change in phase per pixel is found. By applying equation (7-1) the differentiated PDM can be translated into a strain map. Although CAFRAN does not allow the introduction of dimensions or legends which assign the proper strain values to colors within the legend, the PDM derivative represented in the map is ascertainable and it is known that the 256 colors available are distributed equally within the range. Thus, the magnitude of strain represented by each color can be determined and a legend can be constructed using a simple paintbrush program. The strain map with color legend is shown below in Figure 7.7.

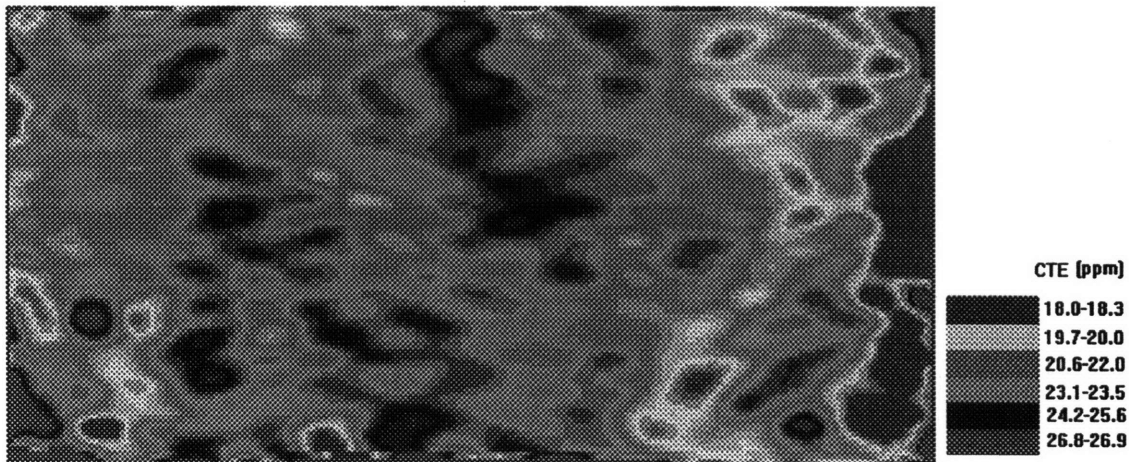


Figure 7.7-Color contour strain map for bulk aluminum specimen analyzed in Chapter 4. The legend denotes the CTE value based on the known ΔT and strain values by applying equation (7-2) to allow comparison with data in Chapter 4.

The median CTE value obtained from the map was directly in line with the previously measured results for the same sample in Chapter 4. The regions of high and low CTE values (or

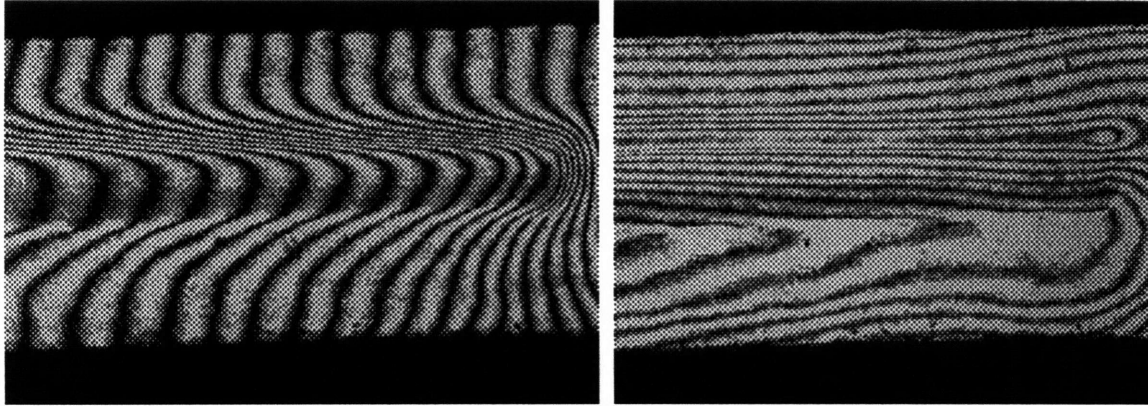
strain) are a result of fringe edge roughness, anomalous intensity variations and phase unwrapping misinterpretation. In regions near the edges of the image in the direction of interpretation (x direction in this case) the phase unwrapping algorithm has problems dealing with the discontinuities. This experiment was conducted a number of times to verify the reproducibility. The results established that CAFRAN was correctly analyzing the fringes computationally.

7.4 Computational Analysis of PPGA Fringe Patterns

After the CAFRAN fringe analysis algorithms had been validated numerous times on a control specimen, the software was used to analyze the shear strains in the die attach layer. Before starting the narration of the image processing protocol for the PPGA die attach region, several details must be discussed which distinguish shear strains. Recall from Equation (2-5) from Chapter 2 that the shear strain calculations require the consideration of both the U-field and V-field shear strain components. Within CAFRAN this was not possible without significant difficulty since there was no operation for strain map addition. Furthermore, the CCD camera pixel cells were rectangular rather than square causing one to need to dimensionalize the image in both the x and y directions to obtain strain. Remember that the V-Field strain is found by interpreting phase in the x direction and the U-Field by interpreting in the y direction.

Since the dimensionalization would have to have occurred within the Excel strain model since the CAFRAN data represents only in terms of change in phase per pixel. Thus the output of shear strain using CAFRAN in the present form would produce two partial strain maps representing the U and V-field shear strain components. The values for each would then need to translated separately into strain components using their own dimensionalization factor and finally combined on a pixel by pixel basis.

This cumbersome task was avoided by a simplification to the process made possible by a characteristic of the strain state in the die attach layer of the PPGA. The fringe patterns for the PPGA die attach region analyzed are shown below in Figure 7.8.



Figures 7.8 A and B-Room temperature (23 °C) U-Field (left) and V-Field (right) fringe patterns for encapsulated PPGA analyzed in Chapter 6.

The orientation of the PPGA is similar to that in Figure 6.1 with the copper substrate on the upper most portion of the pattern. Directly under the copper slug is the die attach layer followed by the die. The plastic encapsulant is the bottom region of the fringe pattern. Incidentally the corner of the die is seen in the middle of the fringe pattern (vertically) and on the far right. The region of interest is the die attach layer near this corner where manual shear strain calculations were made. Since the V-field has only a small fraction of a fringe in the x direction of the die attach region, it was assumed that its contribution to the shear strain was negligible. Thus it was possible to consider only the U-field to obtain the shear strain value. The AOI was first defined and edited in the previously described manner yielding Figures 7.9 A and B.

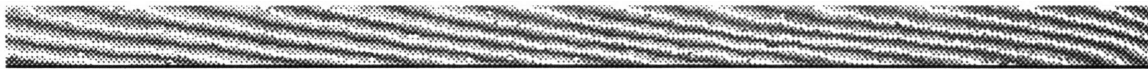


Figure 7.9A-U-field AOI in PPGA die attach region at 23.7 °C before importing into CAFRAN.

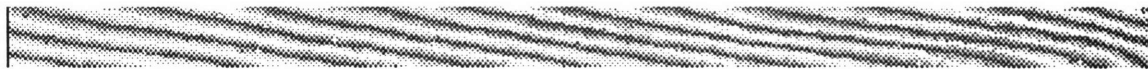


Figure 7.9B-U-field AOI in PPGA die attach region at 33.7 °C before importing into CAFRAN.

The images were then imported into CAFRAN as in section 7.4 where they were FFT'd for filtering and intensity profile smoothing. The phase domain representations of both fringe patterns are shown below in Figures 7.10A.



Figure 7.10A-Two dimensional frequency domain representation of Figure 7.9A.



Figure 7.10B-Two dimensional frequency domain representation of Figure 7.9B.

The harmonics exhibit frequency components in both the x and y directions as a result of the periodicity of the structure in both of these directions in the original images. The aluminum fringe pattern exhibited only normal thermomechanical strains and therefore was associated with a fringe pattern with only one component in frequency domain. The y directional frequency component was essentially zero denoting no periodic structure. In the die attach by contrast a row and column Fourier transform will detect periodicity in both directions. This gives rise to the harmonics being distributed up and to the right of the origin. They are at the (x,y) points representing the first harmonic in the x direction and the first harmonic in the y direction respectively. The isolated first harmonics for these fringe patterns are shown below in Figures 7.11 A and B.




Figure 7.11A-Isolated first harmonic from Figure 7.10A representing 7.9A.



Figure 7.11B-Isolated first harmonic from Figure 7.10B representing 7.9B.

After isolating the first harmonics and eliminating the higher frequency noise and lower frequency background noise, the fringe patterns were recreated again by IFFT. The IFFT'd fringe patterns are shown below in Figures 7.12 A and B.




Figure 7.12A-IFFT of Figure 7.11A to recreate the 23.7 °C fringe pattern.




Figure 7.12B-IFFT of Figure 7.11B to recreate the 33.7 °C fringe pattern.

The intensity profiles of the smoothed fringe patterns were then phase unwrapped shown below in Figures 7.13 A and B.



Figure 7.13A-Phase map of fringe pattern in Figure 7.12A.



Figure 7.13B-Phase map of fringe pattern in Figure 7.12B.

Then in an identical manner to the protocol in section 7.4, the difference between the pixel by pixel values represented by each phase map is then calculated to determine the PDM shown below in Figure 7.14.



Figure 7.14-Phase difference map depicting the pixel by pixel difference in the phase value in Figures 7.13 A and B.

By the same principles discussed previously the PDM was then differentiated and smoothed to yield a strain map shown below in Figure 7.15. The legend was then calculated and added later using an image editor.

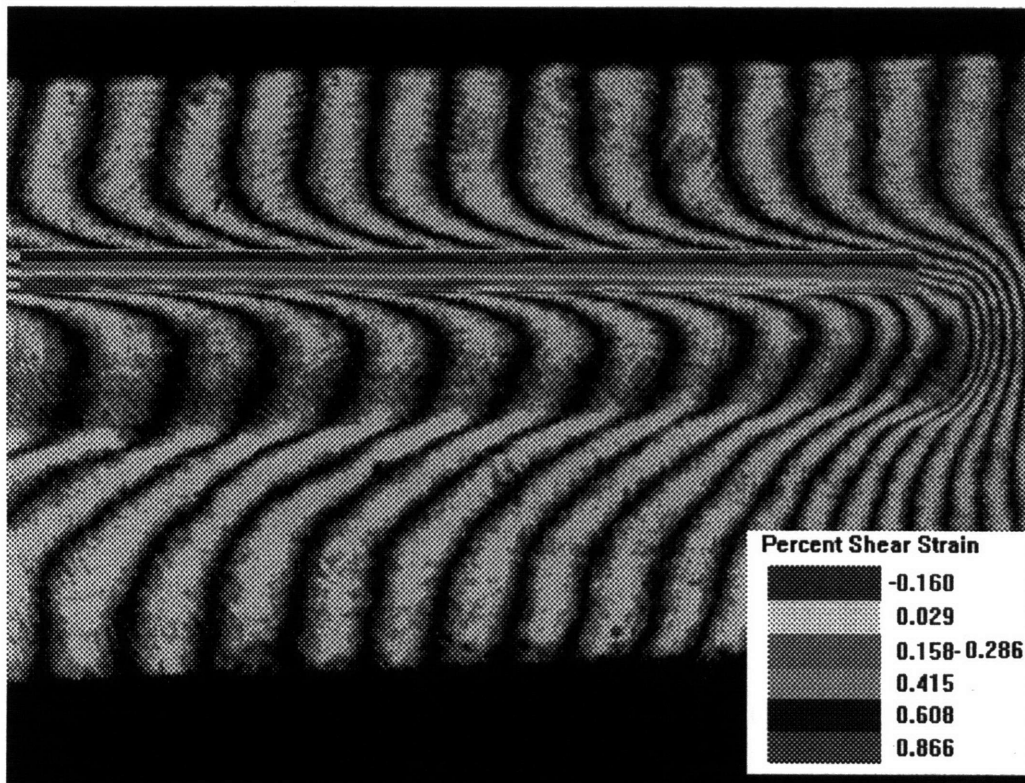


Figure 7.15-Strain map of encapsulated PPGA die attach region.

The values represented in the strain map are of the expected magnitude for accumulated strain in 10 °C change in sample temperature represented by the fringe pattern. The strain map for a 19.5 °C change in temperature was also produced using the same technique. The same original 23.7 °C fringe pattern was compared to one for the same sample at 43.2°C. Figure 7.16 A and B shows the die corner regions for both maps to illustrate the consistencies in their strain profiles and the front-like motion of strain contours as strain accumulates.

Strain Map of Encapsulated PPGA DA Layer (Map of Region 186 microns thick @ die corner)

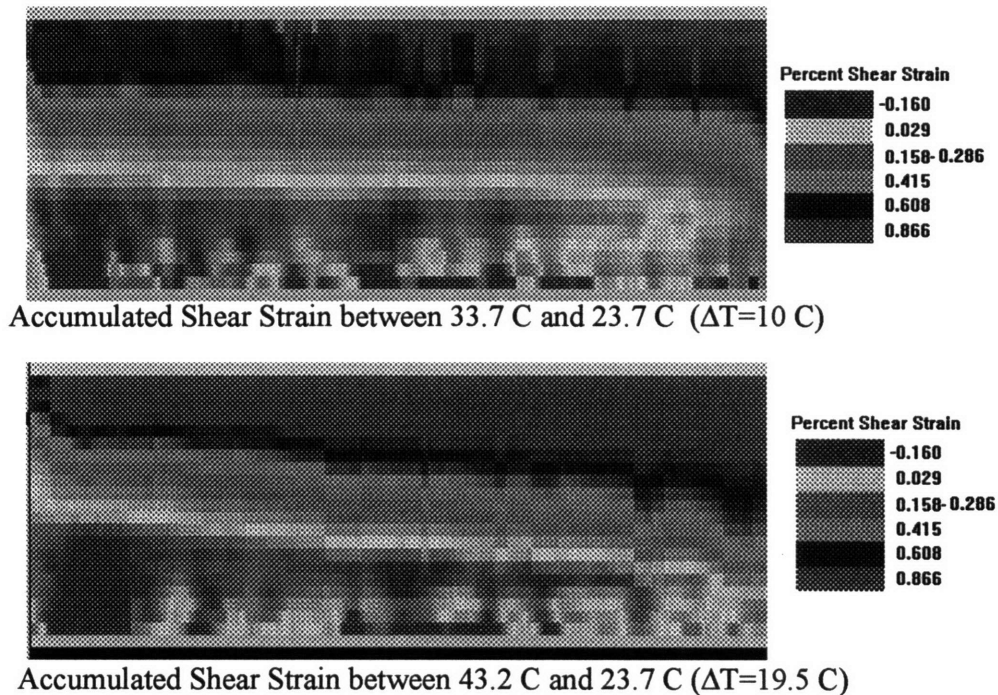


Figure 7.16 A and B-Comparison of strain maps for ΔT 's of 10°C and 19.5°C.

In summary, the strain values obtained using CAFRAN were on the right order of magnitude and the regions of the map which were sampled by the manual strain element perpendicular bisector yielded the same values of strain as the manual technique. The ability to resolve strains as precisely everywhere in the die attach region is not possessed by any other easily implementable technique of strain analysis. Thus, these results are presented as preliminary and unverified with some confidence being lent to their precision by the control specimen and the recurring strain pattern in both the 10 and 20 °C samples. Clearly improvements to the software would allow iterative changes in image processing and redefinition of AOIs that would lead to

better quality strain maps. The improvements to the system will be detailed in the future work section of the thesis, Section 8.2. A copy of 3D-CAFRAN may be obtained by sending email to: cafran@center.wakayama-u.ac.jp, Professor Yoshiharu Morimoto at morimoto@toro.me.es.osaka-u.ac.jp, or Professor Motoharu Fujigaki at fujigaki@center.wakayama-u.ac.jp.

Chapter 8

Conclusions and Future Work

8.1 Introduction

The assessment and proliferation of an experimental measurement tool involves a learning and validation stage, an implementation stage, and an automation or simplification stage. The initial stages of this research focused on establishing a fundamental protocol by which samples could be rendered, and the results obtained could be regarded as valid. The confidence for measurement validity must be provided by gauge studies against established alternative measurement tools and by religious adherence to the procedures developed for sample preparation. The final stage of the research focused on applying moiré interferometry strain analysis to actual packages or simulations of actual packages. In furtherance of the general motif of simplification, image processing was employed to automate the data reduction and improve the quality of the analysis. Validation of automated results was in turn provided again by measurements of bulk aluminum. In the process of improving and evolving the entire system a number of difficulties were encountered and on occasion potential solutions were envisioned. The following sections summarize the results of the validation, and automation phases of the research tool development and then propose further improvements and future applications for the system.

8.2 Summary of Results

The initial stage of tool validation was described in Chapters 3 and 4. A systematic method of applying diffraction gratings to samples and a method for reproducibly analyzing the samples was established. It was also determined that in electronic packages the cross-sectioning step was critical in obtaining accurate results. Cross-sectioning with a wire saw was determined to be the most reliable means of package separation. The glass transition temperature of the Tra-Con F-230 epoxy used in grating application was measured to be ~ 113 °C when cured at 104 °C. An assessment of the accuracy with which moiré can be used to measure mechanical strain was discussed in Chapter 4 where it was shown that moiré exhibited no bias and had comparable or better resolution than TMA is measuring normal thermal strains. Automated fringe reduction by CAFRAN was applied to the same samples and yielded continuous normal strain information which was centered on the values obtained by both the manual moiré and TMA methods. Thus, the manual and automated reduction methods are capable of providing valid strain information.

Moiré Interferometry was applied in two separate geometry/material comparison experiments. The first involving die bonded to organic and ceramic substrates demonstrated the capability of obtaining warpage-temperature profiles for the packages. The values of relative warpage measures were shown to have good correlation with results from laser profilometry (flexus). At room temperature the mean relative accumulated warpage for the die bonded packages was 3.4 and 49.9 μm for the ceramic and organic substrates respectively. The mean accumulated room temperature shear strain measured in the die bond layers was 0.25% and 1.54% for the ceramic and organic substrates respectively. Thus the organic sample, which contained a substrate that was 0.020" thinner than the ceramic sample, exhibited warpage ~15 times greater and shear strain ~6.14 times greater than the ceramic sample. The variance is attributed partially to the differences in CTE mismatches and partially to the differences in geometries (substrate thicknesses).

The second applications experiment involved assessment of the impact of plastic encapsulants on the monolithic warpage and die attach shear strain levels in PPGAs. It was found that the presence of the plastic encapsulant reduced the accumulated die attach shear from ~1.5% to ~0.45% in the PPGA at room temperature. Moreover the ending room temperature warpage magnitude was 2.5 μm for the die and 2.92 μm for the slug versus 10.85 μm for the die and 22.73 μm for the slug in the encapsulated and unencapsulated PPGAs respectively. Moiré was able to resolve a complex warpage accumulation reversal mechanism attributed to viscoelastic behavior in the plastic encapsulant and die attach materials between the temperatures of 100 °C and 25 °C. The encapsulant was shown to decrease the accumulated die attach shear by a factor of ~3.3 and decrease the room temperature relative warpings by factors of ~4.3 and ~7.8 for the die and slug respectively. All relative measures are given as the values relative to the absolute magnitudes of strain or warpage at the grating application temperature of 104 °C.

CAFRAN was used to computationally analyze the fringe patterns representing the die attach region of the encapsulated PPGA. The results showed that for a sample cooled from 43.2 °C to 23.7 °C ($\Delta T=19.5$ °C) that the accumulated strain in the die attach region was between ~0.16% and ~0.29% near the die interface and approached ~0.61% at the slug interface. Similarly as the sample was cooled from 33.7 °C to 23.7°C ($\Delta T=10$ °C) the relative accumulated die interface shear was less than ~0.16% and the slug interface shear was between 0.29% and 0.42%.

The reproducibility of these results must be verified by examination of a larger number of samples. The results may indicate that in some regions of the die attach layer that the accumulated relative shear strain on cooling to room temperature may reach ~2.47% rather than the 0.45% measured manually. The discrepancy between the manual results may be inherent to the process of manual differentiation which yields a single region average for shear strain. This value may or may not be the value present at the interfaces particularly if the perpendicular bisector lines do not sample the interface regions.

8.3 Future Work

The process of producing strain information for electronic packages can generally be broken into three steps: sample preparation, interrogation, and data reduction. Certainly each new study will require diligence to assess the damage sensitivity and specific sample preparation procedure, but there exist many overarching improvements which could be made to the physical moiré data acquisition system as well as sample preparation protocols which might increase the reproducibility and accuracy of the results.

The most pressing issue in samples preparation is the development of a cross-sectioning technique or set of techniques which introduces minimal damage and will allow larger numbers of packages to be analyzed. Second, an epoxy with a glass transition temperature at least above 150°C should be found to allow the study of the nonlinear behaviors in the range from 145°C to 100°C. The creep of polymers will occur most rapidly at high normalized homologous temperatures, thus the repeated cyclic analysis of a sample may have detrimental effects on the strain data accuracy. This effect should be characterized at least in a limited order of magnitude sense. Finally higher frequency diffraction gratings should be sought commercially if they become available. The yield on 1200 line/mm gratings is for all practical purposes 90-100% depending on the samples. A diminished yield would be a worthwhile trade-off if the resolution were increased. Finally, the feasibility of incorporating a shorter wavelength light source into the PEMI should be investigated although the physical construction of the apparatus may limit this.

Improvements to the data acquisition process include a need for a single high magnification zoom lens with a c-mount adapter for the CCD camera. With more advanced applications of CAFRAN the ability to control the fringe/pixel ratio for noise reduction purposes will rely almost

solely on the ability to continuously select magnification. The environment chamber described in Chapter 3 should be improved by adding direct sample thermocouple lines which could be used to measure and control the temperature gradient within the sample during testing. Finally, the samples should be analyzed using a mismatched grating method in which the null field is aligned with a master grating of different frequency than the samples' master grating. This will introduce constant carrier which can be calculated and subtracted from the final strain values.

The data reduction using CAFRAN would be expedited if a direct means of capturing images in Image Pro Plus and transporting them to CAFRAN existed. Furthermore, a large image with a large distribution of fringe densities could be importable and then individual regions of relatively constant fringe densities could be analyzed in a piecewise manner. Thus, a strain map for the entire package could be obtained by assembling all the maps. If moiré mismatch method is attempted by using a different frequency master grating, CAFRAN has the ability to shift Fourier spectra accurately provided the discretization is known and fringe/pixel ratio is great enough. Finally, CAFRAN should be altered to provide all the amenities of a standard windows image editing program, a continuous strain legend and the ability to separate and combine the different components of shear strain. These improvements would render CAFRAN a more powerful data reduction tool and would improve the ultimate accuracy of the maps by allowing the interactive optimization of data collection which is critical.

During the early stages of CAFRAN use the author attempted to obtain strain maps from individual fringe patterns using CAFRAN. This technique requires only one phase unwrap step as opposed to the phase map difference method presented in this study which uses two phase-unwrap steps. This preliminary experiment mistakenly found that CAFRAN was incapable of producing a single fringe pattern strain map representative of the accumulated strain in cooling from the grating application temperature. Subsequent follow-up efforts by George Raiser of Intel showed that CAFRAN did have this capability. Clearly the reduction of the number of phase-unwrapping steps from two to one will yield a dramatic decrease in phase-unwrap noise propagation. If a specific temperature range is to be focused on either method should provide comparable results. Any distinctions would be functions of differences in noise propagation through the processing sequences as the paths taken to arrive at the final strain map would be different.

References

1. Merriam-Webster, A. *Webster's Ninth New Collegiate Dictionary*, Merriam-Webster Inc., Springfield Massachusetts, 1991.
2. Walker, Colin A. "A Historical Review of Moiré Interferometry", *Experimental Mechanics*, December, 1994.
3. Guild, J., *The Interference Systems of Crossed Diffraction Gratings*, Oxford University Press, London, 1956.
4. Daniel Post, Bongtae Han, Peter Ifju. *High Sensitivity Moiré*, pp. 148-149, Springer-Verlag, 1994.
5. Takeda *et al.*, "Fourier-transform method of fringe-pattern computer-based topography and interferometry", *Journal of Optical Society*, Volume 72, No. 1, January 1982.
6. Takeda, Mitsuo, "Spatial-carrier fringe-pattern analysis and its applications to precision interferometry and profilometry: An overview", *Industrial Metrology*, vol. 1, 1990.
7. Takeda, M. and Mutoh, K., "Fourier Transform Profilometry for the Automatic Measurement of 3-D Object Shapes," *Appl. Opt.*, 22 (24), 3977-3982 (1983).
8. Morimoto, Y., Seguchi, Y. and Higashi, T., "Two-dimensional Moiré Method and Grid Method Using Fourier Transform", *SEM Conference Proceedings*, 1989.
9. Morimoto, Yoshiharu, Seguchi, Y., Higashi, Toshihiko, "Application of Moiré Analysis of Strain Using Fourier Transform", *Optical Eng.*, August 1988, Vol. 27 No. 8.
10. Morimoto, Y., Seguchi, Y. and Higashi, T., "Strain Analysis by Mismatch Moiré Method and Grid Method Using Fourier Transform", *Computational Mechanics*, 6, 1-10, 1990.
11. Morimoto, Y., Seguchi, Y. and Higashi, T., "Moiré Analysis of Strain by Fourier Transform", *JSME International Journal, Series I*, Vol. 32, No. 4, 1989.
12. Morimoto, Y., Seguchi, Y. and Sasahara, S., "Image Processing for Fourier Transform Moiré and Grid Method (FTMGM)", *SEM Conference Proceedings*, June 1990.
13. Morimoto, Y., Seguchi, Y. and Daifuku, K., "Fourier Transform Moiré Method In Consideration of Misalignment", *Proceedings 9th International Conference On Exp. Mech.*, Volume 4.
14. Morimoto, Yoshiharu, "Digital Image Processing", *Handbook of Experimental Mechanics*, Chapter 21, 1993.
15. Morimoto, Y., Gascoigne, Harold E. and Post, Daniel, "Carrier Pattern Analysis of Moiré Interferometry Using Fourier Transform Moiré Method", *Optical Engineering*, Vol. 33 No. 8, August, 1994.

16. Morimoto, Yoshiharu and Motofumi, Fujisawa, "Fringe Pattern Analysis of Phase-Shifting Method Using Fourier Transform", *Optical Engineering*, Vol. 33, No. 11, Nov 1994.
17. Guo, Y., Post, D., Czarnek, R., "The Magic of Carrier Fringes in Moiré Interferometry", *Experimental Mechanics*, June, 1989.
18. Morgan, C. J., "Least-squares estimation in phase-measurement interferometry", *Optics Letters*, Volume 7, Number 8, August 1982.
19. Mertz, L., "Real-time fringe-pattern analysis," *Applied Optics*, Volume 22, Number 10, 1983.
20. Bastawros, A. F., Voloshin, A. S., "Thermal Strain Measurements in Electronic Packages Through Fractional Fringe Moiré Interferometry", *Journal of Electronic Packaging*, Volume 112, December 1990.
21. Voloshin *et al.*, "Fractional Moiré Strain Analysis Using Digital Imaging Techniques", *Experimental Mechanics*, September 1986.
22. Creath, K., "Phase-Measurement Interferometry Techniques," *Progress in Optics*, Volume 26, 1988.
23. Cavaco, Marco A. M., Voloshin, Arkady, "Automated Moiré Interferometry for Strain Analysis of Electronic Packages", Lehigh University.
24. Shield, T. W., Kim, K.S., "Diffraction Theory of Optical Interference Moiré and a Device for Production of Variable Virtual Reference Gratings: A Moiré Microscope", *Experimental Mechanics*, June, 1991.
25. Shield, T. W., Kim, K., S., "Experimental Measurement of the Near Tip Strain Field in an Iron-Silicon Single Crystal", *Journal of Mech. Phys. Solids*, Volume 42, Number 5, 1994.
26. Macy, William W., "Two-dimensional fringe-pattern analysis", *Applied Optics*, Volume 22, No. 23, December 1983.
27. Kowalski, V. T., Voloshin, A. S., "Moiré interferometry Analysis of Laser Weld Induced Thermal Strain", *Journal of Electronic Packaging*, Volume 116, September 1994.
28. Choi, H. C. *et al.*, "Solder Ball Connect (SBC) assemblies under thermal loading: II. Strain Analysis via image processing and reliability considerations", *IBM Research and Development*, Volume 37, Number 5, September 1993.
29. Han, Bongtae, "Interferometric methods with enhanced sensitivity by optical/digital fringe multiplication", *Applied Optics*, Volume 32, Number 25, September 1993.
30. Poon *et al.*, "Spatial-Carrier Phase Shifting Method of Fringe Analysis for Moiré Interferometry", *Journal of Strain Analysis*, Volume 28, Number 2, 1993.
31. Poon *et al.*, "Automated Fringe Pattern Analysis for Moiré Interferometry", *Experimental Mechanics*, September 1993.

32. Huntley, J. M., Saldner, H., "Temporal phase-unwrapping algorithm for automated interferogram analysis", *Applied Optics*, Volume 32, Number 17, June 1993.
33. Roddier, Claude, Roddier, Francois, "Interferogram analysis using Fourier transform techniques", *Applied Optics*, Volume 26, Number 9, May 1987.
34. Creath, Katherine, "Phase-measurement Interferometry Techniques", *Progress In Optics*, Volume 26, 1988.
35. Hariharan, B.F. Oreb, Brown, N., "A Digital Phase-Measurement System for Real-Time Holographic Interferometry", *Optics Communications*, Volume 41, Number 6, May 1982.
36. Bone, Donald J. *et al.*, "Fringe-pattern analysis using a 2-D Fourier Transform", *Applied Optics*, Volume 25, Number 10, May 1986.
37. Kujawinshka, Malgorzata, "Use of phase-stepping automatic fringe analysis in moiré interferometry", *Applied Optics*, Volume 26, Number 22, November 1987.
38. Singh, Harmeet, Sirkis, James S., "Direct extraction of phase gradients from Fourier-transform and phase-step fringe patterns", *Applied Optics*, Volume 33, Number 22, August 1994.
39. Gierloff, Jeffrey J., "Phase Unwrapping by Regions", *Current Developments in Optical Engineering II*, Volume 818, 1987.
40. Huntley, J. M., "Noise-immune phase unwrapping algorithm", *Applied Optics*, Volume 28, Number 15, August 1989.
41. Tomlimieri, Richard, An, Myoung and Lu, Chao, *Algorithms for Discrete Fourier Transform and Convolution*, Springer-Verlag, 1989.
42. Savitzky, Abraham and Golay, Marcel J. E., "Smoothing and Differentiation of Data by Simplified Least Squares Procedures", *Analytical Chemistry*, Vol. 36, No. 8, July 1964.
43. Franklin, Philip. *Fourier Methods*, McGraw-Hill, 1949.
44. Seeley, Robert T., *An Introduction to Fourier Series and Integrals*, W.A.Benjamin, 1966.
45. Lau, John H., *Thermal Stress and Strain in Microelectronics*, Van Nostrand Reinhold, New York, 1993.
46. Reed, Robert E., Abbaschian, Reza. *Physical Metallurgy Principles*, PWS-Kent Publishing, Boston, 1991.